

PROBING THERMONUCLEAR BURNING ON ACCRETING NEUTRON STARS

Cover: 25 hour long X-ray light curve of LMXB EXO 0748-676, which exhibits single, double and triple bursts (see Chapter 4), combined with the light curve of 4U 1608-522 at the time of its superburst (see Chapter 3). The background is a wide star field image of the region around HD 189733b (credit: NASA, ESA, and the Digitized Sky Survey 2; acknowledgment: Davide De Martin, ESA/Hubble).

© 2008 Laurens Keek. Copyright of Chapter 2, 3 and 4 is owned by Astronomy and Astrophysics. These chapters are reproduced with permission.

This book is typeset in L^AT_EX using the CLASSISTHESIS package. Printed by Gildeprint Drukkerijen BV.

ISBN 978-90-393-4946-5

PROBING THERMONUCLEAR BURNING ON ACCRETING NEUTRON STARS

THERMONUCLEAIRE VERBRANDING OP
ACCRETERENDE NEUTRONENSTERREN

(met een samenvatting in het Nederlands)

PROEFSCHRIFT

ter verkrijging van de graad van doctor aan de Universiteit Utrecht op gezag van de rector magnificus, prof. dr. J. C. Stoof, ingevolge het besluit van het college voor promoties in het openbaar te verdedigen op maandag 1 december 2008 des middags te 2.30 uur

door

LAURENS KEEK

geboren op 11 april 1980 te Winterswijk

Promotor: Prof. dr. N. Langer
Co-promotoren: Dr. J.J.M. in 't Zand
Prof dr. M. Méndez

CONTENTS

1	Introduction	9
1.1	Neutron star formation	9
1.2	Structure	10
1.3	Manifestations	11
1.4	Thermonuclear burning	14
1.5	Thermonuclear X-ray bursts	17
1.6	In this thesis	18
1.7	Outlook	20
2	The superburst recurrence time in luminous persistent LMXBs	21
2.1	Introduction	21
2.2	Observations	24
2.3	Search for superbursts	24
2.4	Recurrence time	26
2.5	Mass accretion rate	29
2.6	Discussion	32
2.7	Conclusion	35
3	First superburst from a classical low-mass X-ray binary transient	37
3.1	Introduction	37
3.2	Observations and spectral calibration	39
3.2.1	Observations	39
3.2.2	Spectral calibration of the ASM	41
3.3	History of accretion and X-ray burst activity	42
3.3.1	Long-term light curve	42
3.3.2	Accretion rate	43
3.3.3	Long-term bursting behavior	49
3.4	Superburst analysis	51
3.4.1	Light curve	51
3.4.2	Spectral analysis, energetics and layer thickness	55
3.5	Discussion	59
3.5.1	Recurrence time	60
3.5.2	Producing and preserving carbon	62
3.5.3	The crust temperature and carbon ignition	63
3.5.4	Bursting behavior and mHz QPOs	66
3.6	Summary and conclusions	66

4	Discovery of X-ray burst triplets in EXO 0748-676	69
4.1	Introduction	70
4.2	Observations and data reduction	72
4.3	Non-bursting emission	74
4.4	Bursts	76
4.4.1	Parameters definition	78
4.4.2	Parameters distributions	81
4.4.3	Relation between burst fluence and accumulated mass	86
4.4.4	Relation between fluence and flux	89
4.4.5	Profiles	89
4.4.6	Spectral properties	92
4.5	Comparison with the EXOSAT observations	97
4.6	Discussion	100
4.6.1	Comparison with theory: LWT bursts	102
4.6.2	Comparison with theory: SWT bursts	106
4.A	Light curves & bursts list	109
5	The effect of rotation on the stability of nuclear burning in accreting neutron stars	115
5.1	Introduction	115
5.2	Method	117
5.2.1	Grid	118
5.2.2	Accretion	118
5.2.3	Diffusivity and viscosity	119
5.2.4	Initial model	120
5.2.5	Flux from the crust	121
5.3	Results	121
5.3.1	Turbulent mixing	121
5.3.2	Effect of mixing on stability	127
5.3.3	Mass accretion rate dependence	133
5.4	Discussion	134
5.4.1	Non-magnetic mixing	135
5.4.2	Centrifugal force	136
5.4.3	Marginally stable burning	136
5.4.4	Further consequences of mixing	138
5.5	Conclusion	138
6	Thermonucleaire verbranding op accreterende neutronensterren	141
6.1	Van zeer groot tot uiterst klein	141
6.2	Neutronensterren	142
6.3	Röntgenflitsen	143

6.4	Te snel	143
6.5	Superflitsen	145
6.6	Een gewone superflits?	145
6.7	Explosief of stabiel?	147
6.8	Conclusie	148
Curriculum Vitae		149
Publications		151
Acknowledgments		153
Bibliography		155

CONTENTS

INTRODUCTION

Neutron stars are the most compact objects that can be directly observed. They have a mass of the order of $1 - 2 M_{\odot}$ and a $10 - 20$ km radius, such that the average density equals or exceeds the nuclear matter density of $2 \cdot 10^{14} \text{ g cm}^{-3}$. In fact, if neutron stars were compressed to just a third of their size, they would be black holes, which can only be detected indirectly. Due to their extreme densities, neutron stars are unique laboratories for particle physics. The equation of state of matter at supranuclear densities and low temperatures, like in the neutron star core, is currently poorly constrained and a much studied topic. However, the neutron star itself and its diverse phenomena are interesting in their own right. In this thesis we focus on the nuclear burning in the envelopes of neutron stars that accrete matter from a binary companion star.

In this chapter we introduce neutron stars and their different observed manifestations. In particular we present a brief overview of observations and models concerning thermonuclear burning in the envelopes of accreting neutron stars.

1.1 NEUTRON STAR FORMATION

A neutron star (first suggested by Landau in 1932, see Rosenfeld 1974; Baade & Zwicky 1934) is formed in the center of an aging massive star when its core collapses. The collapse itself is a spectacular and violent event. Following the core collapse, the outer layers of the star explode as a supernova. During the collapse, the degenerate neutrons formed by electron capture on protons provide a pressure. As long as gravity exceeds this pressure, the core continues its collapse and the radius becomes smaller than the Schwarzschild radius, resulting in a black hole. However, for stars with an initial mass of less than approximately $25 M_{\odot}$, gravity is balanced by the degeneracy pressure. In this case the core is stable and forms a neutron star (e.g., Heger et al. 2003).

Alternatively, a neutron star can be formed through the accretion-induced collapse of a white dwarf in a binary system. Also in this case the collapse gives rise to a supernova. Depending on the amount of

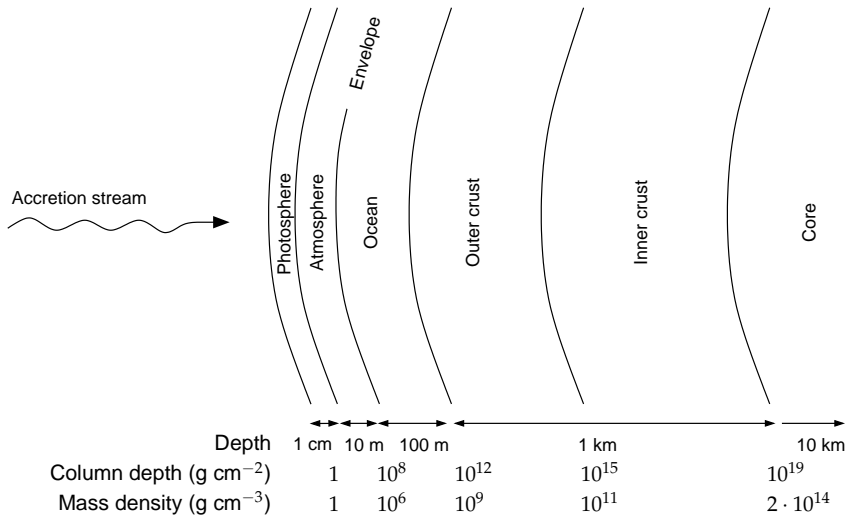


Figure 1.1: Schematic structure of a neutron star. Indicated are the thickness of the different layers as well as the column depth and density at their boundaries, for a $1.4 M_{\odot}$ neutron star with a 10 km radius.

energy released, the white dwarf either completely disrupts or transforms into a neutron star (Nomoto & Kondo 1991).

1.2 STRUCTURE

A neutron star consists of several parts with different constituent particles and phases: a core, a crust and an envelope (Fig. 1.1; e.g., Page & Reddy 2006). If the neutron star accretes from a binary companion star, the atmosphere consists typically of hydrogen and helium. Below the atmosphere is an ocean of ashes of nuclear burning in the atmosphere. Atmosphere and ocean constitute the envelope.

In the outer crust, pycnonuclear fusion and electron capture reactions take place (Sato 1979; Haensel & Zdunik 1990). The latter produce neutron-rich isotopes. At the bottom of this layer the “neutron drip point” is reached, where it becomes energetically favorable for some neutrons to be outside nuclei. Further down, the inner crust consists of a mixture of neutron-rich isotopes and an increasing number of “free” neutrons.

The innermost part is the core, where the density exceeds the nuclear density. The equation of state, which relates the density and the

pressure, for the core and the type of constituent particles are poorly understood. Depending on how high the density at the center is, matter may be in the form of neutrons or more exotic particles such as pions, hyperons, deconfined quarks or even strange quarks (see, e.g., the review by Lattimer & Prakash 2007). Matter cannot be probed under these conditions in particle accelerators on Earth, making neutron stars the only laboratories available to study physics under these extreme conditions. Potentially, observations of neutron stars can pose constraints on the quantum chromodynamics (QCD) theory at high densities and low temperatures.

An important step in discriminating between the different possible equations of state is accurately measuring both the mass and radius of a neutron star. This has proven to be quite a challenge. The most constraining measurement thus far is obtained by Özel (2006) and Cottam et al. (2002), which favors hadronic equations of state.

1.3 MANIFESTATIONS

After its birth in a supernova, the neutron star presumably cools down from surface temperatures of around 10^6 K, emitting radiation with a thermal spectrum that peaks in the soft X-ray band. Due to the small surface area, the luminosity is relatively low. After several tens of thousands of years, the flux is expected to decline below the detection threshold of current X-ray telescopes. This would explain why, out of the $10^8 - 10^9$ neutron stars expected to exist in our Galaxy (e.g., Faucher-Giguère & Kaspi 2006), the ROSAT all-sky survey detected only 7 so-called dim isolated neutron stars for which the flux is likely due to cooling (Treves et al. 2000). As dim stellar remnants, neutrons stars may seem uneventful. However, it is their compact nature which gives rise to diverse and spectacular manifestations that enhance their detectability. Currently $\sim 10^3$ neutron stars have been detected.

During the collapse which forms the neutron star, conservation of angular momentum causes the core to spin up as its radius shrinks. Neutron stars have been observed with spin frequencies of up to 716 Hz (Hessels et al. 2006). Also, a magnetic field is present with a typical field strength of 10^{12} G. The magnetic dipole field causes charged particles to be accelerated at the magnetic poles and emitted in a beam, carrying away energy and angular momentum. This causes the neutron star to spin down. The charged particles emit beamed synchrotron radiation. As the neutron star rotates, such a beam can periodically cross our line of sight, resulting in pulses (Gold 1968; Pacini 1967). These so-called rotation-powered pulsars have been observed mostly at ra-

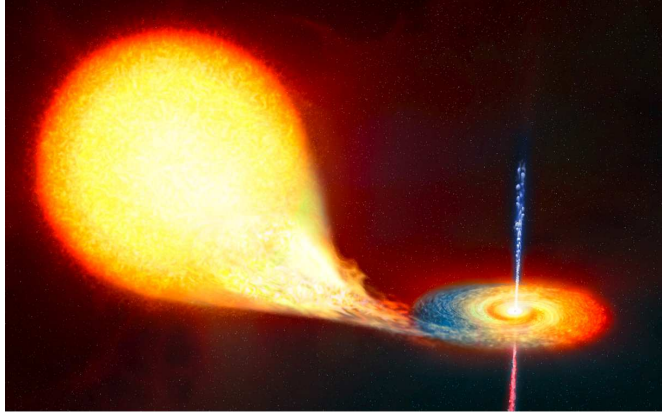


Figure 1.2: Artist's impression of a low-mass X-ray binary. The companion star (left) fills its Roche lobe and donates matter to the compact object (right) through an accretion disk. *Credit: ESA.*

dio wavelengths (Bell & Hewish 1967; Hewish et al. 1968). Another class of pulsars are the magnetars, which are thought to have very high magnetic fields of $10^{14} - 10^{15}$ G. Since the luminosities of magnetars are larger than can be explained from the loss of rotational energy, it is thought that the decay of the strong magnetic field powers their emission (Kouveliotou et al. 1998; Thompson & Duncan 1995, 1996).

The above mentioned manifestations are mostly observed in isolated neutron stars. However, approximately 10% of the known neutron stars in our Galaxy are found in X-ray binaries (Liu et al. 2007). No radio pulses are observed from these sources, possibly due to burial of the magnetic field by matter accreted from the companion (e.g., Cumming et al. 2001) or due to the accretion stream blocking the acceleration of charged particles. Depending on the mass of the companion star one speaks of a high- or low-mass X-ray binary. For low-mass X-ray binaries (LMXBs) the companion star has a mass of less than approximately $1 M_{\odot}$. Matter can be accreted from the companion star through Roche-lobe overflow, forming an accretion disk around the neutron star (Fig. 1.2). Because of the high surface gravity of the neutron star of $g_{\text{surface}} \simeq 2 \cdot 10^{14} \text{ cm s}^{-2}$, the infall of matter liberates a large amount of potential energy which heats the accretion disk. The bulk of this heat is radiated away in X-rays.

While the accreted matter is often of solar composition (i.e., approximately 73% hydrogen and 25% helium), the precise mass fractions of

the different elements can vary from star to star. A subset of LMXBs are known to have binary periods of one hour or less. In the small orbit of such so-called ultra-compact systems, only an evolved star stripped of its hydrogen-rich envelope fits. The matter accreted in ultra-compact systems is therefore hydrogen-deficient (see, e.g., in 't Zand et al. 2005).

Matter is typically transferred from the companion star to the disk at a more or less constant rate, which varies from source to source. However, the rate at which matter is accreted from the disk onto the neutron star can change in time. While some sources have displayed a fairly constant accretion rate over the past decades, so-called transient sources accrete only significantly during outbursts which last on average a few months. When the outburst has ceased, the source is said to be quiescent. The maximum accretion rate is set by the Eddington limit. For a $1.4 M_{\odot}$ neutron star, the Eddington-limited accretion rate is $\dot{M}_{\text{Edd}} \simeq 2 \cdot 10^{-8} M_{\odot} \text{yr}^{-1}$ for hydrogen-rich accretion and $\dot{M}_{\text{Edd}} \simeq 3 \cdot 10^{-8} M_{\odot} \text{yr}^{-1}$ otherwise.

Different phenomena from LMXBs are observed in X-rays as a result of the accretion process, for instance:

- ★ For sources observed at high orbital inclinations, variations in the flux are detected at regular intervals (Fig. 1.3). When the binary companion obscures the accretion disk, an eclipse takes place. Sometimes “dips” are observed: (partial) obscurations due to filaments on the disk (Frank et al. 1987).
- ★ Kilohertz quasi periodic oscillations (kHz QPOs) are variabilities on timescales similar to the dynamical timescale at the inner edge of the accretion disk (e.g., van der Klis 2006). Two peaks are observed in the power spectrum with frequencies in the range of 200 to 1200 kHz. When the spin of the source is detected, the peaks are found to be separated in frequency by approximately the spin frequency or half this value (although the situation may be more complicated, see Méndez & Belloni 2007).
- ★ A broad iron emission line is observed from a number of LMXBs. Similar to kHz QPOs, the origin is likely the inner edge of the accretion disk, where the rotational velocity is a substantial fraction of the speed of light. The line has a broadened and skewed profile due to Doppler and relativistic effects (Fabian et al. 1989; see the review by Miller 2007).
- ★ X-ray bursts with a typical duration of 10 – 100s, a recurrence time as short as a few minutes and a spectrum identical to that

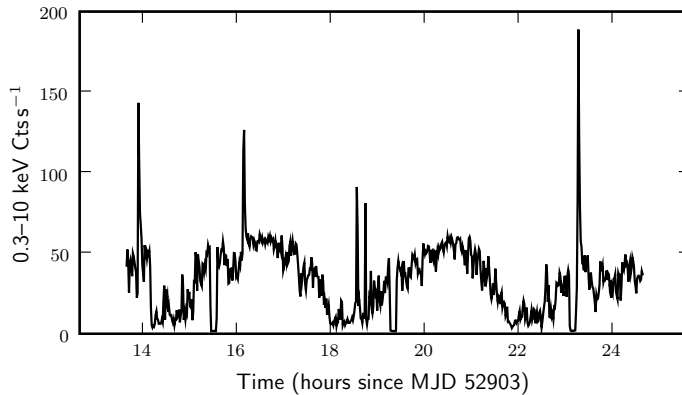


Figure 1.3: Light curve at 60 s time resolution with dips, eclipses and bursts. XMM-Newton observation of EXO 0748-676. The persistent flux is modulated by dips, while it almost completely vanishes during three eclipses. The five bright peaks are type I X-ray bursts. The recurrence time between the third and the fourth is remarkably short: ten minutes. See also Chapter 4.

of the non-burst emission. These so-called type II X-ray bursts are thought to originate in the disk (Lewin et al. 1993). Only two neutron star LMXBs exhibit this phenomenon: the Rapid Burster and the Bursting Pulsar.

- ★ X-ray pulsations, which are probably related to the existence of a hot spot where the accretion stream hits the neutron star surface (Wijnands & van der Klis 1998). Ten so-called accretion-powered millisecond pulsars have been identified. Three of these sources are intermittent pulsars of which pulsations are detected only during part of the time.

Once the accreted material has reached the surface it can undergo thermonuclear burning. Unstable burning is observed as thermonuclear bursts, while stable burning produces a luminosity which is only of the order of one percent of the luminosity from the accretion process.

1.4 THERMONUCLEAR BURNING

As matter is accreted, it accumulates in a layer on the neutron star surface. When this shell is just a few meters thick, the density and

temperature at the bottom are such that nuclear fusion starts. The temperature in this shell is determined by the balance between burning and cooling processes. Thermonuclear burning releases energy, which is transported out of the shell by radiative cooling. Note that in the steady state neutrino-cooling does not play an important role in the envelope. If the temperature rises, the energy generation rate due to the burning increases as well as the cooling rate. If the energy generation rate increases faster than the cooling rate, a thermonuclear runaway occurs. The thermonuclear burning proceeds in an unstable manner, causing the entire layer to burn on a timescale of 1 s. The energy of the flash is released as a burst of X-rays which briefly outshines the accretion radiation from the disk (Woosley & Taam 1976; Maraschi & Cavaliere 1977; Lamb & Lamb 1978).

Whether burning is stable or unstable thus depends on the temperature dependence of the energy generation rate and the cooling rate. The radiative cooling rate is proportional to T^4 . The energy generation rate depends on the type of the reaction, the temperature and the timescales of spontaneous decay of the various isotopes. Since the accreted material consists mostly of hydrogen and/or helium, the relevant reaction chains are primarily those involving hydrogen and helium burning.

When the temperature in the accreted layer is $T \gtrsim 10^7$ K, hydrogen burns via the hot CNO cycle, producing helium. For temperatures in excess of $8 \cdot 10^7$ K, β -decay gives the longest timescale in this reaction chain. This timescale is independent of temperature, implying that the energy generation rate depends solely on the amount of available CNO nuclei. Under these conditions hydrogen burning proceeds in a stable manner.

Helium burns via the triple-alpha process which has a strong temperature dependence: $\epsilon_{3\alpha} \propto T^{41}$ at $T = 10^8$ K. Therefore, a small temperature increase leads to a large increase in the amount of generated energy, causing a thermonuclear runaway. However, the dependence decreases towards higher temperatures, such that above a certain temperature it is smaller than the temperature dependence of the cooling rate and helium burning is stable. At a typical column depth of $y \simeq 10^8$ g cm $^{-2}$, the transition lies at $T \simeq 3.5 \cdot 10^8$ K (Bildsten 1998).

In case a mixed hydrogen/helium flash occurs, the rapid proton capture process (rp-process) produces heavy isotopes up to a mass number of about 100 (Schatz et al. 2001). When hydrogen and helium burn stably or when helium burns unstably in a hydrogen-deficient environment, a carbon-rich layer is produced. At a column depth of $y \simeq 10^{12}$ g cm $^{-2}$ and a temperature of $T \simeq 5 \cdot 10^8$ K carbon can ignite and burn unstably.

With these conditions for the stability of the nuclear burning of hydrogen and helium, the theoretical models find different scenarios as a function of the mass accretion rate (Fujimoto et al. 1981; see also Bildsten 1998). For $\dot{M} \lesssim 0.5 \cdot 10^{-2} \dot{M}_{\text{Edd}}$ hydrogen ignites unstably, resulting in a combined hydrogen/helium flash (assuming a neutron star mass of $1.4 M_{\odot}$ with a 10 km radius, a hydrogen mass fraction $X = 0.7$ and a CNO mass fraction $Z_{\text{CNO}} = 0.01$). If accretion is faster, hydrogen burning proceeds in a stable manner. For $0.5 \cdot 10^{-2} \dot{M}_{\text{Edd}} \lesssim \dot{M} \lesssim 3 \cdot 10^{-2} \dot{M}_{\text{Edd}}$, helium ignites unstably when hydrogen is burned completely, while for $3 \cdot 10^{-2} \dot{M}_{\text{Edd}} \lesssim \dot{M} \lesssim \dot{M}_{\text{Edd}}$ the helium flash ignites while some hydrogen is still unburnt. At accretion rates in excess of \dot{M}_{Edd} the models predict helium burning to be stable. For sources that accrete hydrogen-deficient material, the lack of heating due to stable hydrogen burning shifts this transition even higher accretion rates (Bildsten 1995, 1998). Note that if accretion is not spherically symmetric and the spreading of material over the neutron star surface is less efficient than expected, for instance due to channeling by the magnetic field, the accretion rate may locally be different from the global accretion rate \dot{M} .

The temperature in the accreted layer is an important factor in whether nuclear burning proceeds in a stable or unstable manner. Apart from the heat generated by stable hydrogen/helium burning, it is determined by the heat flux from the neutron star crust. During accretion the crust is compressed, inducing pycnonuclear reactions and electron captures. About 10% of the thus generated energy heats up the accreted layer, the rest goes to the inner crust and core and is subsequently emitted as neutrinos. Since the heat generation is the result of compression due to the accreted column of matter, the heat flux into the accreted layer is proportional to the mass accretion rate and typically generates $0.1 \text{ MeV nucleon}^{-1}$ (Haensel & Zdunik 2003), although it may be up to ten times more (Gupta et al. 2007).

The picture sketched above explains that for nuclear burning to occur, a fuel column has to be accreted up to a thickness such that at the bottom the ignition conditions are reached. However, if the accreted matter is efficiently mixed down to larger depths, these conditions can be reached sooner. A possible source for chemical mixing are (magneto)hydrodynamical instabilities. Since the accreted matter has a larger rotational velocity than the neutron star itself, the angular momentum is transported throughout the star, creating differential rotation. The latter can give rise to hydrodynamical instabilities driving the angular momentum transport and generating turbulence (Fujimoto 1993). The turbulent motions mix the chemical composition of neighboring mass elements. Studies of these processes in accreting white

dwarfs show that mixing allows for more stable shell burning (Yoon et al. 2004a). Recent analytical and numerical studies that also include magnetic fields find that mixing can have a similar effect in accreting neutron stars (Piro & Bildsten 2007).

1.5 THERMONUCLEAR X-RAY BURSTS

The picture presented in the previous section of thermonuclear shell flashes explains the type I X-ray bursts observed in LMXBs since 1975 (Grindlay et al. 1976; see reviews by Lewin et al. 1993, Strohmayer & Bildsten 2006). At present several thousands of these bursts have been observed from approximately 90 sources in our galaxy (see e.g., Galloway et al. 2006). They have in common a peak effective temperature of 10^7 K and a light curve consisting of a fast rise followed by a slower, exponential-like decay. The differences in rise and decay timescales, recurrence times and energy output can generally be well explained by differences in mass accretion rate and composition of the accreted matter.

A flash of hydrogen and/or helium typically takes less than 1 s. Afterwards one observes the cooling of the burnt layer. In the presence of hydrogen, the rp-process may take place, which has a timescale of 10 to 100 seconds. Therefore, bursts with longer tails are often thought to result from burning in a hydrogen-rich layer.

For sources that accrete mostly helium, the envelope is not heated by stable hydrogen burning. The layer is therefore cooler and a thicker helium column is needed to reach ignition conditions. This results in a long and energetic X-ray burst which can last up to half an hour (in 't Zand et al. 2005; Cumming et al. 2006). The duration of the cooling is proportional to the column depth of the layer.

Even more impressive in terms of decay time and energy output are the so-called superbursts that are observable for up to a day, emitting a thousand times more energy than normal type I bursts (Kuulkers 2004). Superbursts are thought to be the result of unstable carbon burning in the ashes of hydrogen and helium burning. A carbon-rich layer is created by helium burning, probably during stable burning. In the presence of hydrogen, the carbon abundance is lowered by normal type I bursts through proton-capture reactions that create heavy isotopes. However, the presence of these heavy elements alters the heat conductivity of the layer, such that the carbon can ignite at lower depths (Cumming & Bildsten 2001). Therefore, it appears that both stable and unstable burning of accreted material are required to produce superbursts (in 't Zand et al. 2003). It typically takes years to form the thick

carbon-rich layer required for superburst ignition. Therefore, superbursts are rare: only 15 have been observed from 10 different sources. Out of these 10 sources, at least one accretes hydrogen-deficient matter (Strohmayer & Brown 2002). The superburst from this source is also the only one for which photospheric radius expansion is inferred (see below). All superbursters exhibit normal type I bursts as well. After the occurrence of a superburst, normal X-ray bursts are quenched for typically one month.

If the peak luminosity of an X-ray burst exceeds the Eddington limit, the photosphere expands. This lowers the effective temperature, sometimes causing the peak of the spectrum to briefly move out of the X-ray bandpass. This is referred to as “photospheric-radius-expansion” (PRE). Since the peak bolometric flux of a PRE burst corresponds to the Eddington luminosity, the observation of these bursts can be used to determine the distance to the source (e.g., Kuulkers et al. 2003).

1.6 IN THIS THESIS

Although the general properties of type I X-ray bursts are well explained by theory, there are still important inconsistencies between the observations and the models. In this thesis we present the results of three observational and one theoretical study which aim to investigate some of these open questions.

We start off in *Chapter 2* by attempting to expand the sample of known superbursts by systematically searching through archival data of the Wide-Field Cameras on board the BeppoSAX satellite. While we do not find any new superbursts, we are able to set lower limits to the recurrence time of superbursts in nine sources. We compare these lower limits to theoretical estimates of the superburst recurrence time as well as observed recurrence times. We consider three sources that have an accretion rate close to the Eddington limit. The lower limit we infer for these sources is long compared to the superburst recurrence times observed for GX 17+2, which has a similar accretion rate (in ‘t Zand et al. 2004a). An important difference between these sources is that only GX 17+2 is known to exhibit normal X-ray bursts. This supports the idea that normal bursts are a prerequisite for obtaining shorter superburst recurrence times (Cumming & Bildsten 2001).

Of the 15 known superbursts, one is observed in a typical *transient* LMXB. In *Chapter 3* we report on the analysis of this unique superburst and find that it poses interesting challenges for the current models. The first question is how a layer of carbon fuel was built. Carbon is mostly produced by stable helium burning during the periods of high

accretion rate and destroyed in X-ray bursts when the accretion rate is lower. Since the periods of high accretion rate occur only once every few years and last ~ 50 days, it is interesting that a thick carbon-rich layer was able to form without being destroyed by the many normal type I bursts. The second challenge to theory is the heating of the carbon-rich layer. This layer is heated by the crust, which in turn is heated during accretion. All other superbursters accreted for over 10 years at a high rate, ensuring that the crust is sufficiently hot. 4U 1608–522, however, accreted during only 55 days prior to the superburst. The latest models predict that the temperature required for carbon-ignition cannot be reached during this short time. Both measurements are inconsistent with current models.

Another relatively rare phenomenon are thermonuclear bursts with short recurrence times. In *Chapter 4* we study double and triple bursts in a long set of observations of the source EXO 0748–676 by the XMM-Newton satellite. In these events two or three type I X-ray bursts take place with recurrence times as short as ten minutes or less. This recurrence time is too short to accrete enough fuel for a burst. We find that the total fluence of a double or triple event is on average larger than the fluence of a single burst. This suggests that not all available fuel is burnt in one burst, allowing for a second or third burst to occur.

An important discrepancy between theory and observations is the critical mass accretion rate above which helium burning is stable. The models find the transition to occur at $\dot{M} \simeq \dot{M}_{\text{Edd}}$ (Fujimoto et al. 1981), while observations suggest the transition occurs at $\dot{M} \simeq 0.1 \dot{M}_{\text{Edd}}$ (van Paradijs et al. 1988; Cornelisse et al. 2003). Models for accreting white dwarfs show that turbulent mixing due to hydrodynamical instabilities increases the stability of nuclear burning (Yoon et al. 2004a). Recent studies suggest that turbulent mixing has a similar effect in neutron stars and that a rotationally induced magnetic field plays an important role in this (Piro & Bildsten 2007). In *Chapter 5* we present a multi-zone numerical model of nuclear burning in the envelope of an accreting neutron star. For the first time differential rotation and magnetic fields are included in such a model. We study the effect of turbulent mixing on the stability of the nuclear burning and find that the transition from unstable to stable burning takes place at a much lower accretion rate than \dot{M}_{Edd} . For many models the effect is substantially stronger than predicted by Piro & Bildsten (2007). If we allow for a heat flux from the crust which is higher by a factor of 2 than assumed in previous studies (but consistent with the recent result of Gupta et al. 2007), we are able to provide a possible explanation for the observed transition at $\dot{M} \simeq 0.1 \dot{M}_{\text{Edd}}$.

1.7 OUTLOOK

Although we gained more insight into thermonuclear burning in the envelopes of accreting neutron stars, it may be clear that many questions remain and new ones have been raised. Here we describe our future ambitions on this subject.

The observation of more superbursts will allow us to place more stringent constraints on their recurrence time, which provides important information on the creation of a carbon-rich layer as well as on the properties of the crust. The sample of superbursts can be increased by searching through large data sets of wide-field instruments.

The superburst from 4U 1608–522 suggested that the crust heated up much quicker than expected by theory. We have set up a campaign of target of opportunity observations with XMM-Newton and Chandra to observe the crustal cooling of this source after a long accretion outburst. This will provide us with more information about the thermal properties of the crust.

For short recurrence-time bursts it remains unknown why fuel is left over from one burst and how it can ignite as a second burst only 10 minutes later. The phenomenon is not limited to the one source we studied. 16 sources exhibit these events (Galloway et al. 2006). We are undertaking a study of all these sources and their bursting behavior to learn more about the circumstances under which short recurrence times occur.

While we demonstrated that the inclusion of turbulent mixing has an important effect on the stability of thermonuclear shell burning, there are other effects that may be of importance but were not considered yet. For example, we studied helium accretion, while most bursters accrete a mixture of hydrogen and helium (Woosley et al. 2004). Also, gravitational settling may play a role (Peng et al. 2007). Furthermore, since we use a one-dimensional model, two dimensional effects, such as latitudinal dependencies and flame spreading are not taken into account (e.g., Cooper & Narayan 2007). The consideration of any of these points in models together with turbulent mixing may prove important in explaining the current open questions.

THE SUPERBURST RECURRENCE TIME IN LUMINOUS PERSISTENT LMXBS

L. Keek, J. J. M. in 't Zand and A. Cumming

Astronomy & Astrophysics 2006, 455, 1031–1036

ABSTRACT Theory and observations favor stable helium burning as the most important means to produce fuel for superbursts on neutron star surfaces. However, all known superbursters exhibit unstable burning as well. This ambiguity prompted us to search for superbursts in data from the BeppoSAX Wide Field Cameras of ten luminous LMXBs, most of which do not exhibit normal type I X-ray bursts. We found no superbursts and determine a lower limit on the recurrence time which varies between 30 and 76 days (90% confidence). All recurrence time limits except one are longer than the observed recurrence time for GX 17+2. This difference can be understood if the mass accretion rate in GX 17+2 is several tens of percent higher than in the other sources; alternatively, the accreted material in GX 17+2 might be hydrogen deficient, leading to larger carbon yields than in the other sources. We compare our results to the latest models of superbursts. As our search method is indiscriminate of the burst ignition scenario, the recurrence time limits may also be applied to other bursts of similar duration and brightness.

2.1 INTRODUCTION

Neutron stars in low-mass X-ray binaries (LMXBs) accrete hydrogen- and helium-rich matter from a sub-solar mass companion star. The gravitational energy that is released when the matter travels to the surface of the neutron star accounts for most of the observable X-ray radiation. The accreted matter forms a layer on the neutron star. When this layer is sufficiently compressed and heated, thermonuclear burning is ignited. The burning can be stable or unstable, depending on e.g. the mass accretion rate. Unstable nuclear burning results in a type I X-ray burst (Grindlay et al. 1976; Belian et al. 1976; Woosley & Taam 1976; Maraschi & Cavaliere 1977). A burst is observed as a fast (1–10 seconds) rise in the flux and a slow (10–1000 seconds), exponential-like decay. Many such bursts have been observed from about 80 sources

(see e.g. in 't Zand et al. 2004b). For reviews see Lewin et al. (1993) and Strohmayer & Bildsten (2006).

Longer X-ray bursts have been observed that have a similar fast rise, but a much longer decay of several hours. These so-called superbursts release about a thousand times more energy than the normal type I X-ray bursts. So far, ten superbursters have been identified, with two exhibiting more than one superburst. For an observational overview, see Kuulkers (2004) (and see also in 't Zand et al. 2004a, Remillard et al. 2005 and Kuulkers 2005 for reports of new superbursters).

Superbursts are ascribed to unstable carbon burning (initiated by $^{12}\text{C} + ^{12}\text{C} \rightarrow ^{20}\text{Ne} + \alpha$) in an 'ocean' of heavy elements which lies between the freshly accreted layer and the neutron star crust (Cumming & Bildsten 2001, Strohmayer & Brown 2002). The carbon and heavy elements are thought to be the products of rp-process hydrogen and helium burning in the accreted layer (see e.g. Schatz et al. 1999, 2003). This model has been fairly successful at reproducing the energetics and recurrence times of superbursts (Cumming & Bildsten 2001; Strohmayer & Brown 2002; Brown 2004; Cooper & Narayan 2005; Cumming et al. 2006), as well as the observed lightcurves and the quenching of normal type I X-ray bursts for about a month following a superburst (Cumming & Macbeth 2004; Cumming et al. 2006).

An open issue is how to produce enough carbon to power a superburst. Carbon fractions of more than 10% are required to reproduce the observed lightcurves of superbursts and to achieve unstable ignition at the accretion rates of approximately $0.1\dot{M}_{\text{Edd}}$ inferred for most of the superbursters (\dot{M}_{Edd} is the Eddington accretion rate). Calculations of rp-process burning show that stable rather than unstable H/He burning is required for such large carbon fractions (Schatz et al. 2003). The reason is that carbon production is only possible by helium burning after the hydrogen has been consumed, since hydrogen readily captures on carbon, processing it to heavy elements. Helium is rapidly consumed at the high temperatures reached during unstable burning. However, in stable burning, the helium burns at a reduced rate so that when the hydrogen has been completely consumed by rp-process burning, there is still some helium left that then burns into carbon. In this way, there is an anti-correlation between the amount of carbon that is produced and the length of the rp-process, or equivalently the average mass of the heavy elements (Schatz et al. 2003).

Observations support the presence of stable burning in superburst sources. In 't Zand et al. (2003) showed that superburst sources preferentially have large values of α , the ratio of the persistent fluence between type I X-ray bursts to the fluence in the type I X-ray burst. Large values of α indicate that not all the nuclear fuel is con-

sumed in bursts, and that stable burning must occur between them. Cornelisse et al. (2003) studied BeppoSAX observations of nine type I X-ray bursters and found that the burst rate drops for luminosities exceeding approximately 10% of the Eddington limit, implying that stable burning is occurring. This critical luminosity is close to the lowest luminosity of superburst sources, and may explain why superbursts have not been seen at accretion rates less than $\sim 0.1\dot{M}_{\text{Edd}}$.

In contrast, the role of unstable burning and the heavy elements produced by the rp-process remains unclear. Observationally, it is true that all superburst sources show type I X-ray bursts. Cumming & Bildsten (2001) pointed out that for a fixed heat flux emerging from the neutron star crust, the heavy nuclei reduce the thermal conductivity of the accumulating ocean, leading to higher temperatures and earlier carbon ignition than previously found in models of pure carbon layers (see e.g. Woosley & Taam 1976). However, Brown (2004) showed by considering the thermal state of the entire neutron star that in fact the thermal state of the core and crust of the neutron star is most important for setting the ignition column¹. Because the flux emerging from the crust changes with the heavy element composition, the overall effect of the heavy elements is much smaller than calculated by Cumming & Bildsten (2001). Nonetheless, the heavy elements do have some effect on the ignition depth, and so it is possible that unstable burning could contribute to the presence of superbursts.

One way to address this issue is to study the several persistently bright LMXBs which either do not or very rarely show type I X-ray bursts. The rapidly accreting source GX 17+2 has already been important for testing carbon ignition models. Cumming & Bildsten (2001) showed that superbursts should occur at rapid accretion rates near Eddington, but with reduced energies and recurrence times. In 't Zand et al. (2004a) identified four superbursts from GX 17+2 which well-matched the predicted recurrence times, although their durations were longer than expected. In this paper, we report on a systematic search for superbursts in BeppoSAX Wide Field Camera data of ten LMXBs with sufficiently high accretion levels. This includes the so-called 'GX' sources: very bright LMXBs with luminosities close to the Eddington limit. We include six sources that never exhibited an X-ray burst as well as four X-ray bursters for comparison purposes, including the known superburster GX 17+2. We compare the behavior of the four most luminous sources Sco X-1, GX 340+0, GX 5-1 and Cyg X-2 to the

¹ This is a very exciting result because it opens up the possibility of using superburst observations as a probe of the neutron star interior (Brown 2004; Cooper & Narayan 2005; Cumming et al. 2006).

equally luminous superburster GX 17+2. For all these sources we find a constraining lower limit on the superburst recurrence time.

2.2 OBSERVATIONS

We search for superbursts in archival data from the Wide Field Cameras (WFC; Jager et al. 1997) on BeppoSAX (Boella et al. 1997a) of ten X-ray sources. The two WFCs were identical coded mask telescopes pointing in opposite directions. They had $40^\circ \times 40^\circ$ fields of view and a $5'$ angular resolution in the 2–25 keV bandpass. They were active between 1996 and 2002. The WFCs carried out a program of semi-yearly campaigns on the Galactic center region. For a review see in 't Zand et al. (2004b). We consider nine sources near the Galactic center and Cyg X-2 (see Table 2.1). The selected sources accrete mass at a comparable rate to the known superbursters. Some of the sources exhibit normal bursts while others do not.

For each source there is 55 to 153 days of observation time accumulated over a period of six years (see Table 2.1). Note that this is not the net exposure time, but includes data gaps due to Earth occultations (typically 36 minutes long and recurring every 96 minutes) and passages through the South Atlantic Anomaly (13 to 26 minutes long). During these data gaps there is no observation of the source. However, the duration of a data gap is short with respect to the expected duration of a superburst. These data gaps are, therefore, not very detrimental to the detection of superbursts. Except for these short datagaps, an uninterrupted period of exposure time is typically 1.5 days long.

To determine the persistent flux in the 0.1–200 keV range of GX 9+9 we use data from the BeppoSAX Narrow-Field Instruments (NFI). Of these instruments we use data from the Low Energy Concentrator Spectrometer (LECS; Parmar et al. 1997; 0.1–10 keV), the Medium Energy Concentrator Spectrometers two and three (MECS; Boella et al. 1997b; 1.3–10 keV) and the Phoswich Detection System (PDS; Frontera et al. 1997; 13–200 keV). For the other sources we obtain a measure of the flux from the literature (see Section 2.5).

2.3 SEARCH FOR SUPERBURSTS

For each source we have 55 to 153 days of observation time while a superburst is typically observable for several hours. From the superbursts thus far detected we know that they are rare, so we expect to find at most a few new superbursts. The search for these consists of an automatic peak-search algorithm and a visual inspection of the data.

Table 2.1: Superburst recurrence time of ten sources. For each source we give the time in days between the first and the last observation t_{span} , the total observation time t_{obs} including data gaps, the flaring fraction, the number of observed superbursts (SBs), whether a source exhibits normal bursts and the (lower limit of the) superburst recurrence time t_{recur} .

Source	$t_{\text{span}}[\text{d}]$	$t_{\text{obs}}[\text{d}]$	flaring	# SBs	burster	$t_{\text{recur}}[\text{d}]$
Sco X-1	1870.03	55.44	16%	0	no	>30
GX 340+0	2062.82	153.20	10%	0	no	>74
GX 349+2	2062.82	129.71	12%	0	no	>66
GX 9+9	2062.57	139.27	8%	0	no	>76
GX 354-0	2062.79	100.97	10%	0	yes	>52
GX 5-1	2062.79	109.95	11%	0	no	>55
GX 9+1	2062.79	103.45	9%	0	no	>53
GX 13+1	2062.79	104.30	9%	0	yes	>55
GX 17+2	2062.80	127.59	16%	4	yes	$30 \pm 15^{\text{a}}$
Cyg X-2	1999.10	109.67	11%	0	yes	>60

^a From in 't Zand et al. (2004a).

We use a lightcurve in the full bandpass at three different time resolutions. The highest time resolution is 16 s. This resolution allows to discriminate between fast and slow rising peaks. A higher time resolution is not useful because the uncertainty in each lightcurve point becomes too large. The next time resolution is 0.02 days (about 0.5 hr). We find this resolution good to resolve superbursts at optimum sensitivity since short features such as normal bursts are averaged out while superbursts are not. The lowest time resolution is 0.1 d. We employ it to measure the non-flaring persistent flux. At this resolution superbursts are largely averaged out while typical variations in the persistent flux are well sampled.

The search algorithm proceeds as follows. At 0.02 d time resolution we check each data point whether it exceeds the persistent flux significantly. Each data point is assigned a measure of the persistent flux through a linear interpolation of the preceding and following 0.1 d-resolution data point. We then check whether the 0.02 d-resolution data point exceeds the persistent flux at 4.4σ significance. We choose 4.4σ since at this level of significance we detect all superbursts of GX 17+2 while limiting the number of false peaks. There are typically

6000 points in a 0.02 d-resolution lightcurve. We expect the number of false peaks exceeding 4.4σ due to Gaussian noise to be 0.06 .

Using the lightcurve at 16 s time resolution we check these peaks visually for superburst characteristics: a fast rise and a slow, exponential-like decay.

The lightcurve may contain features that have the characteristics of a superburst but are flares (in 't Zand et al. 2004a). Flares are thought to result from quick changes in the mass accretion rate. They are generally not expected to be isolated events, but to come in multiples during flaring episodes. Therefore we exclude obvious flaring periods. We identify flaring episodes visually from the light curve. The fraction of the lightcurve that shows flaring is presented in Table 2.1. For the identification of a flaring episode we use a similar argument as in 't Zand et al. (2004a): an interval between two consecutive data points at 0.1 d-resolution is identified as a flaring episode when the root mean square of the count rate at 0.02 d time resolution in that interval exceeds the average root mean square of all intervals by a factor of two. The flaring fractions are on average 11%.

Using this method we reproduce the four superbursts found previously for GX 17+2 as well as the two peaks that were determined to be flares (in 't Zand et al. 2004a). For the other sources we find no superbursts and we determine a lower limit on the superburst recurrence time t_{recur} .

2.4 RECURRENCE TIME

Thus far only two out of ten superbursters exhibited more than one superburst. These are therefore the only sources for which a recurrence time has been directly obtained. From GX 17+2 four superbursts have been observed with an average recurrence time of 30 ± 15 days and from 4U 1636-536 three superburst were observed with recurrence times of 1.75 and 2.9 years (Kuulkers et al. 2004).

To determine the lower limit of the recurrence time for the other nine sources here investigated, we perform Monte Carlo simulations of series of superbursts and cross check those with the WFC observation schedule. We generate the series of onset times, for a given t_{recur} , by first randomly picking the time of the initial superburst between 0 and t_{recur} . Subsequent superburst times are sampled from a Gaussian distribution with a standard deviation σ , centered around a time t_{recur} after the previous superburst. We use the Gaussian distribution to model the variability in the recurrence time resulting from the variability of the mass accretion rate as measured through the flux. For

the nine sources we find from the normalized root mean squared of the flux that σ is between 0.06 and $0.3 t_{\text{recur}}$.

The superburst exponential decay times are randomly sampled between 1 and 6 hours (see review by Kuulkers 2004). As we will show in more detail below, we can take the decay time independently from the wait time since the previous superburst, because we consider decay times longer than the duration of the data gaps. We assume the peak flux to be equivalent to half the Eddington limit of each source. This implies that any superburst is detectable with the WFC for as long as the e-folding decay time.

A given superburst is considered to be detected if at any time of its e-folding decay duration the instrument was observing the source according to the WFC observation schedule, taking into account all data gaps, including those due to Earth occultations and passages through the South Atlantic Anomaly, as well as flaring episodes.

For each source and t_{recur} we perform 100,000 Monte Carlo simulations. With this number of simulations one expects an uncertainty of 0.3% in the obtained value. We determine the percentage of simulations in which at least one superburst is detected. We define the lower limit to the recurrence time to be that value of t_{recur} for which there is a 90% probability of detecting a superburst. The results are provided in Table 2.1. We find lower limits for t_{recur} between 30 and 76 days.

In Figure 2.1 we illustrate the dependence of the superburst detection on the duration from the Monte Carlo simulations. For this we extend the duration range to below 1 hour. This clearly shows that for superburst durations above 1 hour, the presence of short datagaps is not detrimental to the detection of superbursts.

Our aim is to look for superbursts, but in fact our search is not limited to carbon flashes. The search method we use is indiscriminate of the ignition scenario. Other X-ray bursts of sufficient duration and brightness will also be found using our method. Long duration bursts have been observed from several sources (see Cumming et al. 2006 and Kuulkers et al. 2002a). However, the exponential decay time of these bursts is ≤ 600 s, which is shorter than the lightcurve time resolution of 0.02d that we use (see Section 2.3). Therefore we would not have been able to detect these bursts. Note that if a lightcurve at a shorter time resolution is used, such that these long burst are detectable, the limits that can be placed on the recurrence time are far less constraining than for superbursts, since the burst duration is in this case shorter than the data gaps in our observations (see Figure 2.1). Nevertheless, the constraints we find on the recurrence time apply not only to superbursts, but to any type of thermonuclear flashes which are long and bright enough to be detected.

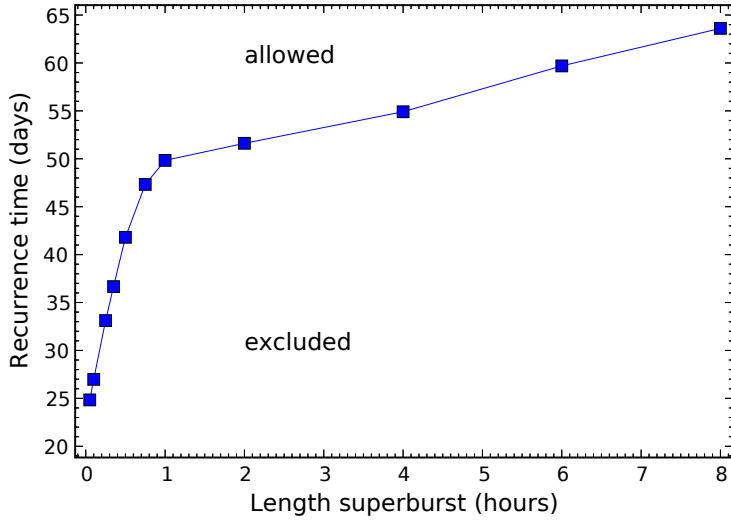


Figure 2.1: Lower limit to the recurrence time at 90% confidence as a function of assumed superburst duration in Monte Carlo simulations. The lower limit drops steeply when the burst duration is of the order of the length of the data gaps or less. Note that our search is insensitive to bursts shorter than 0.5 hour due to our choice of lightcurve time resolution (see Section 2.3).

2.5 MASS ACCRETION RATE

The unstably burning carbon layer to which superbursts are ascribed is formed by the burning of accreted hydrogen and helium. The rate at which the hydrogen and helium are accreted from the companion star plays an important role in whether they burn stably or unstably.

A measurement of the mass accretion rate is most directly done through the X-ray luminosity because the power for the radiation is provided by the liberation of gravitational energy of the accreted matter. However, this is not unambiguous because it is somewhat uncertain what fraction of the liberated energy goes into radiation. It is generally thought that some fraction goes into the kinetic energy of jets. Nevertheless, in the case of neutron star accretors it is not unreasonable to assume that most of the energy goes into radiation (see e.g. Fender 2002).

Another complication involves the determination of the luminosity: distances to LMXBs — needed to translate fluxes to luminosities — are generally poorly known (except for systems in globular clusters). This applies particularly to many of the systems that we study in this paper: persistent LMXBs outside globular clusters without type-I X-ray burst behavior. Systems that exhibit bursts with Eddington-limited fluxes, as diagnosed through photospheric radius expansion, provide a means to find distances with $\approx 30\%$ accuracy (cf., Kuulkers et al. 2003), and transients that turn quiescent may reveal the optical light of the companion star without contamination by optical light from the accretion disk. Neither of these two conditions apply to most of our systems.

A third complication is that for many systems we do not have a broad-band measurement of the X-ray spectrum that is averaged on timescales longer than that of the typical variability to enable a good bolometric correction. Broadband BeppoSAX X-ray spectra have been taken in many cases but almost never for long enough. This situation may change soon with the results of the deep exposures of INTEGRAL on the Galactic bulge.

We attempted to obtain the best broadband flux measurements for the ten systems here studied, see Table 2.2. For nine sources this pertains to values found in the literature from RXTE, BeppoSAX and INTEGRAL observations, and for one system, GX 9+9, we perform the analysis ourselves from BeppoSAX data. The data were taken on April 8, 2000, with exposure times of 23, 50 and 22 ks for LECS, MECS and PDS, respectively. Background spectra are taken from blank field observations for LECS and MECS, at the same detector positions, and from off-source pointings with the PDS. We rebin the spectra to limit

Table 2.2: Flux and luminosity estimates of the 10 investigated sources.

We give the average persistent flux F in the energy range indicated below, the relative variability of the flux as determined from ASM/RXTE measurements, distance d , luminosity L in units of the Eddington luminosity $L_{\text{Edd}} \equiv 2 \cdot 10^{38} \text{ erg s}^{-1}$ and the ignition column depth y . We indicate the uncertainty when given, otherwise we assume a 2% uncertainty. The distances are taken from Christian & Swank (1997) unless indicated otherwise. Christian & Swank take the uncertainty in the distance to be 30%. Jonker & Nelemans (2004) indicate that the uncertainty in the distances they determined is ‘probably very large’. Therefore we use the 30% from Christian & Swank. The uncertainty in the luminosity is dominated by the uncertainty in the distance. Since $L \propto d^2$, the uncertainty in L is 60%. As the ignition column depth is proportional to the luminosity (see equation 2.1), it has the same uncertainty of 60%. In the case of GX 17+2 this has to be added to the indicated uncertainty in y from the spread in the observed recurrence time.

Source	F [$10^{-8} \text{ erg s}^{-1} \text{ cm}^{-2}$]	vari- ability	d [kpc]	L/L_{Edd}	y [$10^{11} \text{ g cm}^{-2}$]
Sco X-1		13%	$2.8 \pm 0.3^{\text{a}}$	$0.9 \pm 0.3^{\text{b}}$	>1.8
GX 340+0	2.67 ^c	15%	<11	<1.9	>9.4
GX 349+2	2.45 ^d	16%	5.0	0.4	>1.8
GX 9+9	$0.8 \pm 0.012^{\text{e}}$	14%	5.0	0.1	>0.6
GX 354-0	0.037 ^f	37%	4.5 ^g	0.05	>0.2
GX 5-1	$2.56 \pm 0.4^{\text{h}}$	8%	<9.0	<1.2	>4.4
GX 9+1	2.1 ⁱ	13%	5 ⁱ	0.3	>1.0
GX 13+1	$0.803 \pm 0.004^{\text{j}}$	7%	7.0	0.2	>0.7
GX 17+2	2.26 ^k	12%	7.5	0.8	1.6 ± 0.8
Cyg X-2	1.3 ^l	23%	8.0	0.5	>2.0

^a Distance from parallax measurements (Bradshaw et al. 1999)

^b From Bradshaw et al. (2003) (2.0–18.2 keV)

^c From Lavagetto et al. (2004) (0.1–200 keV)

^d From Iaria et al. (2004) (0.1–200 keV)

^e From observations with BeppoSAX NFI (0.1–200 keV). See Table 2.3.

^f From Galloway et al. (2003) (2–60 keV)

^g Distance from Jonker & Nelemans (2004) for hydrogen accreting neutron star.

^h From Paizis et al. (2003) (1.5–40 keV). Note that the flux in the 12–20 keV range is obtained through linear interpolation.

ⁱ From Iaria et al. (2005) (0.12–18 keV)

^j From Corbet (2003) (1.5–12 keV) and Revnivtsev et al. (2004) (18–60 keV). Flux in 12–18 keV range obtained through linear interpolation. Total energy range: 1.5–60 keV.

^k From in ‘t Zand et al. (2004a) (0.1–200 keV)

^l From Di Salvo et al. (2002) (0.1–200 keV)

Table 2.3: Flux of GX 9+9 from BeppoSAX NFI observations. As model we use an absorbed disk black body in combination with a comptonized spectrum. We provide the parameters from the best fit of the model to the observed spectrum and the unabsorbed 0.1–200 keV flux.

N_H	$(0.231 \pm 0.003) 10^{22} \text{ cm}^{-2}$
kT_{BB}	$0.853 \pm 0.002 \text{ keV}$
$\text{Flux}_{\text{BB}}(0.1\text{--}200 \text{ keV})$	$(0.33 \pm 0.014) 10^{-8} \text{ erg s}^{-1} \text{ cm}^{-2}$
kT_0	$1.055 \pm 0.003 \text{ keV}$
kT_e	$2.458 \pm 0.004 \text{ keV}$
τ	14.10 ± 0.06
$\text{Flux}_{\text{comptt}}(0.1\text{--}200 \text{ keV})$	$(0.50 \pm 0.04) 10^{-8} \text{ erg s}^{-1} \text{ cm}^{-2}$
χ^2/dof	166/147
$\text{Flux}(0.1\text{--}200 \text{ keV})$	$(0.83 \pm 0.013) 10^{-8} \text{ erg s}^{-1} \text{ cm}^{-2}$

the oversampling of the spectral resolution to 40% of the full-width at half maximum, and to obtain at least 15 photons in each spectral bin. During the spectral analysis, a systematic error of 1% is added in quadrature to the statistical error per spectral bin and the normalization between the three instruments is allowed to vary. We find the generic LMXB spectral model to provide good fits to the data. This model (see e.g. Sidoli et al. 2001) consists of a multi-temperature disk black body (Mitsuda et al. 1984; Makishima et al. 1986) in combination with a comptonized spectrum (Titarchuk 1994; Hua & Titarchuk 1995; Titarchuk & Lyubarskij 1995), both absorbed by cold interstellar matter following the model by Morrison & McCammon (1983). The results of the fit are provided in Table 2.3.

The flux measurements are based on observations which were typically performed during 1.3 days. From one-day averaged ASM/RXTE lightcurves we determine the fractional rms variability for each source, see Table 2.2. We applied the best distance estimates from the literature and determined the ratio of the resulting luminosity and the Eddington luminosity of a canonical neutron star (i.e. $L_{\text{Edd}} \equiv 2 \cdot 10^{38} \text{ erg s}^{-1}$ for a neutron star with a mass of $1.4 M_{\odot}$, a 10 km radius and a hydrogen-rich photosphere). Due to the three sources of uncertainty eluded to above, the resulting ratios are never very accurate, and

we are only able to make a crude distinction between the sources close to one tenth and 100% of the Eddington limit. This inference is in line with the fact that the five sources close to the Eddington limit are the only ones that trace out a Z-shaped curve in a hardness-intensity diagram (e.g., Hasinger & van der Klis 1989). They are Sco X-1, GX 340+0, GX 5-1, GX 17+2 and Cyg X-2. The others are so-called Atoll sources.

2.6 DISCUSSION

We analyzed a large volume of data from the Wide Field Cameras on BeppoSAX of ten luminous LMXBs to search for superbursts. Except for those already reported from GX 17+2 by in 't Zand et al. (2004a), none were found and we set lower limits on the recurrence time of superbursts that range from 30 to 76 days.

One of the conditions for a superburst to occur is a sufficiently large column depth of accumulated matter. The ignition column depth y for a $1.4 M_{\odot}$ neutron star with a 10 km radius, assuming a gravitational redshift $z = 0.31$, is given by (in 't Zand et al. 2004a)

$$y = 2.0 \cdot 10^{11} \text{ g cm}^{-2} \left(\frac{t_{\text{recur}}}{30 \text{ days}} \right) \left(\frac{\dot{m}}{\dot{m}_{\text{Edd}}} \right), \quad (2.1)$$

with $\dot{m}_{\text{(Edd)}}$ the (Eddington limited) mass accretion rate. At a given accretion rate, the lower limit to the recurrence time gives a lower limit to the ignition column depth. Using Equation (2.1) we calculate y (see Table 2.2).

Cumming et al. (2006) investigate several carbon ignition models for superbursts. From these the recurrence time as a function of the mass accretion rate is determined. In Figure 2.2 we compare our lower limits to t_{recur} as well as the observed recurrence times of 4U 1636-536 and GX 17+2 to these models. Looking at what theory predicts, the constraints that we can put on the superburst recurrence time are only meaningful for sources that accrete close to the Eddington limit. For the sources that accrete close to 10% of the Eddington limit the theory predicts for all models a higher t_{recur} than our lower limit. Sco X-1, GX 340+0, GX 5-1 and Cyg X-2 accrete matter at a rate comparable to GX 17+2, namely close to the Eddington limit.

Cumming et al. (2006) discuss the dependence of the ignition of carbon on the heat flux into the superbursting layer from the deeper lying crust: Q_b . At a given accretion rate, the recurrence time is lower for higher Q_b . Therefore a lower limit to t_{recur} , or alternatively to y , gives an upper limit to Q_b for a given model (see Figure 20 in Cumming et al. (2006)). Comparing the lower limit to the ignition column depth of the

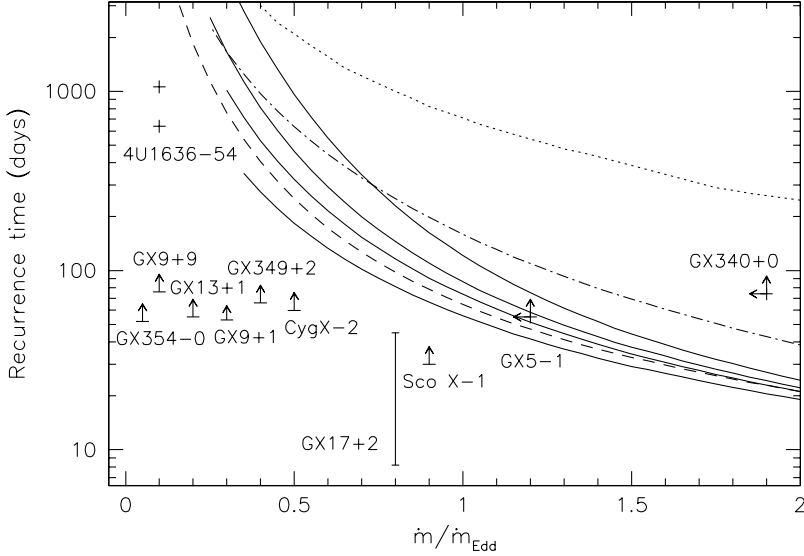


Figure 2.2: Superburst recurrence time as a function of the mass accretion rate in units of the Eddington limited mass accretion rate. We show models from Cumming et al. (2006) and observed recurrence times including our lower limits. The solid curves show results for a model with a disordered crust, a composition of ^{56}Fe and a 20% carbon abundance, without Cooper pairing for four different core neutrino emissivities. The dashed curve is for a model with heavier composition ($A = 104$), the dot-dashed curve has a higher crust conductivity and the dotted curve includes Cooper pair neutrino emission. The curves end at lower \dot{m} where stable carbon burning begins. Note that the uncertainty in the mass accretion rate is at least 60% for most sources (see Table 2.2).

five brightest sources to the results of Cumming et al. (2006) we find $Q_b \lesssim 0.1$ MeV per nucleon for iron composition. However, the large uncertainty in the accretion rate due to the large uncertainty in the distance to these sources prevents us from placing stringent constraints on the models of Cumming et al. (2006).

For GX 340+0, GX 5-1 and Cyg X-2 we found the lower limit to the superburst recurrence time to be about two times the recurrence time of GX 17+2. One of our goals was to learn more about the dependence of superbursts on normal bursting behavior. However, we cannot explain the difference in t_{recur} by the difference in normal type I bursting behavior as both GX 17+2 and Cyg X-2 exhibit bursts, while GX 340+0 and GX 5-1 do not.

From Figure 2.2 we see that, depending on the model, a 35% difference in the mass accretion rate can lead to a two times longer recurrence time. The uncertainty in the mass accretion rate is 60%. Therefore the difference in (lower limit on) t_{recur} could be due to GX 17+2 accreting faster than GX 340+0, GX 5-1 and Cyg X-2.

Another possible explanation for the inferred difference in t_{recur} is that GX 17+2 may differ from the other sources in some aspect which would lower the theoretical curves for this source. The core temperature of GX 17+2 might be higher, which would lead to a lower ignition column depth and therefore a lower recurrence time (see e.g. Figure 11 in Cumming et al. 2006). Alternatively there may be a difference in the hydrogen and helium abundance of the accreted matter. A larger initial helium abundance will lead directly to a larger carbon yield from rp-process burning (Schatz et al. 2003). Cumming & Bildsten (2001) find that the amount of carbon required to achieve unstable ignition at accretion rates close to the Eddington limit is approximately 3–5%. The presence of observable superbursts in GX 17+2 might indicate that the accreted material in this source is hydrogen deficient, allowing sufficient carbon to be made, whereas too little carbon is made in other sources to result in a superburst (a similar suggestion is done by Cooper et al. 2006). Another effect, which goes in the opposite direction, is that a lower initial hydrogen abundance will lead to a less extensive rp-process, giving less massive heavy elements, which increases the carbon ignition depth because of the lower opacity of the accumulating fuel layer (Cumming & Bildsten 2001). However, Brown (2004) shows that this effect is smaller than initially thought. At present only one superburster, the ultracompact system 4U 1820-30, is assumed to accrete hydrogen-poor matter. In this case, the extremely short orbital period of only 11.4 minutes (Stella et al. 1987) implies that the hydrogen mass fraction is $X \lesssim 10\%$, consistent with the very luminous and energetic superburst observed from this source (Cumming

2003). Another case of a superburst accreting hydrogen-deficient matter is possibly the ultracompact system 4U 0614+091 (see e.g. Nelemans et al. 2004) of which most recently a superburst was observed (Kuulkers 2005).

2.7 CONCLUSION

We searched for superbursts from ten bright LMXBs. None were found but the four known superbursts from GX 17+2. For the other sources we obtain lower limits to the recurrence time and the ignition column density. Comparing this lower limit for the five most luminous sources, Sco X-1, GX 340+0, GX 5-1, GX 17+2 and Cyg X-2, to the models by Cumming et al. (2006) $Q_b \lesssim 0.1$ MeV per nucleon is required. Due to the large uncertainty in the distance to these sources, the uncertainty in the mass accretion rate is large as well. This prevents us from placing firm constraints on the predictions by Cumming et al. (2006). As our search method is indiscriminate of the burst ignition scenario, the recurrence time limits may also be applied to other bursts of similar duration and brightness.

The four luminous non-superbursters have a mass accretion rate comparable to the luminous superburst GX 17+2. For three of these sources we find a lower limit to the recurrence time that is twice as long as the observed average t_{recur} of GX 17+2. Most likely this difference is due to GX 17+2 accreting faster than the other sources and therefore GX 17+2 has a lower t_{recur} . However, we are unable to determine whether this is the case because of the large uncertainty in the mass accretion rate.

We found no superbursts in the six non-bursting sources we considered, which confirms the current observational view of superbursters, i.e. all known superbursters exhibit normal type I X-ray bursts as well. This supports the suggestion that both stable and unstable burning of hydrogen and helium are necessary to produce the fuel for superbursts.

To better constrain models of neutron star interior physics, more long term monitoring observations of (candidate) superbursters are necessary. As superbursts have a long recurrence time, a long exposure time is required for each observed source. The planned mission MIRAX (Braga et al. 2004) will be the most suited for such a task. MIRAX will have on board the spare flight unit of the BeppoSAX WFCs as well as two hard (10–200 keV) X-ray cameras. The aim of MIRAX is to perform continuous broadband observations of the Galactic center during nine months per year. This will provide a high probability to observe

any superbursts that have a recurrence time less than approximately these nine months, which includes the predicted recurrence time of many models shown in Figure 2.2 for sources which accrete close to the Eddington limit. The latest observations of superbursts (Remillard et al. 2005; Kuulkers 2005) were done with RXTE/ASM, which observes 80% of the sky each 90 minutes. Due to a time resolution of 90 s the short (1–10 s) burst rise cannot be observed, which makes it more difficult to distinguish between a superburst and a flare. Observations from MIRAX will have a time resolution better than 0.5 ms which is more than adequate to observe the rise of superbursts.

FIRST SUPERBURST FROM A CLASSICAL LOW-MASS X-RAY BINARY TRANSIENT

L. Keek, J. J. M. in 't Zand, E. Kuulkers, A. Cumming, E. F. Brown and
M. Suzuki

Astronomy & Astrophysics 2008, 479, 177–188

ABSTRACT We report the analysis of the first superburst from a transiently accreting neutron star system with the All-Sky Monitor (ASM) on the Rossi X-ray Timing Explorer. The superburst occurred 55 days after the onset of an accretion outburst in 4U 1608-522. During that time interval, the accretion rate was at least 7% of the Eddington limit. The peak flux of the superburst is 22 to 45% of the Eddington limit, and its radiation energy output is between $4 \cdot 10^{41}$ and $9 \cdot 10^{41}$ erg for a distance of 3.2 kpc. Fits of cooling models to the superburst light curve indicate an ignition column depth between $1.5 \cdot 10^{12}$ and $4.1 \cdot 10^{12}$ g cm⁻². Extrapolating the accretion history observed by the ASM, we derive that this column was accreted over a period of 26 to 72 years. The superburst characteristics are consistent with those seen in other superbursting low-mass X-ray binaries. However, the transient nature of the hosting binary presents significant challenges for superburst theory, requiring additional ingredients for the models. The carbon that fuels the superburst is thought to be produced mostly during the accretion outbursts and destroyed in the frequent type I X-ray bursts. Mixing and sedimentation of the elements in the neutron star envelope may significantly influence the balance between the creation and destruction of carbon. Furthermore, predictions for the temperature of the neutron star crust fail to reach the values required for the ignition of carbon at the inferred column depth.

3.1 INTRODUCTION

4U 1608-522 is a bright low-mass X-ray binary (LMXB) with a neutron-star (NS) primary (Belian et al. 1976; Tananbaum et al. 1976). QX Nor was identified by Grindlay & Liller (1978) as the optical counterpart. The accretion onto the neutron star is transient (Lochner & Roussel-Dupre 1994 and references therein) and the outburst behavior complex. Three main flux states can be resolved in 4U 1608-522 (Wachter et al.

2002): an outburst state, a low-intensity state and a true quiescent state. In contrast to many other LMXB transients, its true quiescent state has a relatively low duty cycle of only about 50%. Wachter et al. speculate that the mass transfer rate might be fluctuating around the critical threshold separating stable accretion systems from true transient systems, possibly due to varying stellar spots on the donor star or to a varying vertical accretion disk structure which may change the irradiation and, thus, the mass transfer rate through the disk. Wachter et al. (2002) also identified a modulation in the optical light curve with a period of 12.9 hr which they suspect to be near the orbital period. Thus, the donor is probably hydrogen-rich.

4U 1608-522 exhibits so-called type I X-ray bursts (Belian et al. 1976; Tananbaum et al. 1976). These are understood to result from thermonuclear shell flashes on the surfaces of NSs of layers of accreted hydrogen and helium (Woosley & Taam 1976; Maraschi & Cavaliere 1977; for reviews, see Lewin et al. 1993 and Strohmayer & Bildsten 2006). The flash layers heat up during a fraction of a second and cool down in an exponential-like manner lasting 10 s to a few minutes. As a result, a spectrum may be observed which is typically well fit by a black body with a temperature decreasing from a peak of typically $kT = 2$ to 3 keV and an emission region similar in size to what is expected for a NS (Swank et al. 1977). Some nuclear energy generation may persist throughout the cooling phase, prolonging the bursts somewhat. A number of bursts exhibit photospheric radius expansion (PRE) where the burst flux is thought to reach the Eddington limit. From the observation of PRE bursts from 4U 1608-522, Galloway et al. (2006) derived a distance to this source of 3.2 ± 0.3 kpc. During 5 PRE bursts, burst oscillations were detected at 619 Hz, which implies the fastest known spin frequency for accreting neutron stars (Galloway et al. 2006), with the possible exception of XTE J1739-285 (Kaaret et al. 2007).

Since a few years a different kind of type I X-ray burst is detected in about 10% of all bursters: so-called ‘superbursts’ (Cornelisse et al. 2000; Strohmayer & Brown 2002). These are about 10^3 times more energetic and last for hours to a day. They are thought to result from flashes of carbon-rich layers (Strohmayer & Brown 2002; Cumming & Bildsten 2001). These layers are presumed to be much further down in the neutron star than those where ordinary X-ray bursts occur, which would explain the longer duration. It has been observed that superbursts influence the normal bursting behavior. Each time when the start of a superburst has been observed with sufficient statistics a precursor burst was seen (see e.g. Strohmayer & Brown 2002). Furthermore, after the superburst the normal bursting behavior is quenched for approximately one month (see e.g. Kuulkers et al. 2002b).

Superbursts have so far only been seen in systems in which the NS has been continuously accreting for at least 10 yr (Kuulkers 2004; in 't Zand et al. 2004a), although not in every such system (Keek et al. 2006, see Chapter 2). Here we present a superburst from 4U 1608-522, which represents the first case for a 'classical' transient. A superburst has also been observed from the transient source KS 1731-260 (Kuulkers et al. 2002b). However, unlike KS 1731-260, 4U 1608-522 exhibits states of high flux with a duration that is short with respect to the expected superburst recurrence time. This may have interesting consequences for the theory of superbursts, because the different states of the transient allow us to study different levels of carbon production and burning in one source. Perhaps most importantly, whereas the crust in KS 1731-260 is expected to have been heated significantly out of thermal equilibrium with the core during its long outburst, the crust of 4U 1608-522 is not expected to be significantly heated during its short outbursts. This presents a significant challenge to carbon ignition models for superbursts, which require a hot crust to achieve ignition at the depths inferred from observations of superbursts. Despite these differences, the superburst from 4U 1608-522 has similar properties to superbursts from other sources.

This chapter is organized as follows. First we describe the observations and spectral calibration in Sect. 3.2. In Sect. 3.3 we report on an analysis of the X-ray burst behavior of 4U 1608-522 as a function of its apparent mass accretion rate. Next, in Sect. 3.4, we present the analysis of the detected superburst. Finally, we discuss the implications of the results for superburst theory in Sect. 3.5. Initial reports of this superburst appeared in Remillard et al. (2005) and Kuulkers (2005).

3.2 OBSERVATIONS AND SPECTRAL CALIBRATION

3.2.1 *Observations*

To study both the long-term accretion and bursting behavior of 4U 1608-522, as well as the superburst, we employ observations performed with multiple instruments on-board four X-ray observatories.

The All-Sky Monitor (ASM) on the Rossi X-ray Timing Explorer (RXTE) (Levine et al. 1996) consists of three Scanning Shadow Cameras (SSC), each containing a position-sensitive proportional counter. The cameras are mounted on a rotating drive. Data are accumulated in so-called dwells of 90 seconds. After each dwell the rotation drive changes the orientation of the SSCs. Spectral information is available from three channels with corresponding energy ranges of roughly 1.5–

3, 3–5 and 5–12 keV. After the launch of RXTE in December 1996 until November 2006, the ASM observed 4U 1608-522 for a total of 2.8 Ms. On May 5th 2005 the ASM observed the superburst from 4U 1608-522.

RXTE also carries the Proportional Counter Array (PCA). The PCA consists of five proportional counter units (PCUs) with a total geometric area of 8000 cm² and has a bandpass of 1 to 60 keV (Jahoda et al. 2006). 4U 1608-522 was observed for 1.6 Ms in total, mostly when it was out of quiescence (e.g., van Straaten et al. 2003; Gierliński & Done 2002).

The BeppoSAX observatory (Boella et al. 1997a) was launched in April 1996 and carried two Wide Field Camera's (WFCs) as well as four Narrow Field Instruments (NFI). The WFCs (Jager et al. 1997) are coded mask aperture cameras with a band pass of 2–28 keV. During the six year lifespan of BeppoSAX a campaign of semi-yearly observations of the Galactic Center were carried out, which resulted in an exposure time of 3.8 Ms for 4U 1608-522.

The BeppoSAX NFI performed two pointed observations of 4U 1608-522. The first observation was performed during an outburst on February 28 1998. In this paper we analyze the broad-band spectrum obtained with the following NFI in the indicated energy bands: the Low Energy Concentrator Spectrometer (LECS; Parmar et al. 1997; 0.12–4 keV), the Medium Energy Concentrator Spectrometer (MECS; Boella et al. 1997b; 1.8–10 keV) and the Phoswich Detection System (PDS; Frontera et al. 1997; 15–220 keV). The exposure time depends on the instrument and is 30 ks for the MECS. The second observation took place when 4U 1608-522 was in quiescence. Since we are interested in the production of carbon from accreted matter, we forgo the analysis of the data from this observation.

On May 5th 2005, 33 minutes before the start of the ASM observation of the superburst, the High Energy Transient Explorer 2 (HETE-2; Ricker et al. 2003) observed a flare from 4U 1608-522 with two instruments: the Wide field X-ray Monitor (WXM; Shirasaki et al. 2003) with a 2 to 25 keV band pass and the French Gamma Telescope (FREGATE; Atteia et al. 2003) which has a band pass of 6 to 400 keV.

The International Gamma-Ray Astrophysics Laboratory (INTEGRAL; Winkler et al. 2003) was launched in October 2002. The Imager on Board the Integral Satellite (IBIS; Ubertini et al. 2003) is a coded aperture camera containing two detectors. We use results obtained with the INTEGRAL Soft Gamma-Ray Imager (ISGRI; Lebrun et al. 2003) detector, which has an energy range from 15 to about 500 keV. IBIS/ISGRI has observed 4U 1608-522 up to September 2005 for a total of 6.3 Ms.

In this paper we analyze spectra using version 11.2.0 of the XSPEC software package (Arnaud 1996).

3.2.2 Spectral calibration of the ASM

The spectral response of the ASM detectors is not well defined. A pre-flight effective area array is available, while a redistribution matrix is not (see discussion in Kuulkers 2002). We construct such a matrix by modeling, for an infalling photon with a certain energy, the energy distribution over the three channels by a Gaussian with a full width at half maximum of 20% of the centroid energy, which is a typical width for the type of proportional counter used in the ASM (e.g. Fraser 1989). The response matrix thus obtained is merely a first order estimate, but suffices for rough calculations.

We employ the Crab source to investigate the accuracy of our response matrix. The average count rate over all ASM observations from this source in the full 1.5–12 keV band-pass is 75.4 c s^{-1} . The X-ray spectrum can be described by an absorbed power law. Kirsch et al. (2005) performed simultaneous model fits to Crab spectra obtained with 22 X-ray instruments. Using the results of these fits in the 2–10 keV range, our response matrix¹ predicts an ASM 1.5–12 keV count rate of 70.5 c s^{-1} . Therefore, when performing spectral analyses using this matrix, the normalization of the models needs to be corrected by a factor 1.07 to account for this discrepancy. Note that in principle this factor can be different for each of the three SSCs and can vary with time. However, we find that in a time interval of 100 days centered at the start of the superburst the difference in Crab count rate between any two SSCs never exceeds the 3σ level.

Apart from the accuracy in predicting the count rate of the Crab, we also investigate how well our response matrix can reproduce the typical model parameters that are found by fitting an absorbed power law to the three-channel spectral data. We extracted a spectrum from all the ASM data on the Crab available at the time of writing. We fix the hydrogen absorption column density at the value of $N_{\text{H}} = 0.45 \cdot 10^{22} \text{ cm}^{-2}$, as found by Kirsch et al. (2005) (in the 0.1–1000 keV energy range). Following Kirsch et al., we use the abundances found by Wilms et al. (2000) and cross sections from Verner et al. (1996). Leaving free the power law index and the normalization, we do not find an acceptable agreement with the data. Only if we add in quadrature 10% of the flux to the uncertainty of each data point are we able to obtain an acceptable fit with $\chi^2_{\text{red}} \simeq 1$. Taking into account the correction factor derived previously, we find the best fit with a photon index of $\Gamma = 2.01 \pm 0.12$ and a normalization of $N_{\text{powerlaw}} = 9 \pm 2 \text{ pho}$

¹ Kuulkers (2002) finds the count rate is over-predicted. This is due to a different choice of values for the spectral model parameters.

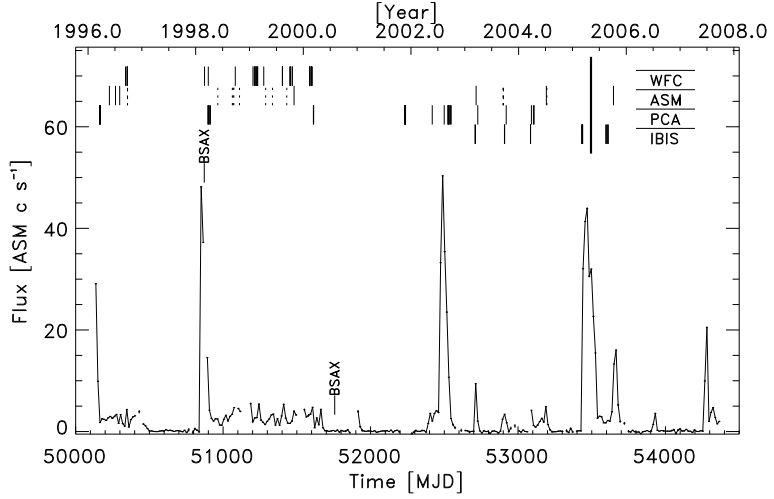


Figure 3.1: 1.5–12 keV RXTE-ASM light curve of 4U 1608-522 at a 2-week time resolution. Data points with errors in excess of 0.5 c s^{-1} were excluded from this plot. The connecting line is broken if data points are more than 2 weeks apart. The vertical lines indicate 37 bursts detected with the WFC, 19 with the ASM (dashed lines indicate tentative bursts), 31 with the PCA (Galloway et al. 2006) and 19 with the IBIS/ISGRI (Chelovekov et al. 2007). The long vertical line indicates the time of the superburst. ‘BSAX’ indicates the times of two BeppoSAX observations.

tons $\text{keV}^{-1}\text{cm}^{-2}\text{s}^{-1}$, which is consistent with the results from Kirsch et al. (2005). The uncertainty in N_{powerlaw} is large, because by definition N_{powerlaw} is the photon flux at 1 keV, which is outside of the ASM energy range. The XSPEC power law model ‘pegpwlw’ uses a user-defined energy range for the normalization. Employing the ASM bandpass gives an uncertainty in the normalization of 6%.

3.3 HISTORY OF ACCRETION AND X-RAY BURST ACTIVITY

3.3.1 Long-term light curve

Figure 3.1 shows the 1.5–12 keV ASM light curve of 4U 1608-522. Clearly visible are the three states identified by Wachter et al. (2002; see Sect.

3.1). Four major outbursts, where the peak photon count rates was in excess of 20 c s^{-1} for more than one month, are visible in the 11-year time span of the observations (see Sect. 3.3.2 for a discussion on the selection criterion). The first outburst was ongoing at the start of the ASM observations and lasted until 60 days afterward, with fluxes in excess of 20 c s^{-1} . The following outbursts lasted with fluxes above 20 c s^{-1} for 44 d (MJD 50848-50892), 48 d (MJD 52475-52523), and 80 d (MJD 53438-53518), respectively. There are also five minor outbursts, after the two latter major outbursts. The low-intensity states are visible in the first half of the mission. From comparing the first half and the latter half of the light curve, it appears that either a low-intensity state emerges after a major outburst, or a series of minor outbursts. This characteristic is only now apparent, after 11 years of observation (Wachter et al. 2002 only considered the first 5 years of the data set). We determined the average flux over the complete ASM data to be $2.466 \pm 0.006 \text{ c s}^{-1}$. This is about 2% of the flux reached during the brightest bursts seen in the ASM.

3.3.2 *Accretion rate*

When matter is accreted onto the neutron star surface, some of the accretion energy and/or some of the material may leave in a jet. If these losses are significant, the persistent flux is not a good tracer of the mass accretion rate \dot{M} . For black-hole X-ray binaries, Fender et al. (2005) argue that jets are not present during the high soft state. It is during the high soft state of 4U 1608-522 that we are particularly interested in the precise value of the accretion rate. Therefore, assuming that the same holds true for neutron star binaries, in this paper we will assume there are no losses through a jet and that the persistent flux is a good measure for \dot{M} . Expressed as a fraction of the Eddington-limited mass accretion rate \dot{M}_{Edd} , which is $\dot{M}_{\text{Edd}} = 2 \cdot 10^{-8} M_{\odot} \text{ yr}^{-1}$ for a canonical hydrogen-accreting neutron star with a mass of $1.4 M_{\odot}$, it can simply be derived as $\dot{M}/\dot{M}_{\text{Edd}} = F/F_{\text{Edd}}$, with F the bolometric flux and F_{Edd} the Eddington-limited flux. We will determine the bolometric flux below. The Eddington-limited flux is exhibited during photospheric radius expansion (PRE) bursts. RXTE PCA observed 12 such bursts (Galloway et al. 2006). The mean unabsorbed bolometric peak flux of these bursts is $F_{\text{Edd}} = (1.32 \pm 0.14) 10^{-7} \text{ erg s}^{-1} \text{ cm}^{-2}$.

Van Straaten et al. (2003) make an extensive study of the spectral changes of 4U 1608-522 during the various states and the associated timing properties. They conclude that 4U 1608-522 is an Atoll source that exhibits the ‘banana’ state during outbursts and moves in the

color-color diagram to the ‘extreme island’ state when the flux goes to levels of the low-intensity state. The distinguishing parameter is the ‘hard color’ (i.e., the flux between 9.7 and 16.0 keV divided by the flux between 6.0 and 9.7 keV) which is about 1.15 in the extreme island state and 0.55 in the banana state. This implies that one-band measurements, such as the ASM count rates, are not an accurate measure of the bolometric flux, let alone the accretion rate. In order to derive the bolometric flux during the low and high accretion states, we analyze the broad-band outburst-observation with BeppoSAX as well as a large number of observations with the RXTE PCA.

Two broad-band observations were carried out during the ASM coverage with BeppoSAX, one of which during outburst (for the timing of these observations, see Fig. 3.1). To determine the flux during this observation we analyze spectra obtained with the LECS, MECS and PDS. We subtract background spectra taken from blank field observations at the same detector positions for the LECS and MECS spectra, while for the PDS off-source pointings are used as background. The spectra are rebinned to obtain at least 15 photons in each bin while sampling the instrument resolution with at most 3 channels at all energies, to ensure the applicability of the χ^2 statistic. An error of 1% is added in quadrature to the statistical error per bin to account for systematic uncertainties. This is common practice in BeppoSAX analyses (Fiore et al. 1999). We fit the data from all three instruments simultaneously with the generic LMXB model (see e.g. Sidoli et al. 2001), consisting of a multi-temperature disk black body (Mitsuda et al. 1984; Makishima et al. 1986; ‘diskbb’ in XSPEC) in combination with a comptonized spectrum (Titarchuk 1994; Hua & Titarchuk 1995; Titarchuk & Lyubarskij 1995; ‘comptt’ in XSPEC), both absorbed by cold interstellar matter following the model by Balucinska-Church & McCammon (1992) (‘phabs’ in XSPEC). During the spectral analysis we allow the normalization between the three instruments to vary and find that the best fit values are within acceptable limits: the normalization between the LECS and MECS is 0.897 ± 0.003 , while 0.7 to 1.0 is acceptable; between the PDS and MECS the normalization is 1.21 ± 0.04 , while 1.1 to 1.3 is acceptable (Fiore et al. 1999). The results of the fit as well as the derived flux are provided in Table 3.1. The flux is determined by extrapolating the model from the observed range to 0.01–300 keV. Extrapolating the model further while correcting for the interstellar absorption does not lead to a significant increase in flux. Under the assumption that no other features in the spectrum other than those we modeled have a substantial flux contribution, we refer to this as the bolometric flux. From the average ASM flux during this observation, we find that 1 ASM c s⁻¹ is equivalent to $(4.4 \pm 0.2) \cdot 10^{-10}$ erg s⁻¹cm⁻².

Table 3.1: Parameters and 1σ uncertainties of fitting the outburst spectrum of 4U 1608-522 from BeppoSAX NFI observations on 28 Feb 1998 with an absorbed disk black body^a and comptonized^b model.

N_{H}	$(8.91 \pm 0.05) 10^{21} \text{ cm}^{-2}$
kT_{BB}	$2.38 \pm 0.07 \text{ keV}$
N_{BB}	18.3 ± 0.9
kT_0	$0.478 \pm 0.005 \text{ keV}$
kT_e	$3.6 \pm 0.2 \text{ keV}$
τ	3.7 ± 0.2
N_{Comptt}	0.40 ± 0.02
$\chi^2_{\text{red}}/\text{dof}$	1.40/160
Flux (0.01–300 keV) ^c	$(1.75 \pm 0.10) 10^{-8} \text{ erg s}^{-1} \text{ cm}^{-2}$
ASM count rate ^d	$39.4 \pm 0.9 \text{ c s}^{-1}$

^a Disk black body model parameters: kT_{BB} is the temperature at the inner disk radius R_{in} and $N_{\text{BB}} \equiv (R_{\text{in}}^2/d_{10}^2) \cos \theta$ the normalization, with R_{in} in units of km, d_{10} the source distance in units of 10 kpc and θ the inclination.

^b Comptonized model parameters: kT_0 , kT_e are resp. the seed photon and plasma temperature, τ the plasma optical depth for a disk geometry and N_{Comptt} the normalization.

^c Unabsorbed 0.01–300 keV flux, which we take to be bolometric.

^d Average ASM count rate during the observation.

To further study the bolometric correction that may be applied to the ASM data as a function of the persistent flux, we employ 160 observations carried out with the RXTE PCA between March 1996 and February 2006. The PCA spectra are extracted from the standard products, with exposure times between 96 s and 13 ks and a total exposure of 310 ks. They are modeled between 3 and 40 keV (the calibrated bandpass) with a generic model consisting of a black body and a cutoff power law, both absorbed following the model by Morrison & McCammon (1983) with $N_{\text{H}} = 8 \cdot 10^{21} \text{ cm}^{-2}$. The resulting fits are acceptable in 144 cases with $\chi^2_{\text{red}} < 2$; in the remaining cases χ^2_{red} rises to up to 6. Despite the sometimes bad fit, we employ all observations since we are interested only in obtaining constraints for the bolometric correction and not in physical implications of the spectral model. The fit outcome is tested leaving N_{H} free: no evidence is found for fluctuations in N_{H} above $5 \cdot 10^{22} \text{ cm}^{-2}$. We determine the photon flux between 1.5 and 12 keV before correcting for absorption and normalize it to observed ASM fluxes through calibration with Crab fluxes and by cross correlating the PCA measurements for 4U 1608-522 with contemporaneous ASM fluxes. We calculate the 0.1 to 100 keV energy flux after a correction for absorption. Obviously, this implies a fairly large extrapolation from the 3 to 40 keV PCA bandpass and we check how much flux is found outside that bandpass. It varies between 10% at the brightest state to 60% in the faintest state. This indicates what the maximum error is of the extrapolation. The results are plotted in Fig. 3.2. It clearly shows the two states identified by van Straaten et al. (2003). The boundary between both states is at 5 to 10 ASM c s^{-1} . At the bright state, when the spectrum is relatively soft, 1 ASM c s^{-1} is equivalent to $5.5 \cdot 10^{-10} \text{ erg s}^{-1} \text{ cm}^{-2}$ and at the hard faint state to $1.0 \cdot 10^{-9} \text{ erg s}^{-1} \text{ cm}^{-2}$. For the bright state we can calibrate this result using the BeppoSAX broadband observation of the 1998 outburst from which we derived above the equivalence of 1 ASM c s^{-1} to $(4.4 \pm 0.2) \cdot 10^{-10} \text{ erg s}^{-1} \text{ cm}^{-2}$. We use this number as conversion factor for the high flux state.

Applying the bolometric correction factors to the ASM flux, we find that the average persistent flux was $(2.313 \pm 0.013) 10^{-9} \text{ erg cm}^{-2} \text{ s}^{-1}$, while the peak flux reached during the three large outbursts was $2.2 \cdot 10^{-8}$ to $3.0 \cdot 10^{-8} \text{ erg cm}^{-2} \text{ s}^{-1}$. The mass accretion rate is on average $\dot{M}/\dot{M}_{\text{Edd}} = (1.8 \pm 0.2) 10^{-2}$ and 0.17 to 0.23 in the peaks of the outbursts.

Using the conversion factor of ASM counts to bolometric flux for count rates above 10 c s^{-1} we determine the fluence of the three major outbursts observed by the ASM for the duration that the count rate exceeded 20 c s^{-1} . For the last outburst we also determined the fluence

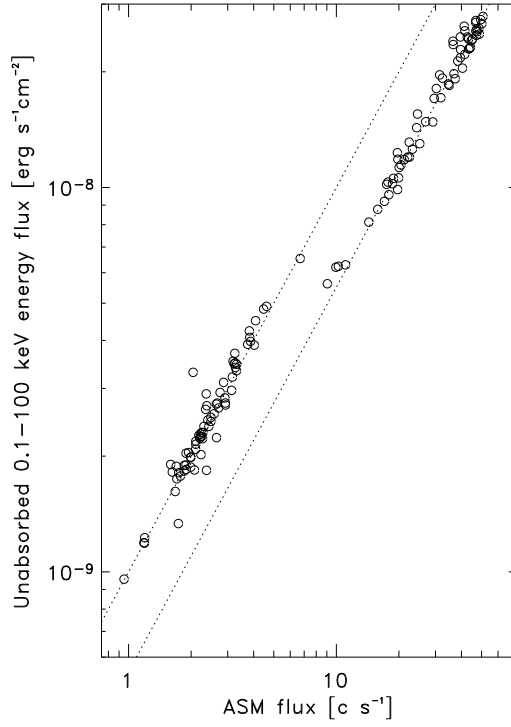


Figure 3.2: Flux as a function of the ASM count rate. The distinction between the two spectral states is clearly visible. The two lines are not fits, but act as guides to distinguish the two states.

Table 3.2: Outbursts properties. Between parentheses we give the 1σ uncertainties in the least significant digit(s).

Outburst	Start time ^a (MJD)	Duration ^a (days)	Fluence (10^{-2} erg cm $^{-2}$)	Energy ^b (10^{44} erg)	Peak Flux ^c (10^{-8} erg s $^{-1}$ cm $^{-2}$)	Peak $\dot{M}/\dot{M}_{\text{Edd}}$ ^d
1	50848.0	44.0	6.3(3)	0.77(15)	3.0(2)	0.23(3)
2	52475.0	48.0	6.9(3)	0.85(16)	2.6(2)	0.20(3)
3	53437.5	79.5	10.4(5)	1.3(2)	2.24(19)	0.17(2)
3 before SB	53437.5	57.6	8.2(4)	1.01(19)	2.24(19)	0.17(2)

^a Start time and duration of time interval when the outburst flux exceeds 20 ASM c s $^{-1}$.

^b Energy calculated from fluence using distance $d = 3.2 \pm 0.3$ kpc.

^c Unabsorbed bolometric peak flux determined from the 1-day ASM light curve (10^{-8} erg s $^{-1}$ cm $^{-2}$).

^d Peak mass accretion rate in units of the Eddington limit assuming a $1.4 M_{\odot}$ neutron star.

up to the moment that the superburst occurred. 20 c s^{-1} corresponds to an accretion rate of $\dot{M}/\dot{M}_{\text{Edd}} = (6.7 \pm 0.8)10^{-2}$ and is chosen as a lower limit since it is close to the value of 0.1 that is required for the production of carbon (Cumming & Bildsten 2001), while selecting the periods of high flux in one interval for each outburst. The bolometric fluences as well as the peak fluxes during the outbursts are presented in Table 3.2.

3.3.3 Long-term bursting behavior

Indicated in Fig. 3.1 are the bursts detected from 4U 1608-522 with the WFC on BeppoSAX until the mission ended in April 2002, the IBIS/ISGRI on INTEGRAL until September 2005 (Chelovekov et al. 2007), the PCA (Galloway et al. 2006) and the ASM on RXTE. One burst was detected by both the WFC and PCA. The ASM bursts are identified through 1) searching individual 90-sec average dwell data of 4U 1608-522 for isolated high points that are at least 3σ above a 100-day running average, resulting in roughly 200 burst candidates; 2) studying the raw 1-sec resolution light curves of the candidate dwells, to eliminate candidates that have no clear flare feature with a time scale smaller than the 90-s dwell time; 3) searching for flares with clear fast-rise exponential-decay profiles, resulting in the identification of 7 certain bursts. The remaining 12 candidates are classified as tentative bursts from 4U 1608-522.

For studying the bursting behavior as a function of the persistent flux, Fig. 3.3 shows a histogram of the ASM-measured persistent flux when a burst is seen for all bursts observed with the WFC, PCA and IBIS/ISGRI as well as the certain bursts observed with the ASM. There is the suggestion that bursts are rare during major outbursts while much more frequent during the extended low-intensity states during MJD 50150–50500 and 50897–51800. Quantitatively, however, the data are inconclusive in this respect. The PCA data set is somewhat biased, because those observations were targeted at 4U 1608-522 mainly when it was in outburst. The other data sets are serendipitous and, therefore, present an objective view of the bursting behavior. The WFC exposure time during major outbursts is 21.3 times smaller than during low-intensity states, while the ratio in the number of bursts is 1 to 36. 2 out of 19 bursts observed by IBIS/ISGRI take place during a major outburst, while the source is observed in outburst during 12.7% of the exposure time. The ASM data are also inconclusive: 2 out of 19 bursts occurred at 1-day average fluxes of 10 c s^{-1} while the fraction of the total time spent in that flux regime is 7.4%. The WFC, PCA, IBIS/ISGRI

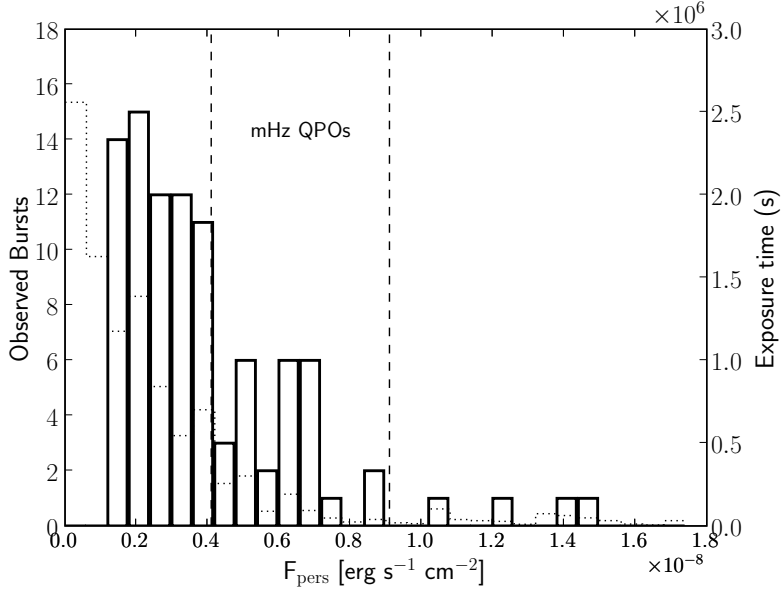


Figure 3.3: Number of observed bursts (*solid line*) as a function of persistent flux F_{pers} . For the latter we use the average ASM count rate in a one-day interval around the moment the burst occurred converted to bolometric flux. This includes all bursts observed with BeppoSAX WFC, RXTE PCA, INTEGRAL IBIS/ISGRI as well as the clear bursts identified in the RXTE ASM light curve. The *dashed lines* indicate the region of F_{pers} where Revnivtsev et al. (2001) observed mHz QPOs (see Sect. 3.5.4). The *dotted line* represents the total PCA, WFC, IBIS/ISGRI and ASM exposure time as a function of the ASM count rate. For PCA, WFC and IBIS/ISGRI observations we use the average ASM count rate during an observation. Together with the burst histogram, one observes that the burst rate does not vary significantly as a function of accretion rate in the range where type I bursts occur.

and ASM light curves exhibit bursts with an average recurrence time of, respectively, 1.19, 0.60, 3.79 and 1.71 days.

The bursting behavior is characterized by α : the ratio of persistent fluence between bursts and the burst fluence. Using the PCA observations we calculate the average value of α both for the outbursts, when the ASM count rate was in excess of 20 c s^{-1} , and for all observations when the ASM count rate was below this level, but not during quiescence. Galloway et al. (2006) determined the fluence of 31 of the type I X-ray bursts observed with the PCA. We find the persistent fluence between bursts by multiplying the average ASM flux during the PCA observations by the burst recurrence time. For the latter we take the ratio of the total PCA exposure time and the number of observed bursts during either the outbursts or the low-flux state. During the outbursts the PCA observed only one burst. Therefore, from the PCA data we only have a lower limit to the burst recurrence time in the outbursts, from which we find the lower limit $\alpha \geq 745 \pm 9$. The PCA observations when the ASM flux was less than 20 c s^{-1} yield an average value of $\alpha = 51.5 \pm 0.2$.

3.4 SUPERBURST ANALYSIS

3.4.1 *Light curve*

In Fig. 3.4 we show the ASM light curve of 4U 1608-522 for the outburst in which the superburst takes place. The onset of the superburst is not observed by the ASM, as it falls in a 1.5 hour data gap. Thirty-three minutes before the start of the superburst observation by the ASM, the light curves of the WXM and FREGATE onboard HETE-2 exhibit a fast rise of 3.6 s followed by a slow decay (Fig. 3.5). Since the event took place at the end of the observation, only one minute of the flare is recorded before the instruments are switched off. Nevertheless, the light curve suggests that the decay is much longer than for a normal type I burst. The WXM detector image of the flare is consistent with the position of 4U 1608-522 if the spacecraft's attitude changed by 0.6° since the middle of the orbit. A variation of the attitude of this size is not uncommon at the end of an orbit. The FREGATE has no positional information, but 4U 1608-522 was in the field of view at that time. From both instruments spectral information is available in four energy bands. Due to the low number of observed photons per energy band, this information is of limited use for the WXM. For the FREGATE, the flare is observed in the 6 to 40 keV and 6 to 80 keV bands and not in higher energy bands, which is consistent with a type

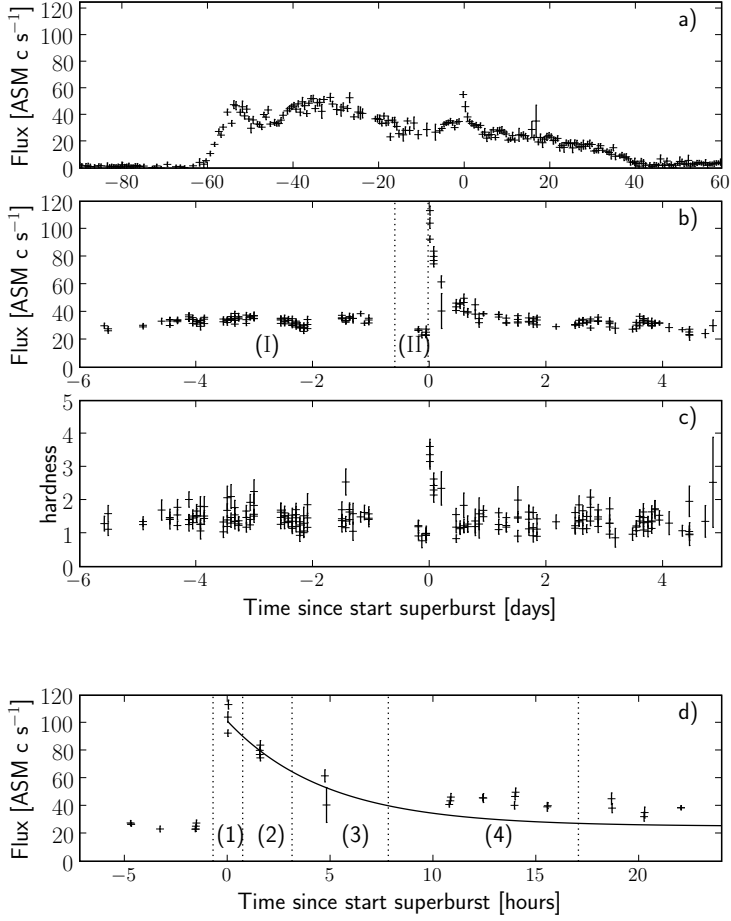


Figure 3.4: Superburst light curves where each data point represents a 90 s dwell with its 1σ uncertainty. *a)* 1.5–12 keV ASM count rate at a 0.5 day time resolution. Shown is the outburst in which the superburst takes place. *b)* Zoomed-in part of *a*. Indicated are intervals I and II of the persistent flux prior to the burst. *c)* hardness ratio for each dwell, defined as the ratio of the counts in the 5–12 keV and the 1.5–3 keV energy bands. One data point with an error in excess of 4 is excluded from the plot. *d)* Zoomed-in part of top figure on the superburst. Burst intervals 1–4 are indicated as well as the exponential decay fitted to the first 5 hours of the burst with an e-folding decay time of 4.8 hr (see Table 3.3).

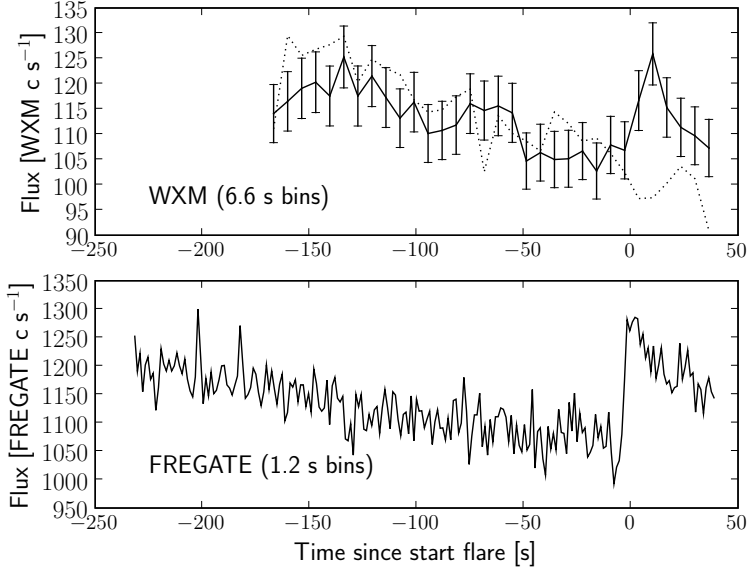


Figure 3.5: HETE-2 light curve of likely onset superburst. *Top*: WXM. The data points show the count rate with 1σ uncertainty observed by detector XB, while the dotted line indicates the count rate observed by detector XA. We employ data from the full 2–25 keV band pass at a 6.6 s time resolution. The data is from the end of an observation, when the count rate decreases as the Earth covers an increasing part of the field of view. The flare is only visible in the XB light curve. From its position on the sky, 4U 1608-522 was in the field of view of XB and not of XA. *Bottom*: FREGATE light curve from the 6–40 keV band pass at 1.2 s time resolution.

I X-ray burst (such as a superburst). Comparing this flare to a type I X-ray burst from 4U 1608-522 which was previously observed with the WXM, the flare's peak height is approximately 80% of that of the burst. Therefore, the peak flux of the flare is at most 80% of the Eddington limit. As the time of occurrence, the source position and the peak flux are consistent with the superburst from 4U 1608-522, we regard this as a likely observation of the start of this superburst.

No precursor burst can be discerned. However, the presence of such a burst cannot be ruled out. If a potentially present precursor is similar to the type I bursts observed during outbursts, it would have a short e-folding decay time of a few seconds and a peak flux of around 60% of the Eddington limit. Before the superburst onset the statistical quality of the FREGATE data is such that we can exclude at a 3σ confidence level a precursor burst with a decay time of several seconds and a net peak flux of $\sim 10\%$ of the Eddington limit or higher. However, the precursors observed from other hydrogen-accreting superbursters all took place at the superburst onset (Kuulkers et al. 2002b; Strohmayer & Markwardt 2002; in 't Zand et al. 2003). If the precursor and superburst light curves are superimposed, the presence of a precursor cannot be excluded from the data. Also, during the precursor burst the peak temperature might be lower than for the superburst, which would result in a lower observed flux in the FREGATE band. The WXM is sensitive down to lower energies, but the relative uncertainty in each data point is larger due to a smaller effective area, which may prevent us from detecting a precursor.

After the superburst took place, the first normal type I X-ray burst was observed with IBIS/ISGRI after 99.8 days. Since there are frequent data gaps, whose durations are long with respect to the duration of an X-ray burst, 99.8 days is an upper limit to the burst quenching time.

In the 4.6 hours preceding the superburst (interval II, see Fig. 3.4b) the persistent flux is at a level of 25.3 cs^{-1} , while in the 7 days prior to that (interval I) it was 32.9 cs^{-1} . The hardness ratio (Fig. 3.4c) indicates that the spectrum is harder in interval I. Approximately one day after the superburst peak, the count rate returns to the level of interval I. Only after 4.5 days does the count rate return to the level of interval II. This suggests that the superburst starts during a slight dip in the persistent flux. This makes it difficult to accurately separate the persistent emission from the burst emission during the decay. Therefore, we report results using both interval I and II.

The decay of superbursts is typically well-fit by an exponential. We fit the decay of the superburst with an exponential in all three channels separately as well as in the combined 1.5–12 keV energy band (see Table 3.3 and Fig. 3.4d). In this fit we restrict ourselves to the first

5 hours of the decay, to avoid the tail where an assessment of the persistent emission is difficult.

Not only is the count rate in interval II lower than in I. Also, the hardness ratio indicates that the spectrum is softer in interval II (see Fig. 3.4c).

3.4.2 Spectral analysis, energetics and layer thickness

We fit the persistent emission ASM spectra from both interval I and II simultaneously with an absorbed power law, coupling the N_{H} value for both spectra. The best fit values as well as the 1.5–12 keV flux in each interval are provided in Table 3.3.

We divide the superburst in four time intervals, as indicated in Fig. 3.4d, from the part of the burst where most data points lie at $> 3\sigma$ above the persistent flux from interval II (when using interval I, we restrict ourselves to the first three burst intervals). These intervals contain in total 19 measurements. Note that some of these start at the same time, but are from different SSCs. A systematic error of 3%, derived from the scatter in the Crab intensity (Levine et al. 1996), is included in the uncertainties of the data points. Levine et al. (1996) note that in many cases this is an underestimate of the systematic uncertainties. For each interval we extract a spectrum. We obtain the net-superburst spectrum by subtracting the persistent spectrum based on either interval I or II from the observed spectrum (see Kuulkers et al. 2002a for a discussion on decoupling persistent and burst emission for normal type I bursts). This net spectrum is fit with an absorbed black body.

During the spectral analysis we fix the hydrogen absorption column density. From BeppoSAX broad-band observations during outburst we find a hydrogen absorption column density of $N_{\text{H}} = 0.89 \cdot 10^{22} \text{ cm}^{-2}$ (see Sect. 3.3.2). However, here we use the value of $N_{\text{H}} = 0.61 \cdot 10^{22} \text{ cm}^{-2}$ which we obtained from the persistent emission in interval II, since we perform the superburst spectral analysis using similar ASM data and the same response matrix.

In the spectral analysis, our best fit has a reduced χ^2_{red} value of 3.5. We increased the uncertainties in the data points such that we obtained a fit with $\chi^2 = 1$. Using this fit we determined the uncertainties in the fitted parameters using $\Delta\chi^2 = 1$. Increasing the uncertainties to satisfy the ‘goodness of fit’ condition χ^2_{red} was also required when we analyzed the Crab spectrum in Sect. 3.2.2. In this procedure the best fit values of the model parameters deviate from the previous best fit values by at most 1.37σ . We fit the four intervals simultaneously, keeping the value of the black body normalization the same for all

Table 3.3: Superburst properties using persistent interval I and II with 1σ uncertainties for the last digits between parentheses.

Exponential decay times ^a				
Persistent:	I	II		
Band (keV)	τ_{exp} (hr)	χ^2_{red} /d.o.f.	τ_{exp} (hr)	χ^2_{red} /d.o.f.
1.5–12	4.1 ^{+0.6} _{−0.5}	6.2/7	4.8 ^{+0.5} _{−0.4}	6.5/7
1.5–3	12.2 ^{+6.9} _{−6.9}	1.6/6	13.2 ^{+6.2} _{−6.2}	1.6/6
3–5	7.8 ^{+3.3} _{−1.7}	1.4/7	7.8 ^{+2.3} _{−1.4}	1.5/7
5–12	3.3 ^{+0.5} _{−0.4}	2.7/7	3.9 ^{+0.4} _{−0.3}	3.2/7
Bolometric	3.0 ^{+0.4} _{−0.3}	4.3/7	3.6 ^{+0.3} _{−0.3}	5.7/7
Persistent emission prior to flare (N_{H} coupled) ^b				
Interval ^c	I	II		
N_{H}	6.1(4) · 10 ²¹ cm ^{−2}			
Γ	1.75(3)	2.06(7)		
N_{powerlaw}	2.8(2)	3.3(4)	photons keV ^{−1} cm ^{−2} s ^{−1}	
χ^2 /d.o.f.	1.7/1			
Flux ^d	1.3(3)	1.0(3)	10 ^{−8} erg s ^{−1} cm ^{−2}	
Superburst spectral analysis (N_{bb} coupled) ^e ; persistent interval I				
Interval ^c	1	2	3	
kT (keV)	2.14(14)	1.90(12)	1.60(8)	
N_{bb}			1.4(3) · 10 ²	
χ^2_{red} /d.o.f.			3.6/5	
Flux ^f	3.18(6)	1.96(4)	1.00(3)	
Superburst spectral analysis (N_{bb} coupled) ^e ; persistent interval II				
Interval ^c	1	2	3	4
kT (keV)	2.13(12)	1.89(9)	1.67(8)	1.38(7)
N_{bb}			1.7(3) · 10 ²	
χ^2_{red} /d.o.f.			3.5/7	
Flux ^f	3.81(2)	2.37(2)	1.438(11)	0.68(6)
Peak flux and burst fluence; persistent interval I				
Burst start:	ASM	HETE-2	Maximum	
Flux _{peak} ^f	2.90(14)	3.5(3)	4.8(6)	
Fluence ^g	3.1(4)	3.8(6)	5.2(1.0)	
y_{12} ^h	1.5	1.7	2.1	
E_{17} ⁱ	1.4	1.6	1.9	
Peak flux and burst fluence; persistent interval II				
Burst start:	ASM	HETE-2	Maximum	
Flux _{peak} ^f	3.88(11)	4.5(2)	6.0(5)	
Fluence ^g	5.0(4)	5.9(5)	7.6(1.1)	
y_{12} ^h	3.0	3.3	4.1	
E_{17} ⁱ	1.5	1.6	1.9	

Continued on next page.

Table 3.3 continued.

^aIn the 1.5–3 keV band we find the decay to be consistent with a horizontal line, due to the large uncertainty of the data points in the tail of our fit interval.

^bAbsorbed power law model ($N_{\text{powerlaw}} E^{-\Gamma}$) parameters: N_{H} the interstellar column density, Γ the photon index and N_{powerlaw} the normalization defined as photons $\text{keV}^{-1} \text{cm}^{-2} \text{s}^{-1}$ at 1 keV.

^cSee Fig. 3.4b.

^dUnabsorbed flux in 1.5–12 keV energy range ($10^{-8} \text{erg s}^{-1} \text{cm}^{-2}$).

^eBlack body model parameters: temperature kT and normalization $N_{\text{bb}} \equiv R^2/d^2$, with R the source radius in km and d the source distance in 10 kpc.

^fUnabsorbed bolometric flux ($10^{-8} \text{erg s}^{-1} \text{cm}^{-2}$).

^gUnabsorbed bolometric fluence ($10^{-4} \text{erg cm}^{-2}$).

^hColumn depth (10^{12}g cm^{-2}).

ⁱEnergy release per unit mass ($10^{17} \text{erg g}^{-1}$).

spectra. Since the normalization parameter depends on the emission region size of the black body, this implies that the size is assumed not to change during the superburst decay. This is a valid approach, as we will see that the peak flux of the superburst is below the Eddington flux at which photospheric expansion is expected. Fits where we did not use this coupling did not indicate a significant change in radius from one interval to the next. We provide the best fit values of the model parameters in Table 3.3. Assuming isotropic radiation and using the distance of 3.2 ± 0.3 kpc as well as the best fit value for the black body normalization, we find an emission region size equivalent to a sphere with a radius of $R = 4.2 \pm 0.5$ km, which is consistent with the black body radii both Murakami et al. (1980b) and Galloway et al. (2006) found for normal type I X-ray bursts.

To investigate the influence of the choice of N_{H} on the fit results, we repeated the spectral analysis using $N_{\text{H}} = 8.91 \cdot 10^{21} \text{cm}^{-2}$ (see Table 3.1). The difference in best fit values of the model parameters to those in the previous analysis never exceeds 1σ . The derived flux differs by at most 3%.

Using the average count rate and the flux we obtained for each burst interval, we convert the count rate of each data point to flux. We fit an exponential function to the first 5 hours of the resulting curve and determine the peak flux at the start of this interval. We find a peak flux of $22 \pm 3\%$ ($29 \pm 3\%$) of the Eddington flux using the persistent level from interval I (II). Integrating this exponential gives us the burst fluence, which at a distance of 3.2 ± 0.3 kpc corresponds to a burst energy of $(3.8 \pm 0.9)10^{41} \text{erg}$ ($(6.1 \pm 1.2)10^{41} \text{erg}$). By extrapolating the

Table 3.4: Characteristics of the 4U 1608-522 superburst compared to 13 other superbursts (from Kuulkers 2004 and in 't Zand et al. 2004a). τ_{exp} from fit to count rates converted to unabsorbed bolometric flux.

	4U 1608-522	Other superbursts
Duration (hr)	5–22	2–15
Precursor	No	Always when data available
$\tau_{\text{exp}}(\text{hr})^a$	~ 4.5	0.7–6
$kT_{\text{peak}}(\text{keV})$	2.1 ± 0.1	1.8–3
$L_{\text{peak}}(10^{38} \text{ erg s}^{-1})$	0.4–0.7	0.4–3.4
$L_{\text{pers}}(L_{\text{Edd}})$	0.11–0.15	0.1–0.25 ^b
$\langle L_{\text{pers}} \rangle (L_{\text{Edd}})$	0.03	0.11–0.43 ^c
$E_b(10^{42} \text{ erg})$	0.4–0.9	0.3–1.4
$\tau \equiv E_b/L_{\text{peak}}(\text{hr})$	1.0–1.3	1.1–6.9
$\gamma \equiv L_{\text{pers}}/L_{\text{peak}}$	0.2–0.5	0.1–0.7
$t_{\text{no bursts}}(\text{d})$	< 99.8	> 7.5
Donor	H/He	He and H/He

^a Exponential decay time in 1.5–12 keV band for 4U 1608-522 and in similar energy bands for other superbursters.

^b Persistent luminosity at the time of the superburst, excluding the candidate ultracompact source 4U 0614+091 and the Z-source GX 17+2 which have a luminosity close to, respectively, 1% (Kuulkers 2005; in 't Zand et al. 2007) and 100% (in 't Zand et al. 2004a) of the Eddington luminosity.

^c Average persistent luminosity from all ASM observations, again excluding 4U 0614+091 and GX 17+2.

exponential to the start of the flare observed by HETE-2, a peak flux of $27 \pm 4\%$ ($34 \pm 4\%$) of the Eddington flux and a burst fluence of $(4.7 \pm 0.8)10^{41} \text{ erg}$ ($(7.2 \pm 0.9)10^{41} \text{ erg}$) are obtained. Extrapolating to the start of the ASM data gap preceding the observed part of the burst, we find an upper limit to the peak flux and burst fluence: respectively $36 \pm 6\%$ ($45 \pm 4\%$) of the Eddington flux and $(6 \pm 2)10^{41} \text{ erg}$ ($(9 \pm 2)10^{41} \text{ erg}$) (see Table 3.3).

Cumming & Macbeth (2004) present multizone numerical models for the cooling of the neutron star surface layers during the decay of a superburst as well as analytic fits to these models. The models depend on the ignition column depth $y \equiv y_{12}10^{12} \text{ g cm}^{-2}$ and the energy release per gram $E \equiv E_{17}10^{17} \text{ erg g}^{-1}$. Cumming et al. (2006) fit these models to the light curves of six superbursts. We perform the same fit to the light curve of the superburst from 4U 1608-522 using the persis-

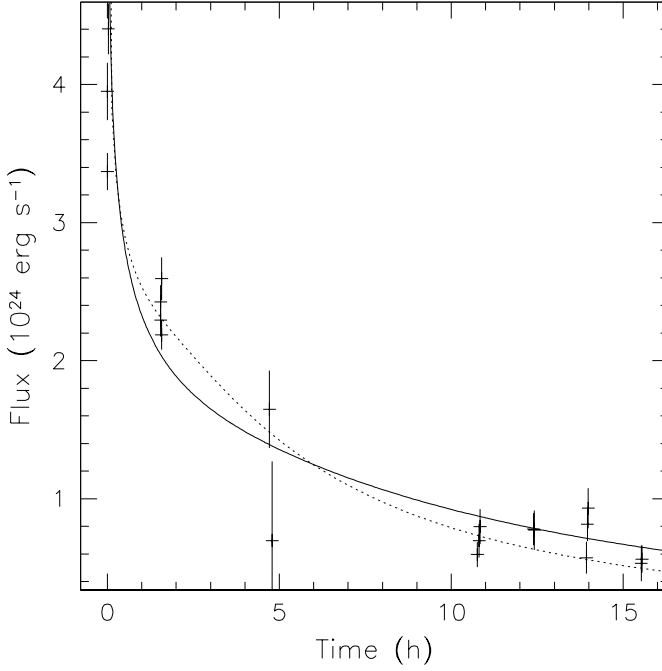


Figure 3.6: Fit of cooling models to superburst decay. The data points are ASM count rates converted to flux for each ASM measurement (see Sect. 3.4.2) with 1σ uncertainties. The persistent level from interval II is used (see Fig. 3.4b). The solid and dotted line represent fits with, respectively, the numerical and analytic cooling models from Cumming & Macbeth (2004).

tent level from both interval I and II (Fig. 3.6). We find, respectively, $y_{12} = 1.5$, $E_{17} = 1.4$ and $y_{12} = 3.0$, $E_{17} = 1.5$. To estimate the values of y_{12} and E_{17} in case the superburst started at either the start of the flare observed with HETE-2 or at the start of the data gap in the ASM light curve, we use the scaling laws found by Cumming et al. (2006). Thus we obtain the ranges $y_{12} = 1.5 - 2.1$, $E_{17} = 1.4 - 1.9$ and $y_{12} = 3.0 - 4.1$, $E_{17} = 1.5 - 1.9$, using respectively the persistent level from interval I and II (see Table 3.3).

3.5 DISCUSSION

The first detection of a superburst from a classical LMXB transient poses significant challenges to superburst theory and underlines short-

comings thereof that were already realized earlier. This shows the need for additional ingredients in the models. While the superburst characteristics of 4U 1608-522 are similar to those from other superbursters (see Table 3.4), the accretion rate on a time scale of ten years is a factor of 3 smaller than observed for the slowest accretor among all other superbursting sources.

In the following subsections we will see that there are two challenges: the destruction of carbon by the ever-present hydrogen/helium flashes is apparently not as important as theory predicts and the predicted crust temperatures fall short by a factor of 2 of the value required for the ignition of unstable carbon burning. Additionally, we make a few remarks on the mHz QPO observed in 4U 1608-522.

3.5.1 *Recurrence time*

From fits of cooling models to the superburst light curve we find that the superbursting layer had at ignition a column depth of $y_{12} = 1.5 - 4.1$ and an energy release per unit mass of $E_{17} = 1.5 - 1.9$, which implies a total energy release of $(2.6 - 9.8)10^{42}$ erg. From the X-ray flux we derived an energy release of $(0.4 - 0.9)10^{42}$ erg, which is only 5 – 45% of the total inferred from the cooling models (after correction for the gravitational redshift with a typical value of $1 + z = 1.3$). The rest of the energy is either released as neutrinos or is conducted to greater depths and radiated away on a longer timescale. Fig. 3.7 shows the column depth that is observed to be accumulated since the start of the ASM observations. At the moment of the superburst a column of $y_{12} = 0.55$ ($y_{12} = 0.27$ taking into account only the stable burning in the high state) had been accreted over a period of 9.3 years. Note that this is derived under the assumption that the X-ray flux is a good measure for the mass accretion rate, which may not be the case (see discussion in Sect. 3.3.2). In fact, we assume that stable burning occurs when the ASM flux is in excess of 20 c s^{-1} , which introduces an uncertainty of several tens of percents in the column depth. With an average accretion rate of $\dot{M} = (1.8 \pm 0.2)10^{-2} \dot{M}_{\text{Edd}}$ the required column depth is accreted over a period of 26 to 72 years. If carbon is only produced from matter accreted during stable burning in the high state, the recurrence time is twice as long. In both cases it is much longer than the 57.6 day duration of the 2005 outburst before the superburst occurred. This implies that the carbon fuel has been produced during multiple outbursts.

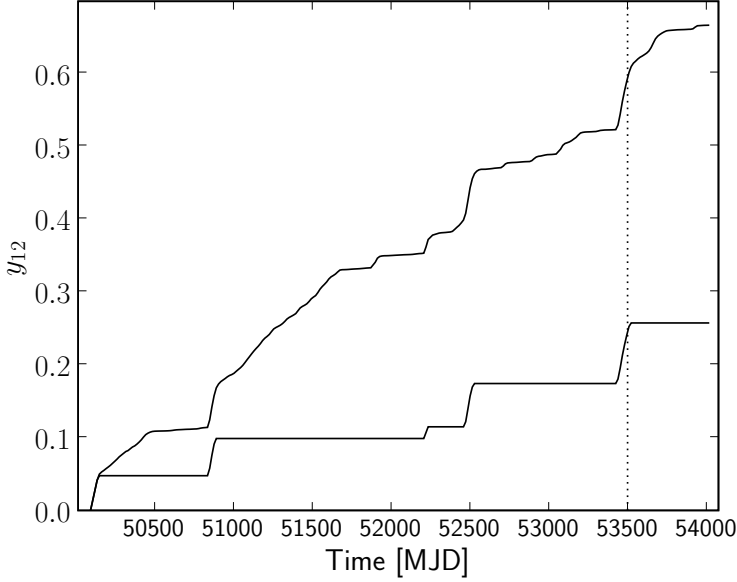


Figure 3.7: Accreted column depth $y_{12} \equiv y/(10^{12} \text{g cm}^{-2})$ over time. Assuming a neutron star of $1.4 M_{\odot}$ mass and 10 km radius at a distance of 3.2 kpc, we show the cumulative column depth that is accreted since the start of RXTE ASM observations as inferred from the X-ray flux at 14 day time resolution (c.f. Fig. 3.1). The lower curve takes into account only matter that is accreted when 4U 1608-522 was in the high state when the ASM count rate exceeded 20 c s^{-1} , while the upper curve includes the low state as well. The dotted line indicates the moment the superburst was observed.

3.5.2 *Producing and preserving carbon*

Schatz et al. (2003) found from nucleosynthesis calculations that carbon is produced most efficiently through the stable nuclear burning of hydrogen and helium. Unstable burning during type I X-ray bursts results in significantly less carbon ($\lesssim 1\%$ by mass; Woosley et al. 2004), but produces heavier ashes. Cumming & Bildsten (2001) proposed that these heavy ashes are important because they set the opacity and therefore temperature of the superbursting layer, although Brown (2000) later showed that this effect is much smaller than initially estimated once the temperature profile of the entire crust was taken into account. Therefore, it is interesting to ask whether both burning regimes are necessary for producing the fuel for superbursts. Certainly, all known superbursters exhibit both type I X-ray bursts and a high α value, which are indications for both unstable and stable burning, respectively.

The stable burning of helium takes place at accretion rates \dot{M} in excess of 10% of Eddington. Therefore, we expect that in 4U 1608-522 carbon is created during the outbursts. This carbon could be destroyed by type I X-ray bursts, which are observed during all flux states. For carbon to survive the bursts, it has to reside in a layer which is depleted of hydrogen. Woosley et al. (2004) find this to be the case at the bottom of a bursting layer. The different composition of the ashes of unstable hydrogen/helium burning as opposed to stable hydrogen/helium burning (Woosley et al. 2004; Schatz et al. 2003) will likely mix rapidly. If a period of stable burning was followed by unstable burning, the heavier ashes of the latter would rapidly undergo a Rayleigh-Taylor instability and mix with the lighter ashes below.

An important question is whether the carbon is able to burn stably during the low state. Cumming & Bildsten (2001) argued that carbon would burn stably at low accretion rates, and suggested that this may explain why superburst sources have accretion rates of ≈ 0.1 Eddington and up. This question is crucial to understand for 4U 1608-522, since the accretion rate is low during quiescence and the low persistent state. Further modelling of the production and destruction of carbon during the cycle of transient outbursts is needed.

A complication here is that at the low accretion rates that occur during quiescence and in the low persistent state in 4U 1608-522, the accretion may be slow enough that the carbon and heavy elements in the ashes of normal type I bursts gravitationally separate, with the carbon floating upwards relative to the heavy elements. To estimate the relative drift velocity of a carbon nucleus in the heavy element ocean, we follow the work of Bildsten & Hall (2001), who estimated the rate of sedimentation of ^{22}Ne in the interiors of CO white dwarfs. They

start with the self-diffusion coefficient for a one component plasma, $D \approx 3\omega_p a^2 \Gamma^{-4/3}$ (Hansen et al. 1975), where ω_p is the ion plasma frequency, a is the inter-ion separation, and Γ is the standard parameter that measures the strength of the Coulomb interactions between ions. A single carbon nucleus in a background of ^{56}Fe feels an upward force of $12m_p g/13$, giving a drift velocity $v = 54m_p g/169e\Gamma^{1/3}(4\pi\rho)^{1/2}$ (compare Bildsten & Hall 2001 eq. [3]). Writing the time to cross a pressure scale height at this drift velocity as $t_s = H/v = P/\rho g v$, and assuming that the pressure is provided by degenerate relativistic electrons (a good approximation at these depths), we find

$$t_s = 7.2 \text{ years } y_{12}^{13/24} \left(\frac{T_8}{6} \right)^{-1/3} \left(\frac{g_{14}}{2.45} \right)^{-31/24},$$

where we assume that the heavy element is ^{56}Fe (the scaling is $t_s \propto Z^{37/18}/A$). This timescale is equal to the accretion timescale t_{accr} for $\dot{m} \approx 0.05 \dot{m}_{\text{Edd}}$. The sedimentation timescale t_s is comparable to the timescale on which we infer the carbon fuel is accumulated, so that the physics of the relative separation of the carbon and heavy elements should be considered further.

3.5.3 The crust temperature and carbon ignition

Although the accretion rate of 4U 1608-522 reaches $\dot{M} \lesssim 0.23\dot{M}_{\text{Edd}}$ during the peak of the outburst, the high accretion rate only lasts a short ($\lesssim 100$ d) time, so that the crust does not reach a thermal steady-state. The temperature of the deep crust can be inferred by observations of the quiescent luminosity (Rutledge et al. 1999). Hence this source provides a test of the strength and location of heat sources in the crust. The question is whether the crust can reach temperatures sufficiently hot to initiate thermally unstable ^{12}C fusion in the short time available during the outburst. To check this, we constructed a time-dependent model based on recent calculations of the heating from electron capture reactions in the crust (Gupta et al. 2007). We set the mass number to $A = 40$, which yields a large heat release (0.40 MeV per accreted nucleon) in the outer crust. For the inner crust, we use the model of Haensel & Zdunik (1990). We integrated the thermal diffusion equation using a standard method-of-lines formalism. The microphysics is identical to that in Gupta et al. (2007). The total heat released in the crust during outburst is 1.8 MeV u^{-1} .

As an initial condition, we computed the temperature for steady accretion at the time-averaged mass accretion rate $\langle \dot{M} \rangle = 6.5 \cdot 10^{15} \text{ g s}^{-1}$. We then ran through a series of 60 outburst/quiescent cycles, to en-

sure that the crust had reached a limit cycle. During outburst we set $\dot{M} = 1.3 \cdot 10^{17} \text{ g s}^{-1}$, with a duration of 80 d; the quiescent interval was set to 4.16 yr. During quiescence we used a relation between the temperature at a column $y = 10^9 \text{ g cm}^{-2}$ and the surface luminosity appropriate for an accreted envelope (Brown et al. 2002). The quiescent luminosity reached a minimum of $L_q = 6.1 \cdot 10^{33} \text{ erg s}^{-1}$, in reasonable agreement with the value derived by Rutledge et al. (2000). Figure 3.8 shows the change in temperature, as a function of column, during the outburst. At the start of the outburst (*solid line*), we set the temperature at a column $y = 10^9 \text{ g cm}^{-2}$ to $5 \cdot 10^8 \text{ K}$. This is a reasonable upper limit on the temperature set by steady-state H/He burning. After 80 d, the temperature in the outer crust has risen substantially (*dotted line*), but is still much cooler than needed to explain the fitted ignition column and temperature (*shaded box*).

We conclude that heating in the crust from electron captures, neutron emissions, and pycnonuclear reactions, is insufficient to raise the crust temperature during the outburst enough for ^{12}C to ignite at the inferred column.

In the other superburst sources, which are either persistent accretors, or transients with long duration outbursts (e.g. KS 1731-260), the crust reaches a thermal steady state. Even in these sources, theoretical models have difficulty explaining the inferred superburst ignition columns of $\sim 10^{12} \text{ g cm}^{-2}$ (Brown 2004; Cooper & Narayan 2005; Cumming et al. 2006; Gupta et al. 2007). The properties of the neutron star crust and core that affect the thermal profile such as neutrino emissivity and crust conductivity must all be chosen to maximize the crust temperature in order to achieve the observed ignition depths. In fact, Cumming et al. (2006) showed that it was impossible to reproduce the observations if neutrino cooling due to Cooper pair formation of superfluid neutrons in the crust (e.g. Yakovlev et al. 1999) was included, because this efficient neutrino emission mechanism led to an upper limit on the crust temperature at the ignition depth of $\approx 4 \times 10^8 \text{ K}$, less than the temperature of $\approx 6 \times 10^8 \text{ K}$ required for carbon ignition. Recent work by Leinson & Pérez (2006) has shown that the neutrino emission due to this mechanism has been overestimated in previous calculations, and that this mechanism is in fact not the dominant source of neutrino emissivity.

As we have shown, the short duration of the transient outbursts in 4U 1608-522 means that the crust is heated to much lower temperatures than those corresponding to thermal equilibrium. Therefore the observation of a superburst from 4U 1608-522 is deeply puzzling and presents a significant challenge to current superburst models.

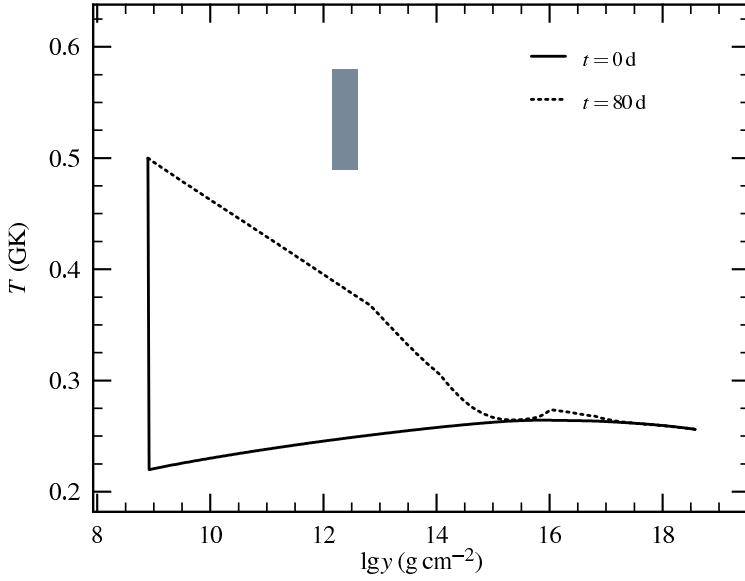


Figure 3.8: Temperature evolution in the crust of 4U 1608-522 during the outburst. At the beginning of the outburst (*solid line*) we set the temperature at a column $y = 10^9 \text{ g cm}^{-2}$ to $5 \cdot 10^8 \text{ K}$. After 80 days, the temperature in the outer crust has risen (*dotted line*), but is still well below the temperature for which a one-zone stability analysis would predict a superburst with a depth inferred from fits to the cooling (*shaded box*).

3.5.4 *Bursting behavior and mHz QPOs*

The normal type I X-ray bursting behavior looks similar to what is seen in persistent bursting sources with strongly variable persistent fluxes, most notably 4U 1820-303 (Chou & Grindlay 2001), GX 3+1 (den Hartog et al. 2003), 4U 1705-44 and KS 1731-260 (Cornelisse et al. 2003). In those cases X-ray bursts become far less frequent or even absent during high flux states. Also in the case of 4U 1608-522 the bursting behavior is seen to differ between the low and high flux state. Murakami et al. (1980b) report that in the high flux state bursts have a shorter duration and a higher α value than the bursts in the low flux state, while the burst rate is not significantly different. The bursts observed with the RXTE PCA and the BeppoSAX WFCs exhibit this behavior as well. This would be consistent with hydrogen and helium burning becoming predominantly stable at higher mass accretion rates (van Paradijs et al. 1988).

Revnivtsev et al. (2001) examined EXOSAT and RXTE PCA data of 4U 1608-522 and discovered low frequency quasi-periodic oscillations (mHz QPOs). They observed no type I X-ray bursts when the persistent emission was higher than when the QPOs were detected, which supported the hypothesis that mHz QPOs occur at the transition of unstable to stable burning, such that at higher accretion rates the bursting behavior ceases (see also Heger et al. 2007). Interestingly, the PCA, WFCs and IBIS/ISGRI have observed a total of four X-ray bursts when the persistent flux was up to a factor of two higher than when mHz QPOs were seen (see Fig. 3.3). Although this disagrees with the prediction of the marginally stable burning model of Heger et al. (2007), the hypothesis could still be valid if, as discussed by Heger et al. (2007), the conditions for nuclear burning vary substantially across the neutron star surface, such that on one part of the surface unstable burning gives rise to type I bursts while on another part mHz QPOs occur. The scenario that ignition conditions might vary across the surface of the star for rapidly rotating neutron stars has been discussed by Cooper & Narayan (2007) (see also Spitkovsky et al. 2002), although the predicted range for the global accretion rate where both stable and unstable burning take place at different latitudes is a factor of 3 higher than where mHz QPOs are observed from 4U 1608-522.

3.6 SUMMARY AND CONCLUSIONS

For the first time a superburst has been observed from a transiently accreting neutron star in a low-mass X-ray binary where the duration of

the accretion outbursts is short with respect to the expected superburst recurrence time. 4U 1608-522 exhibited a superburst 55 days after the onset of an accretion outburst. We analyzed the superburst as well as the long term accretion and bursting behavior of 4U 1608-522. We found the properties of the superburst to be comparable to those of the long superbursts observed from 4U 1254-690 and KS 1731-260. Fits of cooling models to the superburst light curve indicate that the superburst ignited when a column of $y = (1.5 - 4.1)10^{12} \text{ g cm}^{-2}$ had been accreted. From the average X-ray flux that the RXTE ASM observed from 4U 1608-522 over the past 11 years, we derive that this column was accreted over a period of 26 to 72 years.

The difficulties that superburst theory has in explaining the ignition column depths derived for other superbursters, are underlined by the observation of the superburst in 4U 1608-522. The transient nature of the accretion poses challenges for superburst models. The average accretion rate over the past 11 years was much lower than for the other superbursters, with the possible exception of 4U 0614+091 (Kuulkers 2005). At the derived column depth, current superburst theory predicts that during the timespan of the outbursts the crust temperature does not rise to the value required for superburst ignition. Furthermore, the carbon that fuels the superburst is expected to be produced only during the outbursts, while the stable nuclear burning of ^{12}C as well as the frequent type I X-ray bursts lower the carbon abundance. The detection of the superburst implies that a significant amount of carbon survives the long periods outside the outbursts. The balance between the creation and destruction processes is influenced by mixing and sedimentation in the neutron star envelope. The effect of these requires further study before predictions about the produced amount of superburst fuel can be made.

DISCOVERY OF X-RAY BURST TRIPLETS IN EXO 0748-676

L. Boirin, L. Keek, M. Méndez, A. Cumming, J. J. M. in 't Zand,
J. Cottam, F. Paerels and W. H. G. Lewin

Astronomy & Astrophysics 2007, 465, 559–573

ABSTRACT Type-I X-ray bursts are thermonuclear flashes that take place on the surface of accreting neutron stars. The wait time between consecutive bursts is set by the time required to accumulate the fuel needed to trigger a new burst; this is at least one hour. Sometimes secondary bursts are observed, approximately 10 min after the main burst. These short wait-time bursts are not yet understood. We observed the low-mass X-ray binary and X-ray burster EXO 0748-676 with XMM-Newton for 158 h, during 7 uninterrupted observations lasting up to 30 h each. We detect 76 X-ray bursts. Most remarkably, 15 of these bursts occur in burst triplets, with wait times of 12 min between the three components of the triplet, T₁, T₂, and T₃. We also detect 14 doublets with similar wait times between the two components of the doublet, D₁ and D₂. We characterize this behavior to try and obtain a better understanding of bursts with short wait times. We measure the burst peak flux, fluence, wait time and time profile, and study correlations between these parameters and with the persistent flux representing the mass accretion rate. (i) For all bursts with a long wait time, the fluence is tightly correlated with the wait time, whereas burst with short wait times generally have higher fluences than expected from this relationship; (ii) Wait times tend to be longer after doublets and triplets; (iii) The time profile of single bursts, S₁, and of the first burst in a double or triple burst, D₁ and T₁, always contains a slow component which is generally absent in the D₂, T₂ and T₃ bursts; (iv) The peak flux is highest for S₁, D₁ and T₁ bursts, but this is still a factor of 7 lower than the highest peak flux ever seen for a burst in this system; (v) The persistent flux, representing the mass accretion rate onto the neutron star, is about 1% of Eddington, which is among the lowest value so far measured for this system. The amount of energy per gram of accreted mass liberated during bursts is consistent with a fuel mixture of hydrogen-rich material. The characteristics of the bursts indicate that possibly all bursts in this system are hydrogen-ignited,

in contrast with most other frequent X-ray bursters in which bursts are helium-ignited, but consistent with the low mass accretion rate in EXO 0748-676. Possibly the hydrogen ignition is the determining factor for the occurrence of short wait-time bursts. For example the 12 min wait time may be associated with a nuclear beta decay timescale.

4.1 INTRODUCTION

Type I X-ray bursts are due to unstable burning of hydrogen and/or helium on the surface on an accreting neutron star (for a review see Lewin et al., 1993). Fuel accumulates for hours to days, and then ignites as soon as the pressure and temperature conditions for thermonuclear reactions are reached. Since the nuclear reaction rates depend strongly on the temperature, the ignition leads to a runaway process, and the fuel burns explosively in a rapid ~ 10 – 100 s burst releasing typically 10^{38-39} ergs. Two bursts from a given source are usually separated by a few hours. However, doublets with burst intervals as short as ~ 10 minutes have been observed from several sources including EXO 0748-676 (Gottwald et al., 1986), GS 0836-429 (Aoki et al., 1992), 4U 1608-522 (Murakami et al., 1980a), 4U 1636-536 (Ohashi et al., 1982; Pedersen et al., 1982), 4U 1705-440 (Langmeier et al., 1987) and XB 1745-248 (Inoue et al., 1984). A burst interval as short as 50 s has been seen in MXB 1659-29 (Wijnands et al., 2002). Lewin et al. (1976) report SAS-3 observations of *three* consecutive bursts from MXB 1743-28 with burst intervals of 18 and 4 minutes. However, these are observations of a field with several known bursters, and therefore there is a slight chance that these three bursts may not be attributed to one source.

Bursts separated by short time intervals are not well understood in the context of the classical thermonuclear flash model. Since the interval is too short to accrete sufficient material to fuel a thermonuclear burst, secondary bursts are thought to be due to burning of residual fuel that did not burn during the primary burst. This involves incomplete nuclear burning, fuel storage and a mixing mechanism with the freshly accreted material (Fujimoto et al., 1987).

EXO 0748-676 is one of the sources where the double burst phenomenon was best studied thanks to several EXOSAT observations carried out at different persistent fluxes of the system. In 1985, 26 bursts were detected, including four doublets with a burst separation of the order of 10–20 min (Gottwald et al., 1986). The doublets only occurred when the persistent flux was low. As the persistent flux increased, the doublet phenomenon stopped, the wait time of the single

bursts increased, and their shape changed from a ‘slow’ (long tail) to a ‘fast’ profile sometimes showing photospheric expansion. Gottwald et al. (1986) hypothesized that these variations could be caused by the flashes changing from hydrogen-triggered hydrogen-helium flashes at low accretion rates to helium-dominated flashes at high accretion rates, a scenario previously theoretically studied by Fujimoto et al. (1981) (see also Ayasli & Joss, 1982) who outlined three ways to trigger shell flashes depending on the accretion rate. Gottwald et al. (1986) speculated that double bursts could be a feature of hydrogen-triggered hydrogen-helium flashes.

In another EXOSAT observation in 1986, 11 bursts were observed and showed a regular pattern with a long recurrence time always followed by a short one, reminiscent of the double burst phenomenon, but with longer separations, in the range 20–70 min (Gottwald et al., 1987). The wait time to a burst and the total emitted energy in that burst displayed a linear relation but with an offset energy at zero burst interval that was interpreted as incomplete consumption of fuel in the primary burst and its subsequent consumption in the secondary burst. The amount of unburned fuel was estimated to be 10–15% of the total available nuclear energy.

Cottam et al. (2002) reported redshifted spectral lines identified with O and Fe transitions during X-ray bursts from EXO 0748-676 observed with RGS on XMM-Newton, implying a gravitational redshift $z = 0.35$. Combining this redshift measurement with the peak flux of the radius expansion burst observed by Wolff et al. (2005) and the flux and color temperature observed during the cooling tail of bursts from EXOSAT and RXTE, Özel (2006) derived limits on EXO 0748-676 compact object mass and radius which ruled out several soft equations of state for the neutron star interior.

Özel (2006) further derived a lower limit to the EXO 0748-676 distance of 9.2 ± 1.0 kpc (see note 1 in Sect. 4.6). The source distance was previously estimated from bursts showing photospheric expansion to range between 6.8 and 9.1 kpc (Jonker & Nelemans, 2004) or between 5.9 ± 0.9 and 7.7 ± 0.9 kpc (Wolff et al., 2005), the smallest and largest values corresponding to hydrogen rich and poor material, respectively. In this thesis, we use the extreme values of the distance derived so far: 5 and 10 kpc.

EXO 0748-676 light curves exhibit dipping activity and eclipses every 3.8 h (e.g., Parmar et al., 1986). Dips and eclipses are due to the central X-ray source being obscured by some structure above the disk, and occulted by the companion star, respectively, at every orbital period (e.g., Frank et al., 1987). Their presence indicates that EXO 0748-676 is

viewed at an inclination of $\approx 75\text{--}83^\circ$ (Parmar et al., 1986), *i.e.* almost from the accretion disk plane.

Here, we report the discovery of *triple* bursts in EXO 0748-676. This is the first time that unambiguously and repeatedly triple bursts are detected in an accreting neutron star. We inspect EXO 0748-676 non-bursting emission to conclude that the accretion rate is likely constant throughout the analyzed set of XMM-Newton observations (Sect. 4.3). We derive the properties of the 76 bursts detected, using the 5–10 keV light curve to minimize the contamination from the dipping activity (Sect. 4.4). We perform a time-resolved spectral analysis of a sample of bursts not affected by dipping. We compare the triple bursts with the single and double bursts detected during the same XMM-Newton observations, and also with those detected during the EXOSAT observations (Sect 4.5). We discuss the burst properties in the context of the well-studied helium-triggered hydrogen-helium burning thermonuclear flash model and in the context of the poorly-studied hydrogen-triggered hydrogen(-helium?) burning flash model (Sect 4.6).

4.2 OBSERVATIONS AND DATA REDUCTION

The XMM-Newton Observatory (Jansen et al., 2001) includes three 1500 cm^2 X-ray telescopes each with a European Photon Imaging Camera (EPIC) at the focus. Two of the EPIC imaging spectrometers use MOS CCDs (Turner et al., 2001) and one uses PN CCDs (Strüder et al., 2001). Reflection Grating Spectrometers (RGS, den Herder et al., 2001) are located behind two of the telescopes.

EXO 0748-676 was observed by XMM-Newton on several occasions with different instrument configurations. In this thesis, we use the 7 observations performed between September and November 2003, during XMM-Newton revolutions 692 to 719, for a total exposure time of 158 hours (Table 4.1). We focus on the EPIC PN data (0.1–10 keV) that were all obtained in small window mode with the medium optical blocking filter applied. In this mode, only a fraction of the central CCD chip, corresponding to 63×64 pixels or $4'.3 \times 4'.4$, is read out. This allows a time resolution of 5.7 ms to be reached, and significant photon pile-up occurs only for count rates $\gtrsim 100\text{ counts s}^{-1}$.

We reduce the observations using versions 5.4.1 to 6.1.0 of the science analysis software. Only single and double events (patterns 0 to 4) are selected. The ratio of background to source persistent intensity is generally $\lesssim 1\%$ and reaches occasionally $\sim 10\%$ during some episodes of higher background level due to enhanced solar activity. We do not discard any data interval for this analysis. For the light curves and es-

Table 4.1: XMM-Newton observations of EXO 0748-676 performed between September 19 and November 12, 2003. We indicate the observation identification and revolution numbers, the EPIC PN start and exposure times, the number of X-ray bursts and bursting events observed (for singlets, doublets and triplets separately and in total), and the mean event wait time.

Obs-ID	Rev.	Start (UT)			t_{exp}	Bursts	Singlets	Doublets	Triplets	Events	Mean event wait time
		Month	Day	h:m	(h)						(h)
0160760101	692	Sept.	19	13:37	24.6	10	6	2	0	8	3.20
0160760201	693	Sept.	21	13:38	25.1	14	6	1	2	9	2.65
0160760301	694	Sept.	23	10:42	30.0	14	7	2	1	10	3.02
0160760401	695	Sept.	25	17:29	20.4	^a 9	3	^a 3	0	^a 6	3.49
0160760601	708	Oct.	21	10:02	15.2	8	3	1	1	5	2.99
0160760801	710	Oct.	25	19:19	17.3	9	3	3	0	6	2.71
0160761301	719	Nov.	12	08:24	25.2	12	5	2	1	8	3.19
Total					157.9	76	33	14	5	52	Mean 3.02

^a including a burst detected by RGS only, a few seconds before EPIC cameras were turned on.

timate of rough burst properties (peak count rates, number of counts in a burst), we extract source events from within a circle of $40''$ radius centered on the position of EXO 0748-676. For the burst spectral analysis, we extract source events from an annulus with an outer radius of $40''$ and a $9.3''$ inner radius, in order to avoid pile-up effects which become significant near the burst peaks. Such an annulus contains 63% of the events from the circular region.

4.3 NON-BURSTING EMISSION

The PN light curves of the 7 observations of EXO 0748-676 are shown in Fig. 4.16 in the appendix, in the ‘hard’ 5–10 keV (panel a) and in the ‘soft’ 0.3–5 keV energy band (panel b), while panel c shows the color (counts in the hard band divided by those in the soft band) as a function of time. In addition to X-ray bursts, EXO 0748-676 light curves exhibit eclipses every 3.8 h and dipping activity.

Dipping is associated with spectral hardening (Fig. 4.16 c), the soft light curve (Fig. 4.16 b) being substantially more affected than the hard one (Fig. 4.16 a). The dipping activity is highly irregular on timescales of days, with the soft light curve shape clearly changing from one XMM-Newton observation to another. While a dipping pattern covering a limited phase range of ~ 0.7 – 0.9 is easily recognizable in some observations (e.g. revolution 693), this is not the case in others (e.g. revolution 692) where the soft intensity and hardness display erratic variability at all orbital phases.

Díaz Trigo et al. (2006) analyzed the PN data of EXO 0748-676 during revolution 719. Excluding eclipses and bursts, they define six intensity stages, and call the highest range the ‘persistent’ level, and the lowest one the ‘Dip 5’ level. They extract one spectrum per level and fit them simultaneously with a continuum model affected by a neutral and by an ionized absorber. While the parameters of the continuum are forced to be the same for the six spectra, the parameters of the absorbers are left independent. By successfully fitting the spectra with this method, Díaz Trigo et al. (2006) demonstrate that all the intensity and spectral changes from EXO 0748-676 during revolution 719 can be simply explained by changes in the ionization level and in the amount of the absorbers that are located inside the system, while the underlying X-ray source is staying constant. Not only the ‘dipping’ spectra are affected by the local absorbers, but also the ‘persistent’ one (see Fig. 3 and Table 7 of Díaz Trigo et al., 2006). The term ‘persistent’, if understood as un-affected by local absorbers, is therefore un-appropriate in this case, EXO 0748-676 being ‘dipping’ (if understood as affected

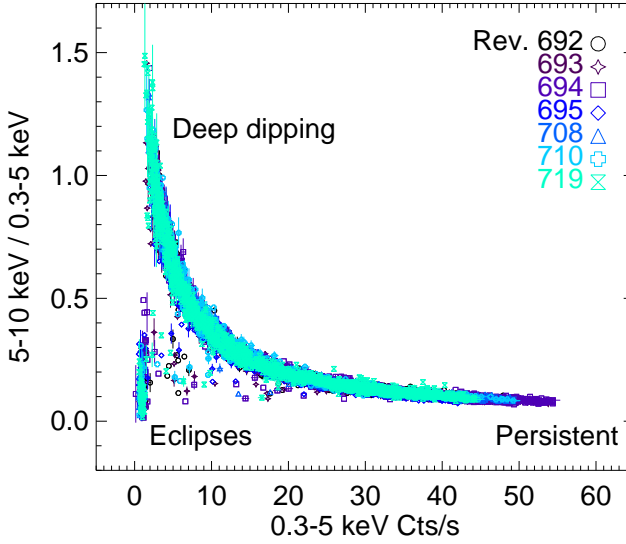


Figure 4.1: Color (counts in the 5–10 keV band divided by counts in the 0.3–5 keV band) of EXO 0748-676 non-bursting emission as a function of the soft (0.3–5 keV) intensity during the seven XMM-Newton observations whose revolution number is indicated in the right corner. Error bars are shown on one third of the points which represent 60 s each. The intensity and spectral changes during revolution 719 (bursts and eclipses excluded), and hence the boomerang track associated to that revolution, can be explained by changes in the ionization level and in the amount of absorbers in front of a constant underlying X-ray source (Díaz Trigo et al., 2006). Remarkably, the data obtained during the other revolutions (spanning several months) follow the same track. This indicates that the spectral changes during these observations can be explained by the same phenomenon and that the underlying X-ray emission is likely the same during the seven observations studied here.

by local absorbers) at all intensity levels and at all phases during that observation.

In Fig. 4.1, we show the color-intensity diagram of the non-bursting emission of EXO 0748-676 during all the XMM-Newton revolutions examined here (from 692 to 719). Remarkably, the data from the different observations overlap perfectly in this diagram. Since the intensity and spectral changes during revolution 719, and hence the boomerang-like

track associated with that revolution in Fig. 4.1, could be explained by changing absorbers in front of a constant X-ray source, we deduce that the spectral changes during the other observations, and thus their associated boomerang tracks in Fig. 4.1, can be explained similarly and that the underlying X-ray emission is the same during revolutions 692 to 719. If the underlying X-ray emission had been different from one observation to another, the various tracks would have appeared shifted with respect to each other, rather than being overlapping, unless a change in the underlying X-ray emission had the very same spectral signature in the color-intensity diagram as the change due to the absorbers, which is unlikely.

Therefore, in this thesis, we assume a constant underlying X-ray flux, and hence a constant accretion rate, for EXO 0748-676 throughout the observations 692 to 719. We will consider the unabsorbed X-ray flux derived by Díaz Trigo et al. (2006) from revolution 719 as representative of the unabsorbed flux for all the observations studied here. We note that the maximum PN count rate reached by EXO 0748-676 outside bursts varies at most by a factor 1.3 from one observation to another, which could be considered an upper limit to the variation of the underlying flux, if the above-mentioned interpretation of changing absorbers in front of a constant underlying X-ray emitter throughout revolutions 692 to 719 was not correct.

Using the data from revolution 719, Díaz Trigo et al. (2006) derive a persistent 0.6–10 keV absorbed flux of $2.25 \times 10^{-10} \text{ erg cm}^{-2} \text{ s}^{-1}$. This corresponds to a 0.6–10 keV unabsorbed (without any attenuation) flux of $2.81 \times 10^{-10} \text{ erg cm}^{-2} \text{ s}^{-1}$. Introducing a break at 50 keV (as found in the 0.1–100 keV BeppoSAX spectrum, Sidoli et al., 2005) in the power-law component of their model, we derive, in the 0.1–100 keV energy band, an unabsorbed flux of $8.44 \times 10^{-10} \text{ erg cm}^{-2} \text{ s}^{-1}$ that we consider as the representative bolometric underlying flux of EXO 0748-676 for revolutions 692 to 719. At 5 kpc, this implies an unabsorbed luminosity of $8.44 \times 10^{35} \text{ erg s}^{-1}$ in the 0.6–10 keV band, and $2.52 \times 10^{36} \text{ erg s}^{-1}$ in the 0.1–100 keV band. At 10 kpc, this implies a luminosity of $3.36 \times 10^{36} \text{ erg s}^{-1}$ in the 0.6–10 keV band and $1.01 \times 10^{37} \text{ erg s}^{-1}$ in the 0.1–100 keV band. We estimate the relative error on the fluxes and luminosities due to the spectral fit uncertainties to be $\sim 3\%$.

4.4 BURSTS

76 X-ray bursts are recorded during the 7 XMM-Newton observations of EXO 0748-676 (Table 4.1). As illustrated in Figs. 4.2 and 4.3 (see also

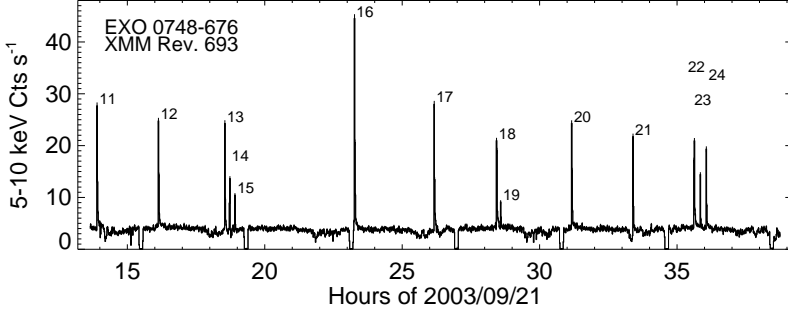


Figure 4.2: 5–10 keV EPIC PN light curve of EXO 0748-676 with a binning of 60 s during XMM-Newton revolution 693. The X-ray bursts are numbered and occur either in singlets, doublets or triplets.

the complete set of bursts in Fig. 4.16 of the appendix), most bursts occur after a wait time since a previous burst of typically 3 h, while others occur after a wait time of only ~ 12 min. We will see in Sect. 4.4.2 that there is a clear distinction between these long and short wait-time bursts. We call several consecutive bursts separated by short wait times a *bursting event*. The observations contain events of one, two and three bursts, which we refer to as *singlets*, *doublets* and *triplets*, respectively. The burst types are denoted by S1 for a singlet, D1 and D2 for the first and second burst in a doublet, respectively, and T1, T2 and T3 for the first, second and third burst in a triplet, respectively.

The observations contain 52 bursting events: 33 singlets, 14 doublets and 5 triplets. On average, one event occurs every 3 h, one singlet every 5 h, one doublet every 11 h and one triplet every 20 h. This is the first time that triplets are unambiguously and repeatedly detected in an accreting neutron star. The bursts from all the triplets are shown in Fig. 4.4 together with the bursts from one singlet and from one doublet.

To reliably compare all the bursts despite the fact that many of them occur during dipping (Fig. 4.16), unless otherwise stated, we base the bulk of our analysis on the hard 5–10 keV energy band because it is much less contaminated by the dipping activity than the soft band (cf. Sect. 4.3, Díaz Trigo et al. 2006). In addition, in Sect. 4.4.6, we perform a spectral analysis in the full 0.1–10 keV band of a sample of bursts that are the least affected by dipping, from which we derive conversion factors that we use to convert the 5–10 keV parameters values into

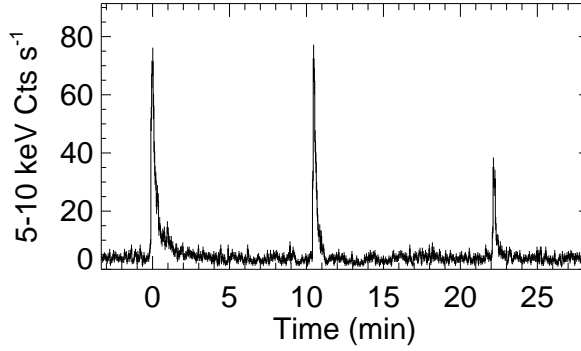


Figure 4.3: 5–10 keV EPIC PN light curve of EXO 0748-676 with a binning of 3 s showing the triplet of bursts 13, 14 and 15. Time is given in minutes from the peak time of the burst 13.

bolometric ones in the rest of the analysis. Bursts 26 and 38 contain data gaps and are excluded from part of the analysis.

4.4.1 Parameters definition

Prior to each burst, we select a reference interval free of eclipse, instrumental data gaps or other bursts, in the 1-s resolution light curve. We define the burst start time when the count rate reaches 3σ above the level in the reference segment, as the burst rises, and the burst stop time when the intensity drops back to a level of 1.1 times the mean intensity in the reference segment, as the burst decays. We define the burst duration as the separation between these burst stop and start times. The peak time is the time at which the count rate is maximum, again in the 1-s resolution 5–10 keV light curve. We define *the wait time* of a burst as the separation between its peak time and the peak time of the previous burst. We take *the event wait time to the next event* as the separation between the peak time of the first burst in the event to the peak time of the first burst in the following event.

We determine the total net counts in a burst by summing all the counts detected between the burst start and stop times and subtracting from this value an estimate of the number of persistent-emission counts that were emitted over the burst duration (average persistent count rate in the reference segment multiplied by the burst duration). The net counts in a burst is a tracer of the burst fluence. We define the net counts in the event (tracer of the event fluence) as the sum of the net counts of each burst in the event.

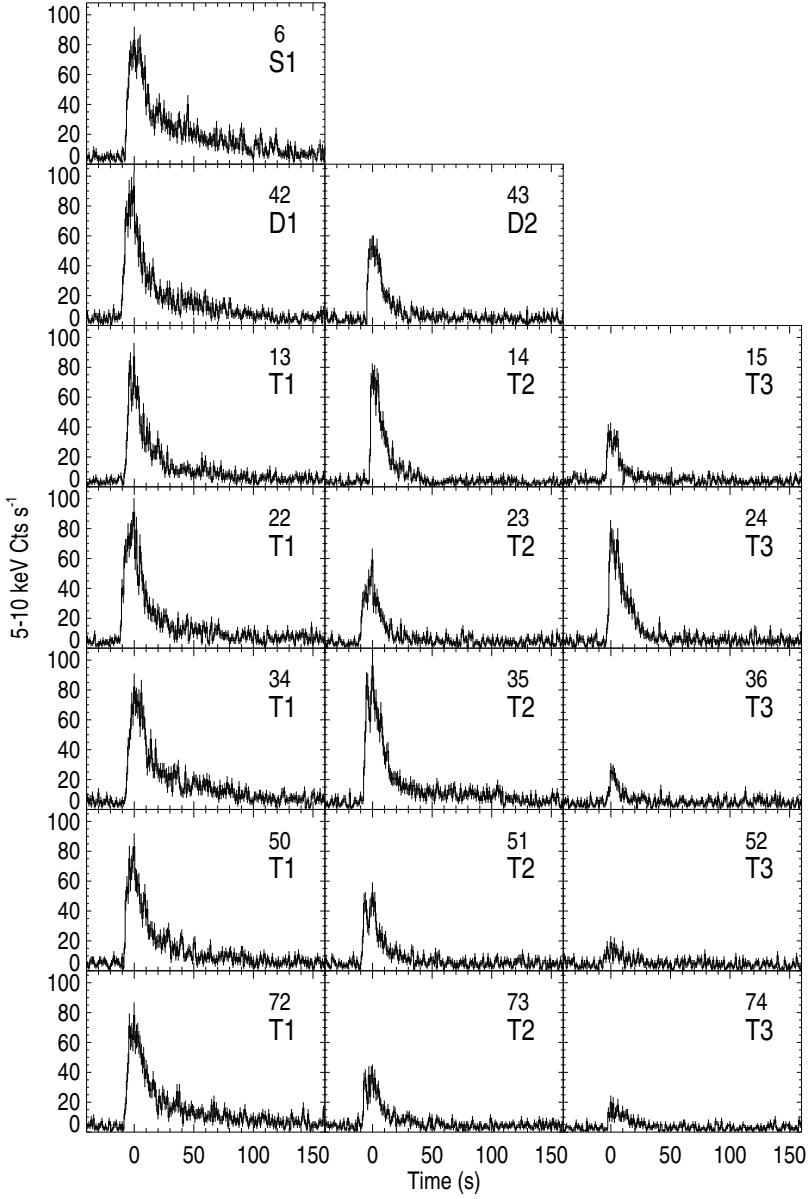


Figure 4.4: 5–10 keV EPIC PN light curves of EXO 0748-676 with a binning of 1 s showing the bursts profiles in one singlet, in one doublet and in all of the five detected triplets. The burst number and its type are indicated in each panel. Time is given in seconds from the burst peak time.

Table 4.2: Mean, minimum and maximum values of the burst peak flux, duration, fluence and α value, for each burst type, derived from the 1 s resolution EPIC PN 5–10 keV light curve, assuming a conversion factor of 8.1×10^{-11} erg cm $^{-2}$ count $^{-1}$ between the 5–10 keV net number of counts and the bolometric burst fluence, a conversion factor of 8.2×10^{-11} erg cm $^{-2}$ count $^{-1}$ between the 5–10 keV peak count rate and the bolometric burst peak flux (Sect. 4.4.6) and a bolometric persistent flux of 8.44×10^{-10} erg cm $^{-2}$ s $^{-1}$ (Sect. 4.3).

Type	t_{wait} (h or min)			Peak flux (10^{-9} erg cm $^{-2}$ s $^{-1}$)			Duration (s)			Fluence (10^{-7} erg cm $^{-2}$)			α		
	Mean	Min	Max	Mean	Min	Max	Mean	Min	Max	Mean	Min	Max	Mean	Min	Max
S1	3.20 h	2.23 h	4.64 h	7.2	5.5	11	116	55	177	1.9	0.90	3.1	53	42	102
D1	2.87 h	2.04 h	3.70 h	7.0	6.1	8.6	100	65	156	1.7	1.1	2.2	52	45	61
T1	2.46 h	2.23 h	2.79 h	6.9	6.4	7.5	81	61	94	1.4	1.2	1.6	54	49	57
S1, D1, T1	3.02 h	2.04 h	4.64 h	7.2	5.5	11	109	55	177	1.8	0.90	3.1	53	42	102
D2	13.20 min	8.40 min	19.02 min	4.7	1.7	7.5	39	22	53	0.61	0.26	1.1	12	6	17
T2	12.18 min	9.42 min	15.36 min	5.2	3.2	7.9	50	28	116	0.73	0.38	1.5	10	5	16
T3	11.70 min	10.62 min	13.02 min	2.9	1.6	6.3	23	15	42	0.30	0.091	0.87	35	8	63
D2, T2, T3	12.66 min	8.40 min	19.02 min	4.5	1.6	7.9	38	15	116	0.57	0.091	1.5	16	5	63
All types	2.05 h	8.40 min	4.64 h	6.3	1.6	11	86	15	177	1.4	0.091	3.1	40	5	102

We apply a multiplicative factor of $8.1 \times 10^{-11} \text{ erg cm}^{-2} \text{ count}^{-1}$ to convert the 5–10 keV net counts into the bolometric fluence, and a factor of $8.2 \times 10^{-11} \text{ erg cm}^{-2} \text{ count}^{-1}$ to convert the 5–10 keV peak count rate into the bolometric peak flux (see details in Sect. 4.4.6).

The α value of a burst is defined as $f_p \times t_{\text{wait}}/E_b$, where f_p is the bolometric persistent flux, t_{wait} the burst wait time and E_b the bolometric burst fluence. As the persistent flux depends on the accretion rate, the product $f_p \times t_{\text{wait}}$ is a tracer of the mass accumulated on the neutron star via accretion between the preceding burst and the considered one. In the context of thermonuclear flash models, the burst fluence is expected to be proportional to the amount of nuclear fuel available. At accretion rates where the fuel does not burn stably outside bursts, the burst fluence is thus expected to be proportional to the accumulated mass, and α to be constant, in a given bursting thermonuclear regime. Here, we determine the α values assuming a constant bolometric persistent flux of $8.44 \times 10^{-10} \text{ erg cm}^{-2} \text{ s}^{-1}$ (Sect. 4.3).

4.4.2 Parameters distributions

The peak time, wait time and type of all the bursts are listed in Table 4.7. The mean, minimum and maximum values of the burst wait time, peak flux, duration, fluence and α are given in Table 4.2 for each burst type and for some combinations of types.

Where relevant, we indicate the skewness and kurtosis of the samples. The skewness of a sample Y_1, Y_2, \dots, Y_N is defined as $\sum_{i=1}^N (Y_i - \bar{Y})^3 / (N - 1)s^3$, where \bar{Y} is the mean, s the standard deviation, and N the number of data points. The skewness is expected to be 0 for a symmetric distribution, < 0 for a skewed left one, and > 0 for a skewed right one. The kurtosis, defined as $[\sum_{i=1}^N (Y_i - \bar{Y})^4 / (N - 1)s^4] - 3$, is expected to be 0 for a normal distribution, < 0 for a flatter one, and > 0 for a more peaked one.

We use the two-sample Kolmogorov-Smirnov test to estimate the probability, P_{same}^{a-b} , that two samples a and b come from the same distribution. Since there are only 5 triplets (as compared to 14 doublets and 33 singlets), the probabilities involving the triplets are inferred from particularly small numbers and should be considered with care.

Wait time

The histograms of the wait times are shown in Fig. 4.5 for each burst type and for some combinations of burst types. The wait times range between 8.4 min and 4.6 h, but we observe no burst with a wait time between 20 min and 2 h. Two distinct groups of bursts are thus clearly

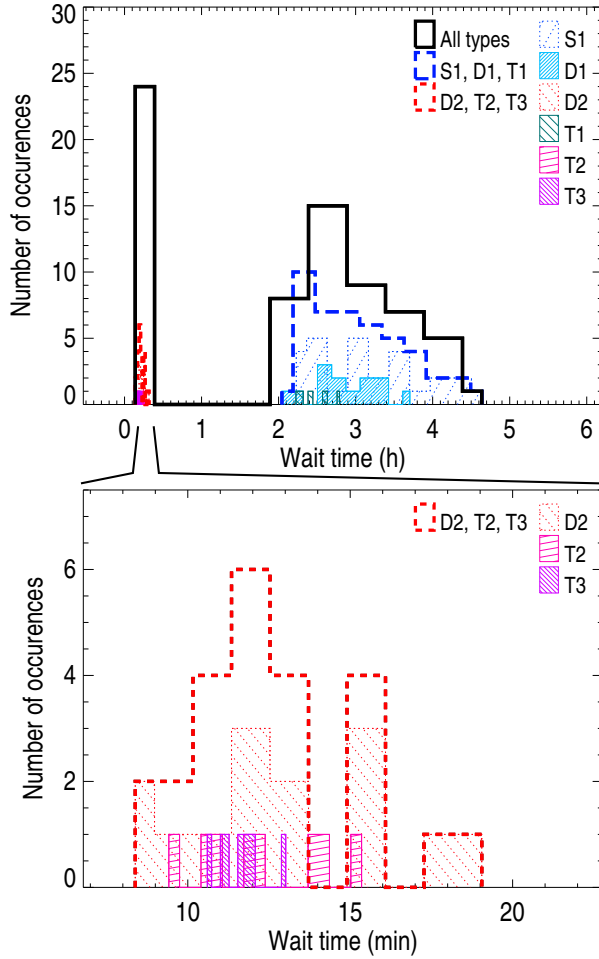


Figure 4.5: Histograms of the wait times. The bottom plot zooms in on the top one. The histograms are built independently for each burst type and for some combinations of types, using always 10 bins. Consequently, the bin size is different from one histogram to another. Furthermore, the size of the first and last bins is adjusted to match the exact observed range of wait times for a given histogram.

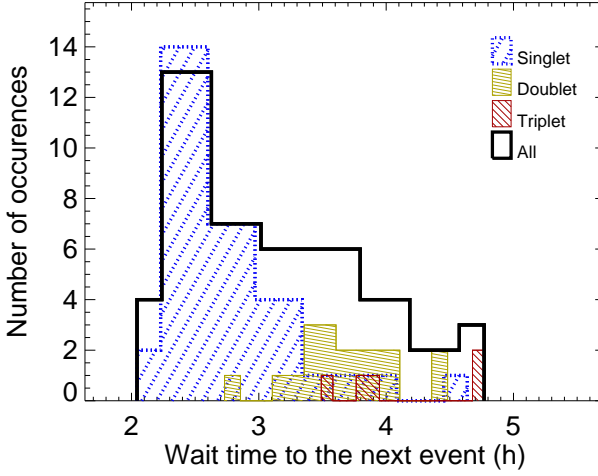


Figure 4.6: Histograms of the event wait times to the next event, built independently for the singlets, doublets, triplets and for all events, using 8 bins.

visible: one group made up of the S_1 , D_1 and T_1 bursts which occur after a mean wait time of 3.0 h, and another group consisting of the D_2 , T_2 and T_3 bursts which occur after a mean wait time of only 12.7 min. We will refer to these two groups as the bursts with long wait times (LWT) and short wait times (SWT), respectively. This distinction is confirmed by the very low probability ($P_{\text{same}}^{\text{long-short}} = 7 \times 10^{-14}$) that the wait times from the two groups come from the same distribution. The SWT histogram and the LWT histogram have the same skewness of 0.64, and a similar kurtosis of -0.57 for the LWT and -0.31 for the SWT.

Inside the LWT group, the wait time distributions from two different burst types are not significantly different ($P_{\text{same}}^{S_1-D_1} = 37\%$, $P_{\text{same}}^{S_1-T_1} = 23\%$, $P_{\text{same}}^{D_1-T_1} = 25\%$). Inside the SWT group, the D_2 , T_2 and T_3 bursts also seem to follow the same wait times distribution ($P_{\text{same}}^{D_2-T_2} = 96\%$, $P_{\text{same}}^{T_2-T_3} = 70\%$, $P_{\text{same}}^{D_2-T_3} = 35\%$).

Fig. 4.6 shows the histograms of the event wait time to the next event. While the doublets and the triplets seem to follow the same distribution ($P_{\text{same}}^{\text{doublet-triplet}} = 58\%$), the singlets follow a significantly different distribution than that of the doublets and triplets ($P_{\text{same}}^{\text{singlet-doublet}} = 0.0015\%$ and $P_{\text{same}}^{\text{singlet-triplet}} = 0.2\%$). For a new event to occur, one has

to wait on average 4.2 h after a triplet, 3.7 h after a doublet, but only 2.7 h after a singlet.

Peak flux

The histograms of the burst peak flux are shown in Fig. 4.7 (top; see also Table 4.2). Despite their overlap, the LWT and SWT peak flux histograms are inconsistent with coming from the same distribution ($P_{\text{same}}^{\text{long-short}} = 1.5 \times 10^{-8}$). The mean peak flux of the LWT bursts is a factor 1.6 higher than that of the SWT bursts. The mean peak flux of the LWT bursts, $7.2 \times 10^{-9} \text{ erg cm}^{-2} \text{ s}^{-1}$, corresponds to a luminosity of $2.2 \times 10^{37} \text{ erg s}^{-1}$ at 5 kpc or $8.6 \times 10^{37} \text{ erg s}^{-1}$ at 10 kpc. The mean peak flux of the SWT bursts, $4.5 \times 10^{-9} \text{ erg cm}^{-2} \text{ s}^{-1}$, corresponds to a luminosity of $1.3 \times 10^{37} \text{ erg s}^{-1}$ at 5 kpc or $5.4 \times 10^{37} \text{ erg s}^{-1}$ at 10 kpc.

The LWT peak flux histogram is very peaked (kurtosis of 5.68) while that of the SWT group is flat (kurtosis of -1.06). The S₁, D₁ and T₁ bursts have similar peak flux distributions ($P_{\text{same}}^{S_1-D_1} = 84\%$, $P_{\text{same}}^{S_1-T_1} = 96\%$, $P_{\text{same}}^{D_1-T_1} = 99\%$). In the SWT group, the D₂ and T₂ bursts have similar peak flux distributions ($P_{\text{same}}^{D_2-T_2} = 99\%$), while the T₃ bursts seem to follow a marginally different one ($P_{\text{same}}^{D_2-T_3} = 4.5\%$, $P_{\text{same}}^{T_2-T_3} = 3.6\%$), with lower values.

In a given doublet (triplet), the peak flux of the D₂ (T₂) is significantly lower than that of the D₁ (T₁) in 10/13 (3/5) cases, and similar to it in the other cases (see Fig. 4.4). The peak flux of the T₃ burst is always significantly less than that of the T₂ burst, except for the strong T₃ burst number 24.

Fluence and duration

The histograms of the burst fluence are shown in Fig. 4.7 (middle; see also Table 4.2). The fluence sample is clearly bimodal ($P_{\text{same}}^{\text{long-short}} = 7.6 \times 10^{-14}$), the SWT bursts being less fluent by a factor ~ 3 than the LWT bursts on average. The mean fluence of the LWT bursts is $1.8 \times 10^{-7} \text{ erg cm}^{-2}$ and corresponds to $5.3 \times 10^{38} \text{ ergs}$ at 5 kpc or $2.1 \times 10^{39} \text{ ergs}$ at 10 kpc. The mean fluence of the SWT bursts is $5.7 \times 10^{-8} \text{ erg cm}^{-2}$ and corresponds to $1.7 \times 10^{38} \text{ ergs}$ at 5 kpc or $6.8 \times 10^{38} \text{ ergs}$ at 10 kpc.

Inside the LWT group, the fluences from the S₁ and D₁ bursts seem to be drawn from the same distribution ($P_{\text{same}}^{S_1-D_1} = 26\%$), while the T₁ bursts would follow a marginally different one ($P_{\text{same}}^{S_1-T_1} = 4.1\%$, $P_{\text{same}}^{D_1-T_1} = 5.4\%$), the T₁ being on average less fluent than the D₁ or the S₁ bursts. Inside the SWT group, the D₂ and T₂ have similar fluence distributions ($P_{\text{same}}^{D_2-T_2} = 93\%$), while the T₃ have marginally different

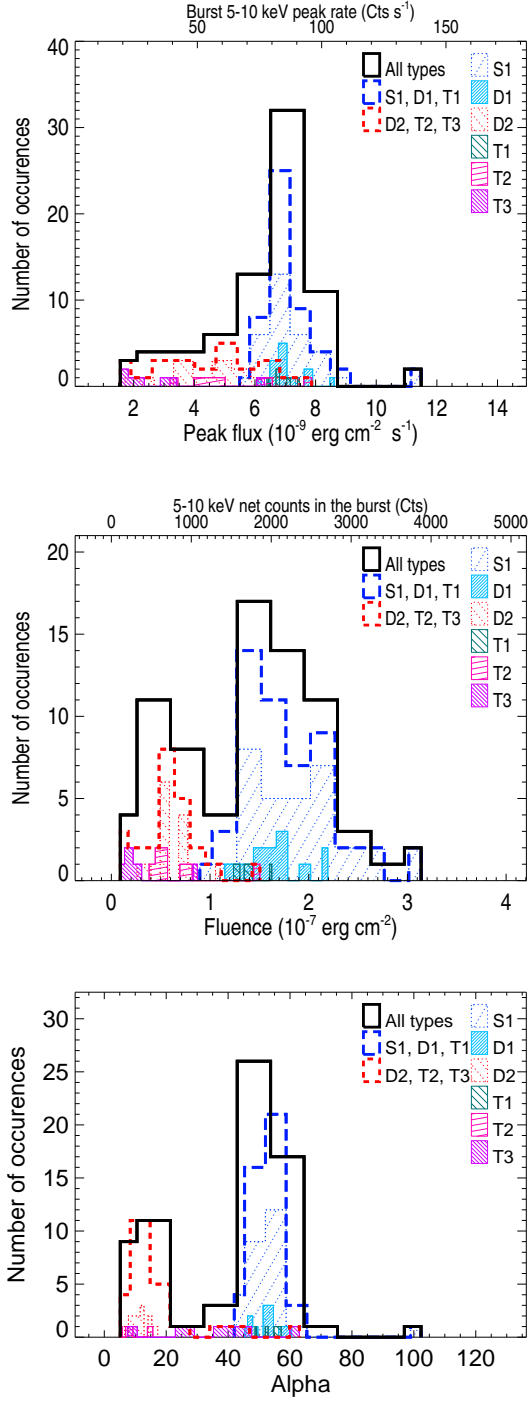


Figure 4.7: Histograms of the burst peak flux (top), fluence (middle) and α values (bottom) built as in Fig. 4.5.

(lower) ones ($P_{\text{same}}^{\text{D2-T3}} = 0.7\%$, $P_{\text{same}}^{\text{T2-T3}} = 3.6\%$). The histograms of the burst duration (not shown here) are very similar to the fluence ones.

In a given doublet, the D2 burst is always shorter and less fluent than the D1. In a given triplet, the duration and fluence of the T2 is always less or equal to that of the T1. The T3 burst, except for the strong T3 burst number 24, has a duration and fluence less than that of the T2 burst.

Alpha

The histograms of the α values are shown in Fig. 4.7 (see also Table 4.2). The sample is clearly bimodal ($P_{\text{same}}^{\text{long-short}} = 1.0 \times 10^{-12}$), the mean α value being smaller by a factor ~ 3.3 for the SWT bursts ($\alpha = 16$) than for the LWT ones ($\alpha = 53$). The α histogram for the S1 bursts is very peaked (kurtosis of 11.4) compared to all the other burst types (kurtosis between -0.4 and -2). Inside the LWT group, the S1, D1 and T1 bursts seem to follow the same α distribution ($P_{\text{same}}^{\text{S1-D1}} = 90\%$, $P_{\text{same}}^{\text{S1-T1}} = 48\%$, $P_{\text{same}}^{\text{D1-T1}} = 60\%$). Inside the SWT group, the T3 bursts seem to follow a marginally different α distribution from the D2 and T2 bursts ($P_{\text{same}}^{\text{D2-T3}} = 1.9\%$, $P_{\text{same}}^{\text{T2-T3}} = 3.6\%$ while $P_{\text{same}}^{\text{D2-T2}} = 32\%$).

4.4.3 Relation between burst fluence and accumulated mass

Fig. 4.8 (left and middle panels) shows the burst fluence as a function of the product of the persistent flux times the wait time, which is a tracer of the mass accumulated by accretion before the burst. Here, the accumulated mass tracer is simply proportional to the wait time because we assume the underlying persistent flux is constant (Sect. 4.3).

Among the LWT types, the fluence is strongly correlated with the accumulated mass tracer, with correlation coefficients of 0.91 for the S1, 0.89 for the D1 and 0.81 for the T1 bursts. For each LWT type, the fluence is well described by a linear function of the accumulated mass tracer ($E_b = \alpha^{-1} \times [f_p \times t_{\text{wait}}] + E_0$). E_0 is the offset energy at zero burst interval. The best-fit parameter values α and E_0 are listed in Table 4.3. Within the 90% confidence range, both α and E_0 are consistent with being the same for the S1, D1 and T1 bursts. For all the LWT bursts together, the α value obtained from the fit is 46 ± 4 and E_0 is $(-2.3 \pm 1.7) \times 10^{-8} \text{ erg cm}^{-2}$. E_0 is consistent with 0 within 3σ , and consistent with being negative within the 90% confidence range (1.65σ). A negative value of E_0 would indicate that a part $|E_0| = 2.3 \times 10^{-8} \text{ erg cm}^{-2}$ of the total available energy is not burned in the burst. This corresponds to an energy of $6.9 \times 10^{37} \text{ ergs}$ at 5 kpc or $2.7 \times 10^{38} \text{ ergs}$

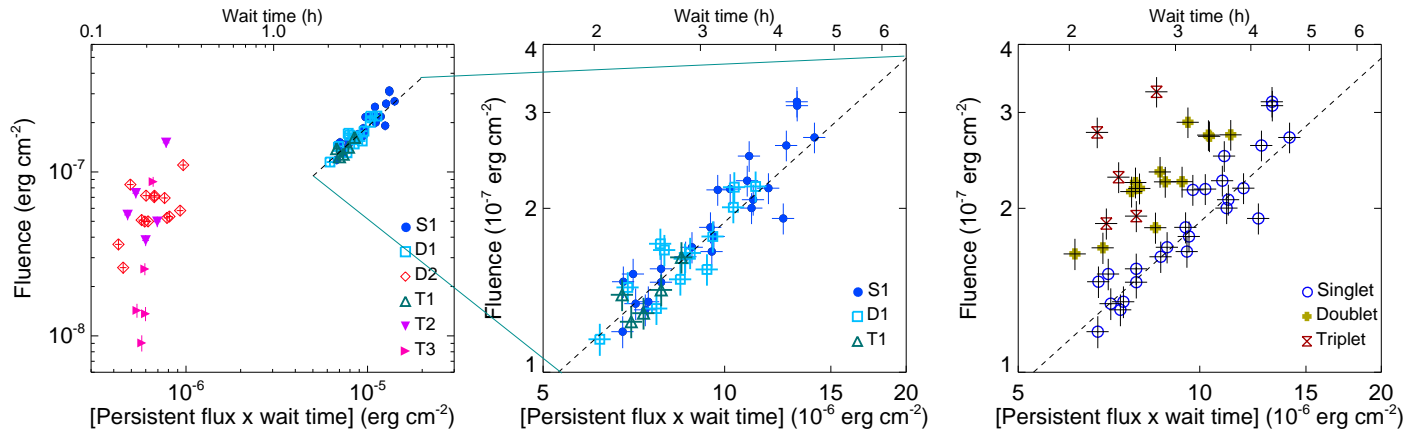


Figure 4.8: **Left:** Burst fluence as a function of persistent flux times wait time (accumulated mass tracer). The line indicates the mean α value for the LWT bursts ($\alpha = 53$). **Middle:** zoom in on the left panel. **Right:** Event fluence as a function of the accumulated mass tracer. The line is the same as in the left panel.

Table 4.3: Best-fit parameters α and E_0 , and their 90% confidence errors, obtained from fitting E_b as $\alpha^{-1} \times [f_p \times t_{\text{wait}}] + E_0$ (see text).

Type	α	E_0 (10^{-8} erg cm $^{-2}$)
S1	45 ± 5	-2.5 ± 2.3
D1	49 ± 11	-1.1 ± 3.7
T1	50 ± 40	1 ± 13
S1, D1, T1	46 ± 4	-2.3 ± 1.7

at 10 kpc, equivalent to 13% of the mean energy released by the LWT bursts.

Among the SWT types, only the T3 bursts show a strong correlation (coefficient of 0.86) between the fluence and the accumulated mass, which can be described by a line with best-fit parameters $\alpha = 1.2 \pm 0.4$ and $E_0 = (-4.5 \pm 4.6) \times 10^{-7}$ erg cm $^{-2}$ (90% confidence errors). The fluence of the D2 or T2 bursts is much less strongly correlated with the accumulated mass, the coefficients being 0.53 for the D2 and 0.62 for the T2, and no acceptable linear fit could be obtained. So, apart maybe for the T3 bursts, the fluence of a SWT burst does not strongly depend on the amount of material freshly accreted just before the SWT burst.

Combining SWT and LWT types (e.g. the whole sample of bursts, or the D1 and D2 combined), we could not obtain acceptable (with reduced $\chi^2 < 2$) linear fits between the fluence and the accumulated mass tracer. Thus, the SWT bursts are inconsistent with following the same fluence- accumulated mass relation as the LWT bursts.

Fig. 4.8 (right) shows the *event* fluence as a function of the accumulated mass tracer. At a given accumulated mass, a triplet is generally more fluent than a doublet which is more fluent than a singlet. When all the events are considered together, the event fluence is only weakly correlated to the accumulated mass tracer (correlation coefficient of 0.38). The fluence of the doublets correlates with the accumulated mass. However, this correlation is not better than the one observed for the D1 bursts only. Similarly the correlation is not improved by considering the triplets (coefficient of 0.44) rather than the T1 bursts (coefficient of 0.81). This effect is visible when the left and right panels of Fig. 4.8 are compared: the dispersion is higher for the doublets than for the D1 and higher for the triplets than for the T1. This suggests that the fluence of a D2 burst (and analogously of a T2-T3 pair) does

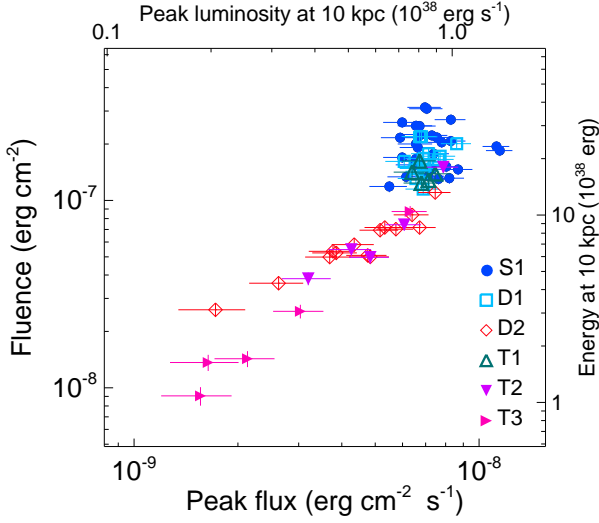


Figure 4.9: Bolometric burst fluence as a function of the bolometric peak flux. The right and top axis indicate the corresponding energy and peak luminosity assuming an isotropic emission at a distance of 10 kpc.

not strongly depend on the amount of material accreted before the D1 (or T1) burst of the considered event.

4.4.4 Relation between fluence and flux

Fig. 4.9 shows the burst fluence as a function of the burst peak flux. While the two quantities are not strongly correlated for the S1, D1 and T1 bursts (with linear correlation coefficients of 0.04, 0.29, and -0.27, respectively), the fluence and flux are strongly correlated in the case of the D2, T2 and T3 bursts, with correlation coefficients of 0.93, 0.94 and 0.99, respectively.

4.4.5 Profiles

Fig. 4.10 shows the profiles obtained by averaging the 5–10 keV light curves of all the bursts of a given type, except the exceptionally strong T2 and T3 bursts number 35 and 24. After subtracting the persistent count rate level before the bursts, the decay of all these profiles is well described by a model consisting of two exponential parts. The best-fit values of the characteristic decay times, τ_1 and τ_2 , and of the transition

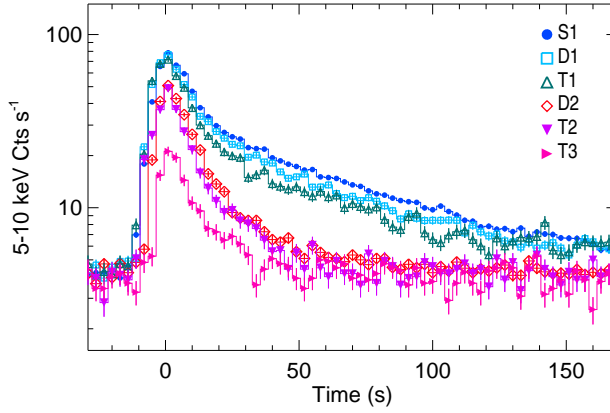


Figure 4.10: Average profiles for each burst type, obtained respectively from 32 S1, 13 D1, 14 D2, 5 T1, 4 T2 and 4 T3 bursts. The strong T2 and T3 bursts number 35 and 24 are excluded. The binning is 3 s. Note that the logarithmic scale of the intensity axis makes an exponential decay appear as a straight line.

time t_1 are given in Table 4.4. The first part of the decay is always faster than the second ($\tau_1 < \tau_2$). The decays of the average S1, D1 and T1 profiles are similar to each other, with $\tau_1 \sim 15$ s and $\tau_2 \sim 52$ s. The D2 and T2 average profiles decay more rapidly, with both τ_1 and τ_2 being shorter. For the T3 average profile, only one exponential component is detected (including a second one does not improve the fit quality). Its decay time is similar to that of the first component of the D2 and T2 average profile.

The top panel of Fig. 4.11 shows the average S1, D1, T1 and D2 profiles obtained from bursts having a similar peak intensity in the range 77–96 counts s^{-1} , and a similar wait time in the range 2–2.8 h for the S1, D1 and T1. The best-fit model of their decay with two exponential parts is given in Table 4.5. While the S1, D1 and T1 profiles are similar, the D2 profile, *at the same peak intensity level*, shows a different and much faster decay which can be modeled by only one exponential decay.

The only T2 and T3 bursts that have a peak intensity in the range 77–96 counts s^{-1} are the exceptionally strong ones number 35 and 24, respectively. The best-fit model of their decay is given in Table 4.5. The decay of the strong T2 burst number 35 shows a fast part followed by a slow flat component. Interestingly, the decay of the strong T3 burst

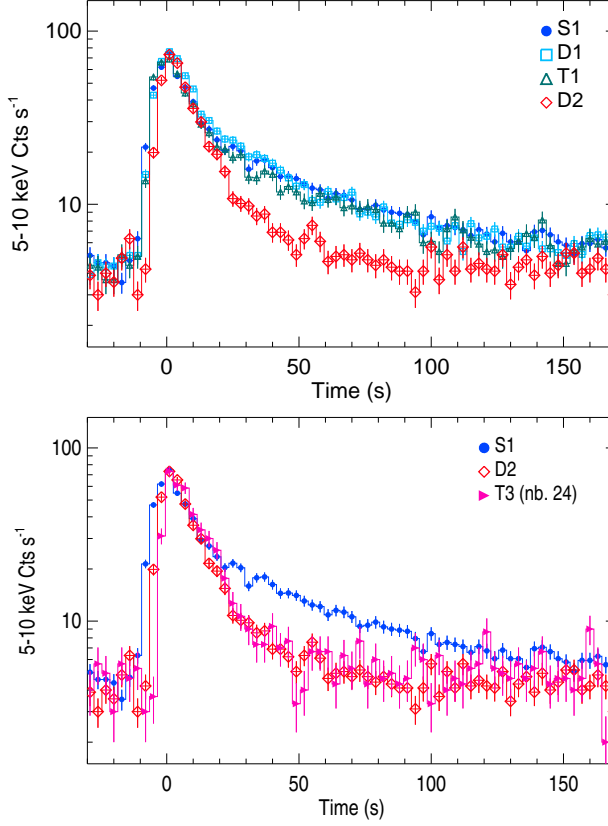


Figure 4.11: **Top:** Average S1, D1, T1 and D2 profiles, obtained respectively from 5 S1, 5 D1, 3 T1 and 3 D2 bursts having a similar peak intensity (77–96 counts s⁻¹), and a similar wait time for the S1, D1 and T1 (2–2.8 h). Time is given from the burst peak time and the binning is 3 s. **Bottom:** The strong T3 number 24 compared with the S1 and D2 average profiles from the top panel.

Table 4.4: Best-fit parameter values and 90% confidence errors for the decay of the average profiles by burst type (Fig. 4.10). We subtract the persistent count rate level before the burst and fit each persistent-subtracted burst decay using a continuous function of two exponential parts: $B_0 e^{-t/\tau_1}$ between t_0 and t_1 , and $B_1 e^{-t/\tau_2}$ between t_1 and t_2 . We set t_0 to the burst peak time (0 s), t_2 to the first time where the persistent-subtracted intensity, B , reaches a level of 0, and B_1 to $B_0 e^{(-t_1/\tau_1)}$. The free parameters are the persistent-subtracted intensity, B_0 , at the burst peak time, the characteristic decay times, τ_1 and τ_2 , and the transition time t_1 . We indicate the time, t_{stop} , where the intensity, I , reaches back a level of 1.1 times the level before the burst. For the profiles whose fit was not improved by including a second exponential component, we give only the decay time of the first and only exponential component.

Type	B_0 (counts s ⁻¹)	τ_1 (s)	τ_2 (s)	t_1 (s)	t_{stop} (s)
S1	79.7 ^{+1.7} _{-0.5}	16.2 ^{+0.4} _{-0.1}	56.9 ^{+2.1} _{-0.6}	20.7 ^{+0.2} _{-0.7}	180
D1	74.1 ^{+3.0} _{-0.8}	15.9 ^{+0.6} _{-0.2}	51 ⁺⁴ ₋₁	21.6 ^{+0.4} _{-1.5}	126
T1	71.1 ^{+4.8} _{-1.5}	13.8 ^{+1.0} _{-0.3}	48 ⁺¹² ₋₂	20.6 ^{+0.6} _{-2.3}	103
D2	53.9 ^{+2.2} _{-1.5}	11.0 ^{+0.6} _{-0.2}	19 ⁺¹³ ₋₂	25 ⁺² ₋₅	52
T2	50.5 ^{+4.6} _{-2.7}	9.0 ^{+1.1} _{-0.4}	14 ⁺¹⁰ ₋₁	15 ⁺³ ₋₅	45
T3	17.3 ^{+8.2} _{-0.4}	10.8 ^{+8.7} _{-0.2}	—	—	33

(bottom panel of Fig. 4.11) is very similar to that of the average D2 profile *at the same peak intensity level*.

4.4.6 Spectral properties

Color intensity diagram

Fig. 4.12 shows the color, C , as a function of the hard intensity, I , during the decay of the averaged profiles obtained, respectively, from 15 S1, 8 D1, 10 D2, 2 T1, 1 T2 and 1 T3 bursts chosen for being the least contaminated by the dipping activity. We find that, for each burst type, $\log(C)$ can be described by a linear function of $\log(I)$ ($\log(C) = a \times \log(I) + b$). For a burst emitting like a blackbody, the

Table 4.5: Same as Table 4.4 for the average profiles by type from bursts having a peak intensity in the range 77–96 counts s^{-1} and a wait time in the range 2–2.8 h for the S1, D1 and T1 (Fig. 4.11).

Type	B_0 (counts s^{-1})	τ_1 (s)	τ_2 (s)	t_1 (s)	t_{stop} (s)
S1	70^{+5}_{-1}	$14.0^{+1.1}_{-0.2}$	49^{+10}_{-2}	$19.9^{+0.5}_{-2.6}$	116
D1	81^{+6}_{-1}	$14.2^{+1.2}_{-0.2}$	40^{+8}_{-1}	$20.3^{+0.5}_{-3.0}$	105
T1	68^{+8}_{-2}	$13.7^{+1.9}_{-0.2}$	45^{+24}_{-2}	$21.0^{+0.6}_{-4.6}$	101
D2	75^{+10}_{-1}	$11.6^{+1.5}_{-0.2}$	—	—	50
T2	78^{+22}_{-2}	$13.0^{+3.5}_{-0.2}$	$149^{<-277}_{-18}{}^a$	$30.7^{+0.6}_{-9.0}$	108
T3	92^{+8}_{-6}	$10.8^{+2.3}_{-0.3}$	—	—	37

^a The second component of this decay is effectively flat, which shows in our fits as a long positive or negative exponential decay time.

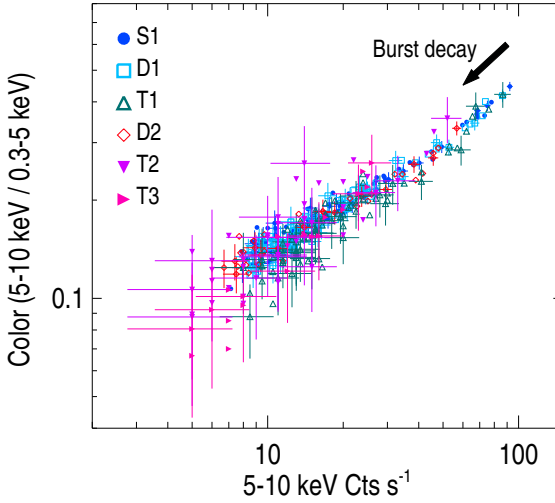


Figure 4.12: Color as a function of hard intensity during the decay of the averaged profiles by type obtained, respectively, from 15 S1, 8 D1, 10 D2, 2 T1, 1 T2 and 1 T3 bursts which are the least affected by the dipping activity. Error bars are shown on one third of the points which represent each 1 s.

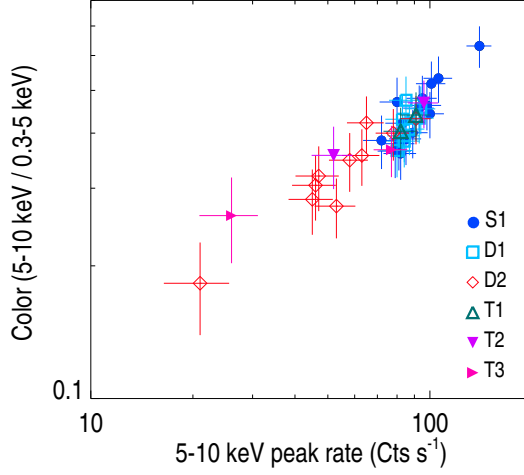


Figure 4.13: Color as a function of the hard intensity at the burst peak for the individual bursts the least affected by dipping activity.

bolometric flux F is expected to depend only on the area, A , of the emitting region and on the blackbody temperature, T , as $F \propto AT^4$. Since C is a tracer of T and I is a tracer of F , any difference in the slope a between burst types would indicate a difference in the flux to temperature dependence ($F \propto T^4$), while any difference in the intercept b would indicate a difference in the area A of the emitting region. We find that, within 3σ , the slope a is consistent with being the same for all burst types. So the comparison of the averaged color-intensity diagrams by burst types does not indicate differences by type in the burst temperature to flux dependence. The best-fit values of the intercept b are consistent with being the same within 3σ for the S1, D1, T1, T2 and T3 types on one hand, and for S1, D1, D2, T2 and T3 types on the other hand, indicating a difference only between the T1 and D2 types. This difference suggests that the apparent emitting area (or blackbody radius) would be on average larger for the T1 than for the D2 bursts.

Fig. 4.13 shows the color at the burst peak as a function of the intensity at the peak, for the individual bursts the least affected by dipping activity. The two quantities are strongly correlated. This implies that the peak temperature distributions have similar properties as the peak fluxes distributions shown in Fig. 4.7, with a clear distinction between

the SWT and the LWT bursts, the latter having higher and less variable peak temperatures. In addition, the correlation in Fig. 4.13 is consistent with that obtained from the averaged decays (Fig. 4.12). So the relation between the temperature and the flux is consistent with being the same for all burst types and for any time of the burst decay including at the peak.

This analysis shows that there is no indication for strong spectral differences between the various burst types, the flux or apparent emitting area being approximately the same at a given temperature during the decay. There is however marginal evidence that the apparent emitting area is on average larger for the first bursts in triplets than for the second bursts in doublets. This could point to differences in the structure or composition of the neutron star atmosphere/outer layers (see Sect. 4.5 and the discussion in Gottwald et al. 1987).

Time-resolved spectral modeling

We select five singlets (bursts 1, 12, 16, 33 and 37, see Appendix), one doublet (bursts 4 and 5) and two triplets (bursts 22, 23, 24 and 34, 35, 36) that are the least contaminated by dipping activity and perform their time-resolved spectral analysis using version 11.3.1 of the XSPEC package. We divide each burst into 3 to 6 intervals, with the interval around the burst peak chosen shorter than intervals in the tail. We extract a spectrum in each burst interval from which we subtract a reference persistent spectrum obtained from segments just before and after the burst. We add a 2% systematic error to account for calibration uncertainties.

Since the net emission of type I X-ray bursts is generally well described by a blackbody (see e.g. Swank et al., 1977; Lewin et al., 1993), we model the net 0.1–10 keV spectrum with an absorbed blackbody. We fix the hydrogen column density, N_{H} , of the neutral absorber to $0.1 \times 10^{22} \text{ cm}^{-2}$ (Sidoli et al., 2005). We also include a Gaussian with a centroid energy set to 0 to describe emission below ~ 2 keV which is in excess of the blackbody model. This soft excess may be related to a temporary increase, due to the burst irradiation, of the ionization level of the local absorbing material in the line-of-sight. The material becomes more transparent, especially at low energy, than it was just before the burst. Consequently, the subtraction of the spectrum extracted prior to the burst from the spectrum extracted during the burst yields to an apparent soft excess in the net spectrum. This component will not be investigated further here. A soft excess was reported in other bursts from EXO 0748-676 and interpreted in a similar way by Asai & Dotani (2006).

Table 4.6: Averaged results of fits of the 0.1–10 keV spectra extracted during intervals of 13 bursts, with a model consisting of an absorbed blackbody and a Gaussian. The parameters are the hydrogen column density N_{H} , the blackbody temperature kT_{bb} and normalization N_{bb} (defined as R_{km}^2/d_{10}^2 where R_{km} is the source radius in km and d_{10} the distance to the source in units of 10 kpc), the Gaussian centroid energy E , width σ and normalization N_{G} . For a given burst, we averaged the best-fit values from the intervals near the peak on one hand, and from the intervals in the tail on the other hand. A range indicates the spread in the obtained averaged values for the different bursts. Uncertainties are the average errors of the parameters at 1σ confidence level. χ_{reduced}^2 is calculated using 50 degrees of freedom. Its average and root mean squared are given.

	Peak	Tail
N_{H} (10^{22} cm^{-2})	0.1 (fixed)	0.1 (fixed)
kT_{bb} (keV)	$(1.54 - 2.13) \pm 0.12$	$(0.93 - 1.39) \pm 0.09$
N_{bb}	$(6 - 49) \pm 5$	$(7 - 39) \pm 5$
E (keV)	0 (fixed)	0 (fixed)
σ (keV)	$(0.5 - 0.8) \pm 0.6$	$(0.40 - 0.84) \pm 0.10$
N_{G} ($\text{cts cm}^{-2}\text{s}^{-1}$)	$(0.15 - 1.94) \pm 0.10$	$(0.08 - 0.36) \pm 0.05$
χ_{reduced}^2	1.1 ± 0.2	1.2 ± 0.3

We obtain good fits for each interval. Fig. 4.14 (left) shows the derived blackbody temperatures and bolometric fluxes as a function of time. Fig. 4.14 (right) shows the blackbody radius (top) and the bolometric flux (bottom) as a function of the blackbody temperature. For a given burst, we average the best-fit parameter values over the intervals near the peak on one hand, and over the intervals in the tail on the other hand. In Table 4.6, we give the range of these peak and tail values covered by our burst sample. The blackbody surface temperature kT_{bb} lies in the interval $(0.93 - 2.13) \pm 0.11$ keV, where higher values are found in the burst peak and lower values in the burst tail. There is no evidence for photospheric expansion. The normalization of the blackbody component and hence the radius of the emitting region is consistent with being constant throughout a burst and consistent with being the same for all the bursts studied. The average radius of the blackbody component is 2.4 km assuming a source distance of 5 kpc, and 4.9 km assuming a distance of 10 kpc, with an average uncertainty of 44%. This blackbody radius, since derived from a measured color temperature rather than the effective temperature, is an underestimate of the physical radius of the neutron star (e.g. London et al., 1984).

Using the previous spectral models, we further calculate the unabsorbed bolometric flux of the blackbody component for each interval, and finally the bolometric burst fluence by integrating over the whole burst. We find that, for our sample of bursts, the bolometric fluence linearly correlates with the 5–10 keV net counts in the burst. This means that the ratio between the bolometric fluence and the 5–10 keV net counts in the burst is consistent with being the same for all bursts types. We derive a value of $(8.1 \pm 0.3) \times 10^{-11}$ erg cm⁻² count⁻¹ for this ratio. Analogously we find a ratio between the bolometric burst peak flux and the 5–10 keV peak count rate of $(8.2 \pm 0.3) \times 10^{-11}$ erg cm⁻² count⁻¹. These ratios serve to estimate the bolometric fluence and peak flux from the 5–10 keV counts for all other bursts, even when they are contaminated by dipping.

4.5 COMPARISON WITH THE EXOSAT OBSERVATIONS

In 1985, EXOSAT observed EXO 0748-676 at different persistent 0.1–20 keV fluxes between 3 and 18×10^{-10} erg cm⁻² s⁻¹ (Parmar et al., 1986; Gottwald et al., 1986). 26 bursts were observed, including four doublets with a burst separation of the order of 10–20 min (Gottwald et al., 1986). The doublet phenomenon only occurred when the persistent 0.1–20 keV flux was below 5×10^{-10} erg cm⁻² s⁻¹, and was part of an overall correlation of the burst properties with changing

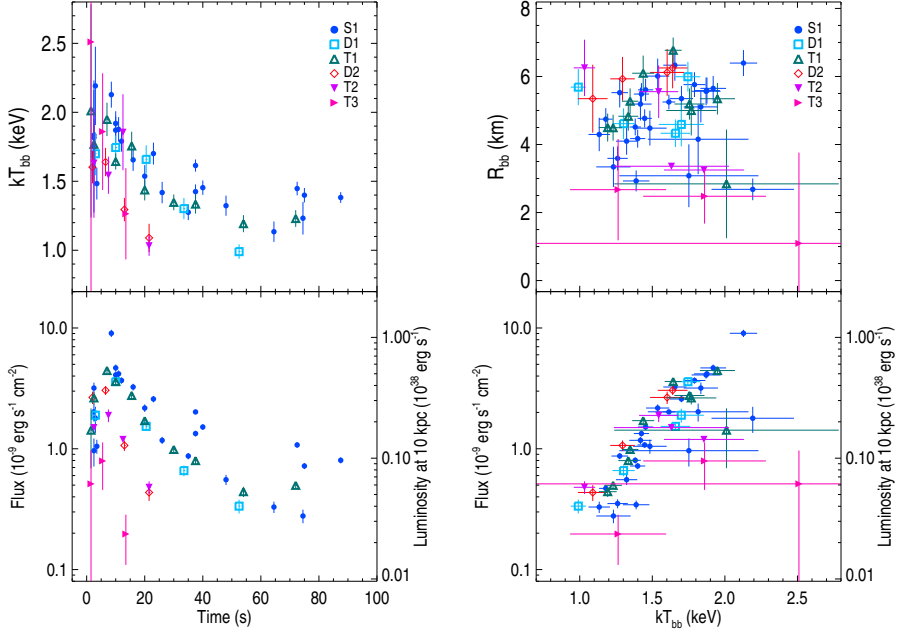


Figure 4.14: Results of the time-resolved spectral analysis of bursts number 1, 12, 16, 33 and 37 (S1), 4 (D1), 5 (D2), 22 and 34 (T1), 23 (T2), and 36 (T3). *Left*: Blackbody temperature (top) and bolometric flux (bottom) as a function of the time since burst onset. *Right*: Blackbody radius (top) and bolometric flux (bottom) as a function of the blackbody temperature.

mass accretion rate. As the persistent flux increased, (i) the wait time of the LWT bursts increased from ~ 1.8 up to 16 h, (ii) their shape changed from a ‘slow’ (long tail) to a ‘fast’ profile sometimes showing photospheric expansion, (iii) their flux at a given temperature increased, and equivalently (iv) their apparent blackbody radius at a given temperature increased. Gottwald et al. (1986) hypothesized that the persistent flux dependent variations in the burst properties could be caused by the flashes changing from helium-dominated at high accretion rates, to hydrogen-triggered hydrogen-helium flashes at low accretion rates. They further speculated that double bursts could be a feature of hydrogen-triggered hydrogen-helium flashes.

In 1986, EXOSAT caught EXO 0748-676 at a persistent 0.1–20 keV flux of $5 \times 10^{-10} \text{ erg cm}^{-2} \text{ s}^{-1}$ (Gottwald et al., 1987). 11 bursts were observed and showed a regular pattern with a long recurrence time always followed by a short one, reminiscent of the double burst phenomenon, but with longer wait times, in the range 20–70 min for the D2-like bursts. All the burst properties were otherwise consistent with that of bursts in the slow mode (*i.e.* low states) of 1985.

Using the spectral model by Díaz Trigo et al. (2006) (see Sect. 4.3), we derive an unabsorbed flux of $4.7 \times 10^{-10} \text{ erg cm}^{-2} \text{ s}^{-1}$ in the 0.1–20 keV band for EXO 0748-676 during the 2003 XMM-Newton observations, indicating that the LMXB was again in a low state. We further suggest that the source state in 2003 is likely closer to the lowest states of 1985 than to the low state of 1986 since the unabsorbed EXOSAT fluxes are probably underestimated compared to the XMM-Newton ones because of the local neutral and ionized absorbers included in the XMM-Newton spectral models.

The comparison of Fig. 4.14 with Figs. 6 and 7 of Gottwald et al. (1986) and Figs. 4 and 5 of Gottwald et al. (1987) indicates that the spectral properties of the XMM-Newton bursts are all consistent with that of EXOSAT bursts in the slow mode (low states). In particular, the XMM-Newton values of the blackbody radius ($4.9 \pm 2.1 \text{ km}$ on averaged) agree well with the EXOSAT values obtained in the low states whereas larger radii of $\sim 9 \text{ km}$ had been obtained in higher states. These variations in the blackbody radius for a given temperature are more likely related to a change in the structure and composition of the neutron star outer layers or atmosphere which distorts the blackbody spectrum than to real variations of the emitting area (Gottwald et al., 1987). In any case, the blackbody radius, since derived from a measured color temperature rather than the effective temperature, is an underestimate of the physical radius of the neutron star (e.g. London et al., 1984). The latter one was estimated by Özel (2006) to be $13.8 \pm 1.8 \text{ km}$ in EXO 0748-676.

Fig. 4.15 (top) shows the EXOSAT burst wait time distributions together with the XMM-Newton one. While no burst at all was detected with a wait time between ~ 20 min and ~ 2 h neither in 1985 nor in 2003, this gap was partly filled in 1986 by the D2-like bursts with 20–70 min wait times. Fig. 4.15 (bottom) displays the EXOSAT wait time distributions as a function of the persistent 0.1–20 keV flux. There is a global shift of the histograms towards higher wait times as the persistent flux increases. The XMM-Newton wait time distribution, and especially the presence of doublets with ~ 12 min burst separation, is consistent with that obtained by EXOSAT when EXO 0748-676 was in its lowest state in 1985.

These comparisons confirm the above-mentioned dependencies of the LWT bursts properties (shape, spectral characteristics, wait times) on the persistent flux. The presence of SWT bursts could also depend on the persistent flux in the following scheme. At low persistent flux (in the low states of 1985 and in 2003), doublets are emitted with a burst separation of ~ 10 –20 min. Triplets occur in that regime as well. They could have been missed by EXOSAT by chance since the satellite looked at EXO 0748-676 in the low state only 3 times ~ 9 h, while XMM-Newton detected a triplet only once every 20 h. In 1986, the D2-like bursts have longer wait times of ~ 20 –70 min. This could be related to a slightly higher persistent flux then, although the derived fluxes in the low states of 1985, 1986 and 2003 are too close to each other to consider this link as certain. At much larger fluxes (in the intermediate and high states of 1985), there are no bursts with short wait times anymore.

4.6 DISCUSSION

Our findings may be summarized as follows. XMM-Newton observed EXO 0748-676 in a low state 7 times, for an average of 22 h per observation, between September and November 2003. 76 sub-Eddington bursts were detected, either in single, double or triple events, respectively on 33, 14 and 5 occasions. The separation between two events is ~ 3 h while the separation between two bursts in a doublet or a triplet is only ~ 12 min. The primary bursts of different events are similar in terms of duration, peak flux and fluence. Their fluence is strongly correlated with the amount of material accreted before the burst. The profiles of these bursts show an initial fast decay and a second slower decaying component. Quite different are the secondary and tertiary bursts. They have a shorter duration, lower peak flux and lower fluence. Their fluence is not strongly correlated with the (little) amount of material accreted before the burst, except maybe for the tertiaries.

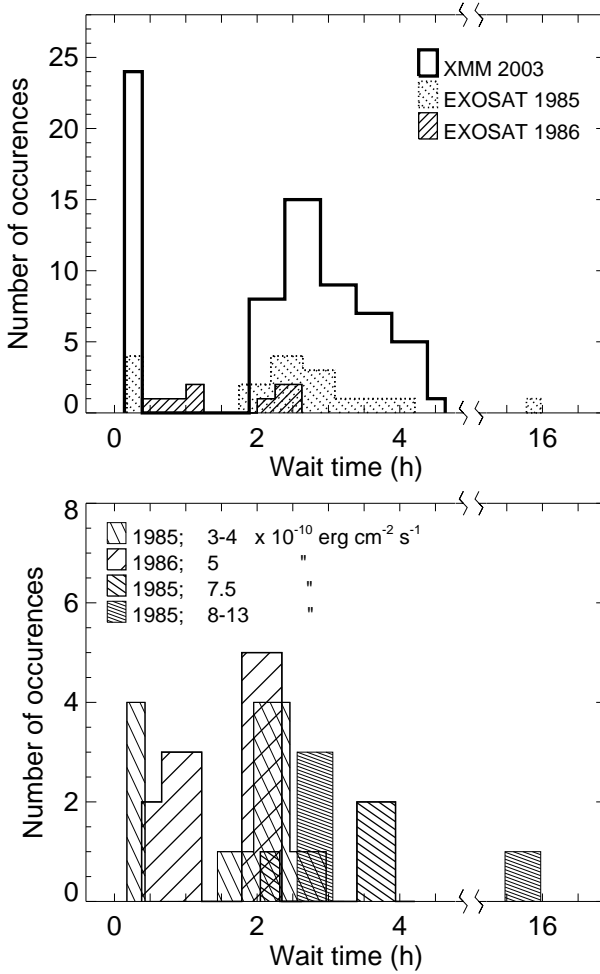


Figure 4.15: *Top*: EXO 0748-676 burst wait time distributions recorded in 1985 and 1986 by EXOSAT (from Table 2 of Gottwald et al. 1986 and Table 1 of Gottwald et al. 1987) and 2003 by XMM-Newton (this chapter). *Bottom*: EXOSAT burst wait time distributions as a function of the persistent 0.1–20 keV flux of EXO 0748-676 indicated in the plot (from Tables 1 and 2 of Gottwald et al. 1986). Note the broken wait time axis in both panels.

The profiles of the secondary and tertiary bursts show only the fast decay and lack the second, more slowly decaying, component seen in the primaries. There is no strong spectral differences between the various burst types. At a given accumulated mass, the total fluence of a triplet is generally larger than that of a doublet which is larger than that of a singlet. For a new event to occur, one has to wait longer after a doublet or a triplet than after a singlet.

4.6.1 Comparison with theory: LWT bursts

How do these results fit within the current theoretical framework? Let us first consider the recurrence times and energetics of the LWT bursts. There are two ways to make bursts (or burst ‘events’) with a recurrence time as short as 3 hours: mixed H/He ignition at an accretion rate close to 10% Eddington, or unstable hydrogen ignition at an accretion rate of $\approx 1\%$ Eddington.

Mixed H/He ignition

The best-studied of these is the first, unstable helium ignition in a hydrogen-rich environment. At high accretion rates, the accumulating fuel layer is hot enough that the hydrogen burns via the beta-limited and thermally stable hot CNO cycle (Hoyle & Fowler, 1965). When the helium ignites, it burns in a hydrogen rich environment, prolonging the nuclear energy release and leads to long burst tails.

The shape of the burst lightcurves from EXO 0748-676 is similar to those observed from GS 1826-24 which Galloway et al. (2004) argued is bursting in this regime. The observed α value supports this interpretation, since the typical energy release $Q_{\text{nuc}} \approx 4$ MeV per nucleon in the rp-process (*e.g.*, Schatz et al. 1999; Table 10 of Woosley et al. 2004) gives an expected α (*e.g.*, Galloway et al., 2004)) close to the observed value $\alpha = 53$:

$$\alpha = \frac{c^2 z}{Q_{\text{nuc}}} \left(\frac{\xi_b}{\xi_p} \right) = 48 \left(\frac{z}{0.31} \right) \left(\frac{4 \text{ MeV}}{Q_{\text{nuc}}} \right) \left(\frac{\xi_p / \xi_b}{1.5} \right)^{-1}, \quad (4.1)$$

where z is the gravitational redshift, and $\xi_{b,p}$ are factors to account for anisotropy in the burst and persistent luminosities. They are defined by $L_{b,p} = 4\pi d^2 \xi_{b,p} f_{b,p}$, where $L_{b,p}$ and $f_{b,p}$ are the intrinsic luminosities and the observed fluxes, and d the distance to the source (Lapidus & Sunyaev, 1985; Fujimoto, 1988)¹. $\xi_{b,p} > 1$ indicates that the observed

¹ We note that anisotropy of the burst luminosity was not included in the analysis by Özel (2006). The EXO 0748-676 neutron star mass and radius determinations in that paper are

flux is lower than it would be in the absence of anisotropy. Here we use the estimates $\xi_b^{-1} = 0.5 + |\cos i|$ and $\xi_p^{-1} = 2 |\cos i|$, obtained by Fujimoto (1988) for a system viewed under inclination i whose geometry enhances the emission in the direction perpendicular to the disk plane, because of scattering in the disk, more strongly when the incident photons come from the inner disk (during persistent emission) than when they come from the neutron star surface (during bursts). Using $i \approx 75\text{--}83^\circ$ for EXO 0748-676 (Parmar et al., 1986) gives $\xi_b \approx 1.3\text{--}1.6$, $\xi_p \approx 1.9\text{--}4.2$, and a ratio $\xi_p/\xi_b \approx 1.5\text{--}2.6$. We note that the $\xi_{b,p}$ estimates could significantly differ if other system geometries (e.g. including disk warping) were assumed.

In multizone X-ray burst simulations of mixed H/He ignition bursts, Woosley et al. (2004) found recurrence times close to 3 hours for accretion of solar metallicity material at $\dot{M} = 1.75 \times 10^{-9} M_\odot \text{ yr}^{-1}$, or luminosity $\dot{M}(GM/R) \approx 2 \times 10^{37} \text{ erg s}^{-1}$ for a $1.4 M_\odot$, 10 km neutron star (models zM and ZM of Woosley et al. 2004). This agrees quite well with the observed X-ray luminosity from EXO 0748-676, once the anisotropy parameter is included. The unabsorbed 0.1–100 keV flux is $8.4 \times 10^{-10} \text{ erg cm}^{-2} \text{ s}^{-1}$, giving for a distance of 5 kpc a luminosity of $L_X = 0.48 \times 10^{37} \text{ erg s}^{-1}$ ($\xi_p/1.9$) and $L_X = 1.9 \times 10^{37} \text{ erg s}^{-1}$ ($\xi_p/1.9$) for a distance of 10 kpc, where we normalize the anisotropy parameter to $i = 75^\circ$. Therefore we find that the recurrence times and α values of the LWT bursts agree well with the models of Woosley et al. (2004), particularly when the anisotropy factor is included.

However, the total energies of the LWT bursts in EXO 0748-676 are somewhat lower than in the models, or than observed for GS 1826-24. In the mixed H/He regime, the ignition column depth is $y_{\text{ign}} \approx 2 \times 10^8 \text{ g cm}^{-2}$ (Cumming & Bildsten, 2000) giving a burst energy $E_{\text{burst}} = 4\pi R^2 Q_{\text{nuc}} y_{\text{ign}} / (1 + z) = 7.4 \times 10^{39} \text{ ergs}$ (assuming complete burning of the whole surface, radius $R = 10 \text{ km}$, and energy release $Q_{\text{nuc}} = 4 \text{ MeV}$). This estimate agrees well with models zM and ZM of Woosley et al. (2004) (see their Table 9) and with the observed burst energies in GS 1826-24 ($5.3 \times 10^{39} \text{ ergs}$ at 6 kpc, Galloway et al. 2004), while the mean burst energy for the LWT bursts in EXO 0748-676 is $(0.5\text{--}2.1) \times 10^{39} \text{ ergs}$ for the distance range 5–10 kpc. Note that anisotropy, which would tend to decrease the burst luminosity for GS 1826-24 (Galloway et al., 2004) and increase it for EXO 0748-676 (Fujimoto, 1988), is not included in these estimates.

likely unaffected by the anisotropy factor, as long as it is constant through the burst, since they come from taking the ratio of the peak flux and the flux in the tail. However, the lower limit on the source distance, $d > 9.2 \pm 1.0 \text{ kpc}$ should be reduced by a factor $\xi_b^{1/2}$, or 15–30%, giving $d > 7.3\text{--}8.1 \text{ kpc}$ for $\xi_b = 1.3\text{--}1.6$, using the estimate of Fujimoto (1988).

The same is true for the peak luminosity. The high base temperatures $\gtrsim 10^9$ K reached in mixed H/He bursts give a peak luminosity $\gtrsim 10^{38}$ erg s $^{-1}$ (e.g., Woosley et al., 2004), approaching the Eddington luminosity. Ignoring anisotropy, in GS 1826-24, the bursts peak flux was 3×10^{-8} erg cm $^{-2}$ s $^{-1}$, giving $L_{\text{peak}} = 1.3 \times 10^{38}$ erg s $^{-1}$ at 6 kpc (Galloway et al., 2004). In contrast the mean peak flux for the LWT bursts in EXO 0748-676 is 7.2×10^{-9} ergs cm $^{-2}$ s $^{-1}$, giving $L_{\text{peak}} = (0.22\text{--}0.86) \times 10^{38}$ erg s $^{-1}$ for the distance range 5–10 kpc. Independent of the assumed distance, it is a factor of 7 below the peak flux of the bright radius expansion burst observed by Wolff et al. (2005) from EXO 0748-676, further showing that these LWT bursts are faint relative to the Eddington luminosity.

Hydrogen ignition

The low burst energies and peak luminosities suggest a different explanation for the LWT bursts from EXO 0748-676, that they are triggered by unstable hydrogen ignition. Hydrogen burning is unstable for temperatures less than $\approx 8 \times 10^7$ K, when the CNO is no longer beta-limited, and can trigger thermonuclear flashes (Fujimoto et al., 1981).

Bildsten (1998) estimates that unstable hydrogen ignition occurs for accretion rates $\dot{M} \lesssim 2 \times 10^{-10} M_{\odot} \text{ yr}^{-1}$, or luminosities $L_X \lesssim 2 \times 10^{36}$ erg s $^{-1}$. This matches the luminosity of EXO 0748-676 if the source is located at the closer end of its distance range, and the anisotropy factor is small. The observed recurrence time of ≈ 3 hours matches the recurrence time expected close to the transition between unstable and stable hydrogen burning. The maximum temperature at which hydrogen can unstably ignite, close to 8×10^7 K, corresponds to a column depth of approximately 10^7 g cm $^{-2}$ (see Fig. 1 of Cumming 2004). At an accretion rate of 1% of the Eddington rate, this column is accreted in 3.2 hours.

There are two possible outcomes of unstable hydrogen ignition (Fujimoto et al., 1981; Peng et al., 2007). If the hydrogen ignition depth is $\gtrsim 5 \times 10^7$ g cm $^{-2}$, the minimum column depth at which helium can ignite (Fig. 1 of Cumming 2004), the increase in temperature following hydrogen ignition triggers ignition of helium by the triple alpha reaction, and a mixed hydrogen/helium flash occurs. At smaller ignition depths, which occur near the transition between unstable and stable hydrogen burning, the hydrogen flash is not able to trigger helium ignition. This case has recently been modeled by Peng et al. (2007). They include, for the first time, sedimentation of heavy elements in the accumulating fuel layer. For an accretion rate close to 1% of the Eddington

rate, they find that the hydrogen flash reaches a peak luminosity of 5 times the accretion luminosity, or $\approx 0.1 \times 10^{38} \text{ erg s}^{-1}$. This is lower than the observed peak luminosities of the LWT bursts by a factor of a few. Burning a column depth of 10^7 g cm^{-2} of hydrogen to helium gives an expected burst energy $0.6 \times 10^{39} \text{ ergs}$ (using the energy release $Q_{\text{nuc}} = 6.0 \times 10^{18} \text{ erg g}^{-1}$ appropriate for the hot CNO cycle). This is within the range of observed energy for the LWT bursts.

Although the peak luminosity found by Peng et al. (2007) is a little lower than observed for the LWT bursts, they only computed a few different cases of hydrogen ignition. In addition, the recurrence time and burst energies do match the expectations for hydrogen ignition close to the stability boundary quite well. An interesting point about this interpretation is that the sedimentation of heavy elements plays a crucial role (Peng et al., 2007). Without sedimentation, the CNO abundance remains close to the solar value at the ignition depth, and the energy released by the initial proton captures is small giving a very weak flash. With sedimentation, the CNO abundance is enhanced by a factor of several, leading to more energy release during the initial runaway, giving a peak temperature of $\approx 3 \times 10^8 \text{ K}$ and a peak luminosity observable above the accretion luminosity.

In addition, the interpretation of the LWT bursts as hydrogen flashes also provides two explanations for the bright energetic burst ($E_b = 3.6 \times 10^{-7} \text{ erg cm}^{-2}$) reported by Wolff et al. (2005) from EXO 0748-676 at a low persistent flux ($f_p = 4.8 \times 10^{-10} \text{ erg cm}^{-2} \text{ s}^{-1}$). First, if the hydrogen flash fails to ignite helium, a pure helium layer builds up beneath the hydrogen burning shell which will eventually ignite by triple alpha reactions. Alternatively, since the burst properties indicate that the hydrogen ignition is occurring close to the transition between unstable and stable hydrogen burning, a slight increase in accretion rate would lead to stable hydrogen burning and a similar accumulation of a pure helium layer. Second, if the accretion rate drops, the hydrogen ignition column depth becomes large enough to trigger helium ignition resulting in a mixed H/He flash. Wolff et al. (2005) derive a burst fluence of $3.6 \times 10^{-7} \text{ erg cm}^{-2}$ which translates to a burst energy of $(1.5\text{--}2.5) \times 10^{39} \text{ ergs}$ (depending on whether the peak luminosity corresponds to the Eddington limit for solar composition or for pure helium; the corresponding distances are 5.9 and 7.7 kpc). Assuming $Q_{\text{nuc}} = 1.6 \text{ MeV}$, appropriate for helium burning to iron group, the implied thickness of the fuel layer is $\approx 10^8 \text{ g cm}^{-2}$. A pure helium layer accumulating beneath the hydrogen shell would typically reach much greater thicknesses before igniting. Therefore, it seems likely that the Wolff et al. (2005) burst is another example of a hydrogen ignition, but this time also igniting the helium.

4.6.2 *Comparison with theory: SWT bursts*

We have spent some time discussing the origins of the LWT bursts in the hope that this might give a clue to the origin of the SWT bursts. These have so far evaded theoretical explanation, although possibilities have been put forward in the literature. Fujimoto et al. (1987) suggested that unburned fuel left over from the preceding burst is mixed downwards by hydrodynamic instabilities driven by rotational shear. Wallace & Woosley (1984) suggested that fresh fuel could be mixed downwards by Rayleigh-Taylor instabilities which set in as the layer cools. However, neither of these explanations offers a natural explanation for the ten minute delay time. This point is emphasized dramatically by the discovery of burst triplets discussed in this chapter. The fact that the same characteristic timescale sets the delay between the second and third bursts in a triplet as well as the first and second points to some physical process with this timescale that can recur more than once in succession.

Mixed H/He bursts at accretion rates close to 0.1 of the Eddington rate have been modeled extensively in spherical symmetry with large nuclear reaction networks (Woosley et al. 2004). However, there has been little work on hydrogen triggered bursts, and so the suggestion that the LWT bursts are hydrogen triggered opens up the possibility that the ten minute phenomenon is connected with unstable hydrogen burning. For example, the half-life of ^{13}N in the CNO cycle is 9.97 minutes, very close to the observed timescale. Perhaps as the layer cools following the initial flash, an instability driven by proton captures on ^{13}C or ^{14}N occurs once there has been time for enough seed nuclei to be produced by the beta-decay of ^{13}N . However, it is not clear how the fact that the timescale between SWT bursts changes (see Sect. 4.5), possibly with accretion rate, would be accommodated in this picture. Further theoretical studies of hydrogen triggered bursts are needed to explore the possibility that the SWT bursting has a nuclear physics explanation.

Even without a good picture of the physics of the SWT bursts, we can explore some possibilities by considering the idea that the second and third bursts are caused by ignition of leftover fuel from the first burst. One way that this might happen is that the ignition conditions for the first burst are always the same, but that sometimes incomplete burning occurs, leaving behind unburned fuel that later reignites leading to double or triple events. However, this is inconsistent with the observation that, at a given wait time, the fluence is the same for a D1, a T1 or a S1 burst (the LWT bursts have all the same alpha values). In addition, the fact that the wait time to the next event is longer after a

double or triple (regardless of the type of the next event) also suggests a different picture. Imagine that after the first burst (either S₁, D₁, or T₁), a fraction f of the fuel layer is left unburned. Then, in double or triple events, this leftover fuel layer is burned after a delay time of ≈ 10 minutes, whereas in single events, the unburned fuel survives, and leads to early ignition of the next event. The difference between singles and doubles/triples here is not whether there is any unburned fuel, but instead whether the unburned fuel is able to ignite on the ten minute timescale.

One way to test this idea is to look for consistency between the wait times and the burst fluences. The wait time after a double (triple) is $\approx 37\%$ (55%) longer than the wait time after a single, suggesting that a fraction $f_a \approx 37\%$ (55%) of the available accreted fuel is not burned during the first burst. If this unburned fuel was of the same composition as the rest of the layer and burned subsequently in the second/third bursts, we would expect the double/triple events to have a larger fluence by the same factor f_a . Now, the double (triple) events have larger fluences than the singles, but only by a factor f_b of $\approx 17\%$ (25%). This indicates that the layer that burns in the second/third bursts has a lower energy per gram, for example a smaller hydrogen content than the accreted fuel that burns in the first burst. This suggests that in fact the ‘unburned’ fuel layer undergoes some hydrogen burning into helium during the first burst. Interestingly, the ratio f_a/f_b is ≈ 2.2 for both the doubles and the triples and is $\lesssim 2.5$ which is the value of the ratio between the energy released by an hydrogen nucleon burning to the iron group (4 MeV) and the energy released by an helium nucleon burning to the iron group (1.6 MeV). The burst lightcurves also support the idea that the second/third bursts have a smaller hydrogen fraction since they have a much shorter tail than the first bursts.

These properties would be naturally explained if the first burst in the sequence involved unstable hydrogen burning into helium. If hydrogen ignition is occurring near the transition from unstable to stable hydrogen burning, then it is not clear whether helium is burning at all in the first flash. Certainly, it is not able to ignite unstably at low column depths but maybe it burns slightly at the peak temperature. The first flash would thus leave a large part (if not all) of the available helium unburned and further produce some. A subsequent second/third burst would take place in an helium-rich environment. The fact that little material can be accreted within ten minutes suggests that the SWT bursts are also hydrogen triggered since lower column depths are required than for helium ignition. More theoretical work on hydrogen ignition bursts is needed to test these ideas.

One important question concerns the occurrence rate of quadruple events. We did not observe a quadruple burst from EXO 0748-676. Galloway et al. (2006) report one quadruple event from 4U 1636-536 in the RXTE burst catalog. The occurrence rate of quadruple versus triple events (as well as triple versus double events) could provide an important constraint on theoretical models.

CONCLUSION

This is the first time that unambiguously and repeatedly triple bursts are detected in an accreting neutron star, EXO 0748-676. The source was already known to frequently exhibit double bursts, where two bursts are separated by only 12 minutes. Now the same time scale is seen in triple bursts. This recurrence time is too short to accrete a sufficient amount of fuel, which indicates that there must have been fuel left unburned in the previous burst. We suggest that after each burst there is an amount of fuel left unburned, which may or may not reignite after 12 minutes, in the former case producing a double or triple burst. We find evidence that this unburned fuel yields less energy per gram, pointing to a lower hydrogen content than for the fuel of the primary bursts.

The recurrence times of 3 hours and the low α values are consistent with mixed hydrogen/helium burning at 0.1 Eddington, as seen for example in GS 1826-24. The persistent luminosity of EXO 0748-676 is consistent with this accretion rate if the X-ray emission from the system is anisotropic, as predicted for large inclination angles. However, the expected energies and peak luminosities are somewhat larger than observed in EXO 0748-676. In addition, this burning regime has been well-studied theoretically and does not predict the ten minute bursting phenomenon. New physics, such as mixing of fuel to deeper layers, is required to explain the multiple events within the mixed hydrogen/helium burning regime.

Hydrogen ignition at a lower accretion rate may provide a more natural explanation for the burst behavior of EXO 0748-676. Hydrogen ignition bursts are not well-studied, but the properties of the bursts from EXO 0748-676 agree quite well with the recent work by Peng et al. (2007). In particular, the low peak luminosity and burst energies of the LWT bursts, and the low persistent luminosity are consistent with burning in this regime. This opens up the exciting possibility that the ten minute recurrence time bursts are in fact a natural consequence of hydrogen ignition bursts.

4.A LIGHT CURVES & BURSTS LIST

Fig. 4.16 shows the EPIC PN light curves of EXO 0748-676 with a binning of 60 s during XMM-Newton revolutions 692 to 719. Panels a and b show the 5–10 keV and the 0.3–5 keV energy band, respectively. Panel c shows the hardness ratio. Times are not barycenter-corrected. A cycle number tracing the eclipse timing is indicated on the top axis. This was determined from a reference time of 13.79 h on 2003 September 19 (or XMM-Newton time of 1.8036643×10^8 s) estimated as the mid-time of the first eclipse observed during revolution 692, and using an orbital period of 3.824 hr (Wolff et al., 2002). Integer values of the cycle number correspond to phase 0, or estimated eclipse mid-times.

The peak time, wait time and type of all the bursts are listed in Table 4.7. Since the wait time of the first burst of each observation in the series cannot be determined, a lower limit is given as the separation between the burst peak time and the start time of the observation. An upper limit is given as the separation between the burst peak time and peak time of the last burst observed during the previous observation of the series.

We note that because of scattering, residual emission is present during eclipses at a level of $\sim 4\%$ of the source's persistent flux. This explains why an X-ray burst was once detected during an eclipse with EXOSAT (Gottwald et al., 1986). This implies that any S1, D1 or T1 (ie. strong) burst occurring during an eclipse of the XMM-Newton observation would have been detected. Since we do not detect any burst during eclipses, it appears unlikely that we have missed an S1, D1 or T1 burst because of eclipses. Furthermore, since an eclipse lasts ~ 500 s, which is less than the typical separation of the bursts in a multiple burst event, it is not possible either to have missed a complete doublet or triplet. From the inspection of Fig. 4.16, we can therefore conclude that it is unlikely that any S1, D1, T1, D2, T2 or T3 burst has been missed because of an eclipse.

However, bursts occurring close to (less than 25 min) the beginning or the end of an observation, or close to a short instrumental gap such as occasionally present in the data, cannot have their type determined certainly because another burst of the same event could have occurred during the gap and been missed. In such cases, the different possible types are indicated in Table 4.7 starting with the one attributed to the burst in this analysis.

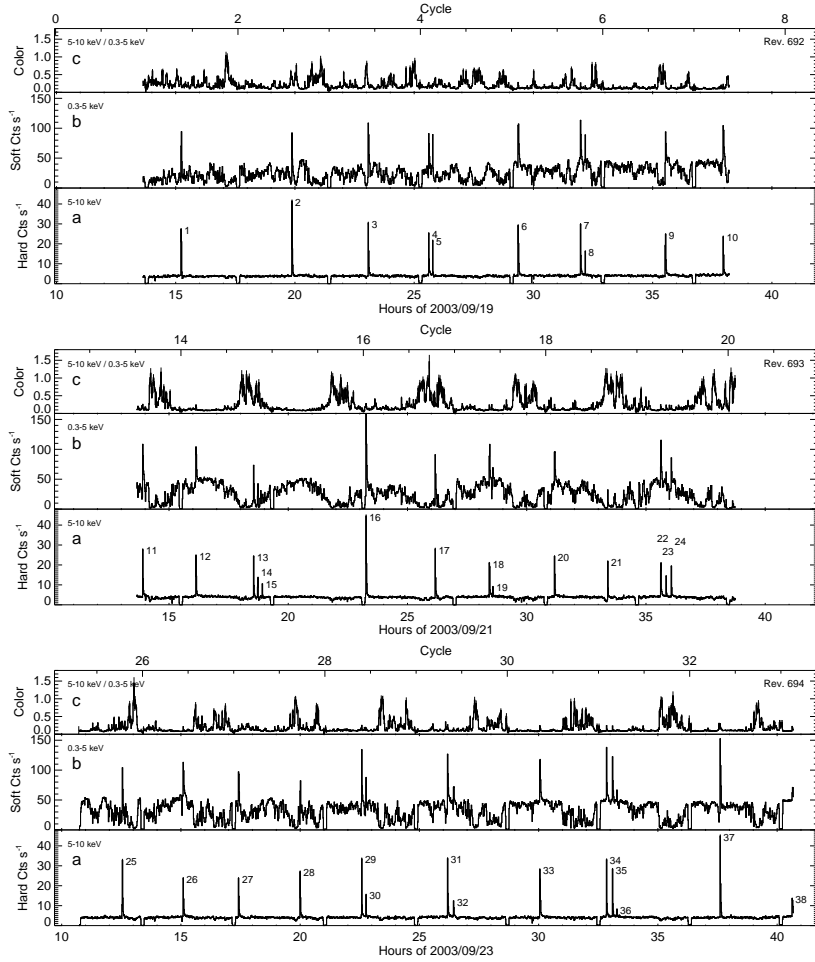


Figure 4.16: EXO 0748-676 as observed by XMM-Newton EPIC PN during revolutions 692 (*top*), 693 (*middle*) and 694 (*bottom*). **a)** 5–10 keV light curve. The bursts are numbered. **b)** 0.3–5 keV light curve. **c)** Color (counts in the 5–10 keV band divided by counts in the 0.3–5 keV band) as a function of time. The binning time is 60 s in each panel. The cycle number is indicated on the top axis, with the estimated mid-eclipse time of the first eclipse observed during revolution 692 taken as cycle number 1.

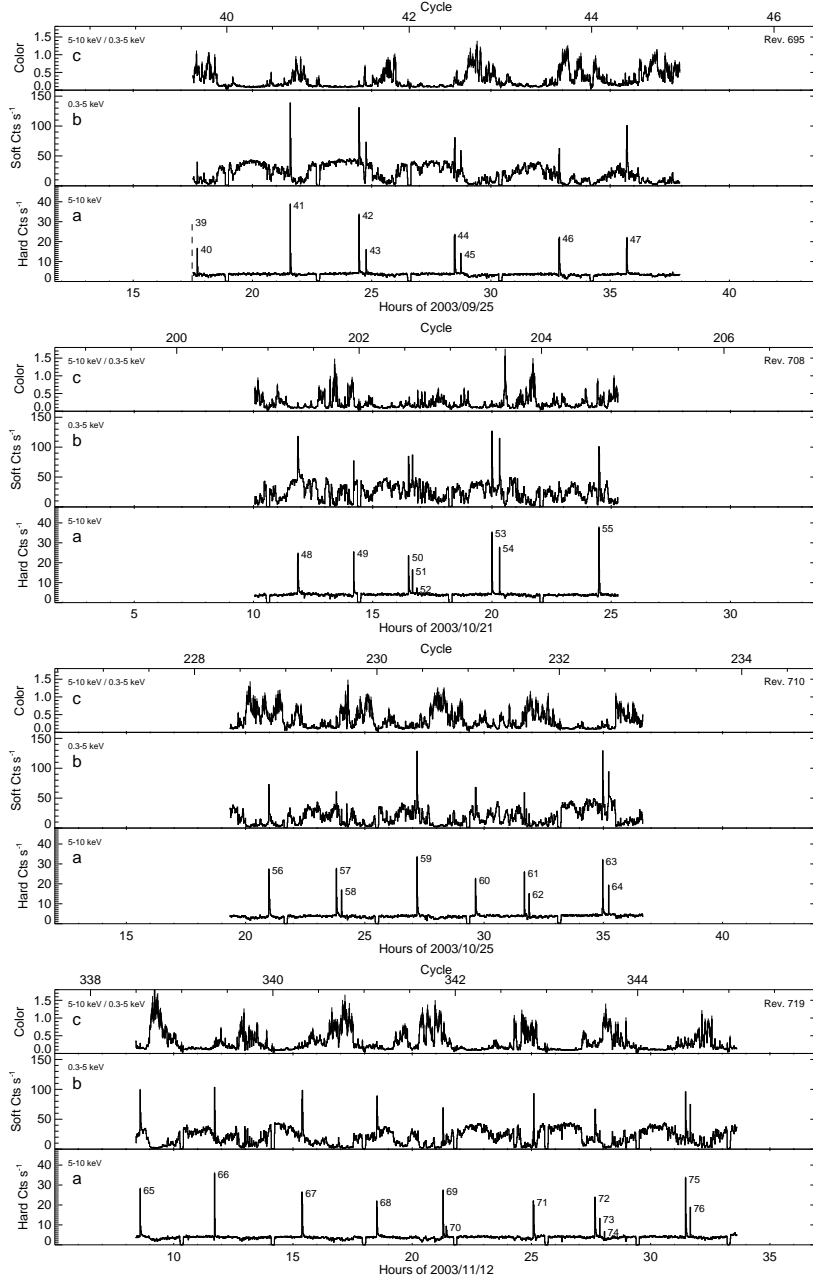


Figure 4.16: Continued for, from top to bottom, XMM-Newton revolutions 695, 708, 710 and 719. The dashed line in panel c of the top plot indicates the time of a burst (numbered 39) detected by RGS just before the start of the EPIC PN observation.

Table 4.7: Bursts timing. The columns indicate the burst number, the XMM-Newton revolution number at which the burst occurred, the burst peak time determined from the EPIC PN 5–10 keV 1 s resolution light curve (except for burst 39 detected only by RGS), the wait time and the burst type. S means single burst. D1 and D2 mean first and second burst in a doublet. T1, T2 and T3 mean first, second and third burst in a triplet, respectively. When the burst type cannot be determined certainly, we indicate the different possible types, starting with the one attributed to the burst in this analysis.

Burst	Rev.	Peak time (UT)	t_{wait} (h)	Type
1	692	Sep 19 15:13:58	1.62 <	S1
2		19:52:12	4.64	S1
3		23:04:31	3.21	S1
4		20 01:36:43	2.54	D1 (T2)
5		01:46:28	0.162	D2 (T3)
6		05:21:42	3.59	S1 (D2)
7		07:58:35	2.61	D1
8		08:10:17	0.195	D2
9		11:31:58	3.36	S1
10		13:57:49	2.43	S1 (D1, T1)
11	693	21 13:53:56	0.259 <	S1 (D2, T3)
12		16:08:03	2.24	S1
13		18:32:55	2.41	T1
14		18:43:22	0.174	T2
15		18:55:05	0.195	T3
16		23:15:33	4.34	S1 (D2)
17		22 02:09:52	2.91	S1
18		04:26:17	2.27	D1
19		04:35:11	0.148	D2
20		07:10:07	2.58	S1 (D2)
21		09:23:54	2.23	S1
22		11:37:24	2.23	T1
23		11:51:07	0.229	T2
24		12:04:08	0.217	T3
25	694	23 12:32:29	1.83 <	S1
26		15:05:56	2.56	S1
27		17:25:09	2.32	S1 (D2)
28		20:00:08	2.58	S1
29		22:34:36	2.57	D1
30		22:45:51	0.187	D2
31		24 02:10:45	3.41	D1
32		02:26:15	0.259	D2

Continued on next page

Table 4.7 continued

33		06:03:06	3.61	S1
34		08:50:34	2.79	T1
35		09:05:55	0.256	T2
36		09:16:31	0.177	T3
37		13:36:43	4.34	S1
38		16:37:55	3.02	S1 (D1, T1)
^a 39	695	2517:28:20	0.036 < < 24.8	D1 (T2)
40		17:41:31	0.220	D2 (T3)
41		21:34:54	3.89	S1
42		2600:28:00	2.89	D1
43		00:46:20	0.306	D2
44		04:28:35	3.70	D1
45		04:44:35	0.267	D2
46		08:51:35	4.12	S1
47		11:41:43	2.84	S1
48	708 Oct 21	11:51:35	1.82 < < 600	S1 (D1)
49		14:12:10	2.34	S1 (D1)
50		16:30:24	2.30	T1
51		16:39:49	0.157	T2
52		16:51:05	0.188	T3
53		19:59:49	3.15	D1
54		20:18:52	0.317	D2
55		2200:28:46	4.17	S1
56	710	2520:58:42	1.65 < < 92.5	S1
57		23:48:23	2.83	D1
58		2600:01:37	0.221	D2
59		03:11:08	3.16	S1 (D1)
60		05:38:40	2.46	S1 (D2)
61		07:41:16	2.04	D1
62		07:53:28	0.203	D2
63		10:58:02	3.08	D1
64		11:13:05	0.251	D2
65	719 Nov 12	08:35:44	0.191 < < 405	S1 (D2, T3)
66		11:42:47	3.12	S1
67		15:23:00	3.67	S1
68		18:31:01	3.13	S1
69		21:17:46	2.78	D1
70		21:26:09	0.140	D2
71		1301:04:58	3.65	S1
72		03:39:57	2.58	T1
73		03:51:47	0.197	T2
74		04:03:36	0.197	T3
75		07:27:43	3.40	D1
76		07:39:37	0.198	D2

^a detected by RGS only, before EPIC cameras were turned on.

THE EFFECT OF ROTATION ON THE STABILITY OF NUCLEAR BURNING IN ACCRETING NEUTRON STARS

L. Keek, N. Langer and J. J. M. in 't Zand

To be submitted for publication.

ABSTRACT Hydrogen and/or helium accreted by a neutron star from a binary companion may undergo thermonuclear fusion. At different mass accretion rates different burning regimes are discerned. Theoretical models predict helium fusion to proceed as a thermonuclear runaway for accretion rates below the Eddington limit and as stable burning above this limit. Observations, however, place the boundary close to 10% of the Eddington limit. We study the effect of rotationally induced transport processes on the stability of helium burning. For the first time detailed calculations of thin helium shell burning on neutron stars are performed using a hydrodynamic stellar evolution code including rotation and rotationally induced magnetic fields. We find that in most cases the instabilities from the magnetic field provide the dominant contribution to the chemical mixing, while Eddington-Sweet circulation becomes important at high rotation rates. As helium is diffused to greater depths, the stability of the burning is increased, such that the critical accretion rate for stable helium burning is found to be lower. Combined with a higher heat flux from the crust, as suggested by recent studies, turbulent mixing could explain the observed critical accretion rate. Furthermore, close to this boundary we find oscillatory burning, which previous studies have linked to mHz QPOs. In models where we continuously lower the heat flux from the crust, the period of the oscillations increases by up to several tens of percents, similar to the observed frequency drift, suggesting that this drift could be caused by cooling of a deeper layer.

5.1 INTRODUCTION

Neutron stars in low-mass X-ray binaries (LMXBs) accrete matter from a companion star through Roche-lobe overflow. Due to conservation of angular momentum, the matter forms a disk around the neutron star, where it radiates away a large fraction of the potential energy

before reaching the neutron star surface. The companion is typically a main sequence star, donating matter with a large hydrogen abundance. For a number of systems which likely have a white dwarf companion, hydrogen may be deficient but helium not (in 't Zand et al. 2005).

The accreted matter is thought to quickly spread over the neutron star surface, forming a thin layer. When this layer is a few meters thick, the temperature and density at the base of the layer reach the ignition conditions for hydrogen and helium fusion. The thermonuclear burning can proceed in a stable or an unstable manner, depending on the temperature dependence of the burning and cooling rates, which depend on the conditions in the thin burning shell. These conditions are largely set by the mass accretion rate (Fujimoto et al. 1981; see also Bildsten 1998). Models predict that hydrogen burning via the CNO cycle is stable for $\dot{M} \gtrsim 10^{-2} \dot{M}_{\text{Edd}}$, while it is unstable for lower accretion rates (assuming a neutron star mass of $1.4 M_{\odot}$ with a 10 km radius, a hydrogen mass fraction $X = 0.7$ and a CNO mass fraction $Z_{\text{CNO}} = 0.01$; \dot{M}_{Edd} is the critical accretion rate where the accretion luminosity equals the Eddington luminosity). For helium burning via the triple-alpha process, theory places the critical accretion rate at the Eddington limit $\dot{M} \simeq \dot{M}_{\text{Edd}}$ (Fujimoto et al. 1981; Ayasli & Joss 1982), which suggests that stable helium burning does not take place in practice. If the accreted matter is hydrogen-deficient, the transition is expected to take place at an even higher accretion rate due to the lack of heating by stable hydrogen burning: $\dot{M} \simeq 10 \dot{M}_{\text{Edd}}$ (Bildsten 1998).

Nevertheless, there are observational indications that stable helium burning takes place at lower accretion rates. Van Paradijs et al. (1988) observe from ten sources, most of which are thought to accrete hydrogen-rich material, that the fraction of hydrogen and helium that is burned in a stable manner increases strongly with the mass accretion rate, while no bursts are observed at accretion rates of $\dot{M} \gtrsim 0.3 \dot{M}_{\text{Edd}}$. Cornelisse et al. (2003) find for 4U 1820-30, which likely has a hydrogen-deficient mass donor, that the burst rate is lower by a factor of 5 for $\dot{M} \gtrsim 0.07 \dot{M}_{\text{Edd}}$ than for lower mass accretion rates, while no bursts are observed at $\dot{M} \gtrsim 0.14 \dot{M}_{\text{Edd}}$. Therefore, the transition of unstable to stable burning likely takes place within several tens of percents of $0.1 \dot{M}_{\text{Edd}}$.

A possible solution is the inclusion of mixing processes. If hydrogen and/or helium are mixed to larger depths, where temperature and density are higher, the conditions under which the fuel ignites are different. An efficient source of mixing are rotationally induced hydrodynamic instabilities (Fujimoto 1993). Yoon et al. (2004a) studied the effect of rotational mixing processes on thin shell burning in accreting white dwarfs and found burning to proceed more stably. Piro

& Bildsten (2007) calculated the effect of turbulent mixing in neutron stars, including mixing due to rotationally induced magnetic fields (Spruit 2002). They find that the magnetic fields are the main driver of the mixing processes. Relatively simple numerical models of helium accretion onto an iron layer show that rotationally induced mixing allows in the case of unstable burning for lower recurrence times for flashes of 5–30 minutes. Furthermore, the models including mixing allow for steady-state burning at accretion rates below \dot{M}_{Edd} . Analytically the dependence of \dot{M}_{st} , the accretion rate at the transition between (un)stable burning, on the rotation rate of the neutron star, Ω , is derived as $\dot{M}_{\text{st}} \propto \Omega^{0.62}$. For neutron stars that rotate slower than 10% of the Keplerian velocity at the surface, Piro & Bildsten (2007) find increased stability: $0.25 \dot{M}_{\text{Edd}} \lesssim \dot{M}_{\text{st}} \lesssim \dot{M}_{\text{Edd}}$.

In this chapter we present the results of detailed numerical simulations to study this effect. We use a one-dimensional multi-zone model of the outer layers of a neutron star to study the nuclear burning of accreted helium. We introduce both rotation and magnetic fields in the model and investigate the stability of the burning as a function of the mass accretion rate, the rotation rate of the neutron star core and the heat flux emanating from the crust.

5.2 METHOD

To model the outer layers of the neutron star we employ a stellar evolution code that is a modified version of the code used by Yoon et al. (2004a) to model nuclear burning of helium shells in white dwarfs. It implicitly solves the stellar structure equations on a one-dimensional grid consisting of a series of mass shells. The effect of the centrifugal force on the stellar structure is taken into account. Consequently, the mass shells are isobars rather than spherical shells (cf. Heger et al. 2000). An extensive nuclear network consisting of 35 isotopes and 65 nuclear reactions is employed to model the chemical evolution. The effects of rotation on the chemical mixing and the transport of angular momentum are calculated. The effects of a rotationally induced magnetic field on the mixing of angular momentum and chemical species is calculated as well (Spruit 2002). Convection is taken into account using the Ledoux criterion.

We consider the accretion of matter which is hydrogen-deficient, but which has a large (99%) helium content. This allows us to study the stability of helium shell burning without the complication of the nuclear processes involving hydrogen. We will discuss the potential effect of the inclusion of hydrogen on our results.

Relativistic effects are not considered during the simulation, since they are small in the thin helium burning shell. The effect of general relativity on observables, such as the luminosity and mass accretion rate, can be taken into account with appropriate gravitational redshift factors (e.g. Woosley et al. 2004), reducing the values for the observables typically by several tens of percents. We do not apply these corrections to our results, as we are primarily interested in the relative effect of rotationally induced mixing on the stability of shell burning.

5.2.1 *Grid*

The one-dimensional grid divides the star in shells with a certain mass and is separated in two parts to facilitate matter accretion while limiting numerical noise in the nuclear burning region. In the inner, Lagrangian part each shell is assigned an absolute amount of mass, while in the outer so-called pseudo-Lagrangian part a shell is assigned an amount of mass relative to the total mass in the model. To minimize numerical diffusion, we choose these regions such that the nuclear burning takes place in the Lagrangian part. After each time step the grid is adjusted to ensure that any gradients in for instance temperature, energy generation rate or chemical composition are well resolved.

Apart from the different grid points our model has the notion of a ‘core’, which represents the inner part of the star that is not modeled in detail and which sets the inner boundary conditions of our grid. The core has a mass, radius, rotation rate and a luminosity. These quantities are kept at fixed values. During consecutive time steps angular momentum is exchanged between the grid and the core, after which we return the angular momentum and velocity of the core to the initial values, effectively preventing the core to spin up or down. We can safely make this approximation, since the amount of angular momentum that is accreted on the timescale of nuclear burning is negligible with respect to the angular momentum of the core.

5.2.2 *Accretion*

Mass accretion is implemented by increasing the total amount of mass and scaling the mass of the grid points in the pseudo-Lagrangian region. The mass fractions of the isotopes at each of these grid points are set to the weighted mean of the original composition of the grid point and the assumed composition of the accreted matter, where we weigh by, respectively, the original mass of the grid point and the accreted mass that is added to the grid point.

The accreted matter originally carries angular momentum corresponding to orbital motion at the Keplerian angular velocity at the surface of $\Omega_K = \sqrt{GMR^{-3}}$, where M and R are the mass and radius of the star, respectively. We assume, however, that the angular momentum of the accreted material is quickly shared with a number of the outermost grid points. This region coincides with or is slightly smaller than the pseudo-Lagrangian region where the mass is added. The distribution of the angular momentum is done such that the specific angular momentum is constant in the outer region. After the accreted angular momentum is added to the model, the mixing of angular momentum resulting from the different viscous processes is applied to the model. As in the treatment of the accretion of mass, we make sure that the region where angular momentum is accreted lies outside the region of interest, i.e. well above the helium burning shell.

5.2.3 *Diffusivity and viscosity*

Due to the accretion of angular momentum, the outer layers of the star spin faster than the core. Therefore a non-zero shear q is present

$$q = \frac{d \ln \Omega}{d \ln r}, \quad (5.1)$$

where r is the radial coordinate. The shear can give rise to hydrodynamical instabilities. We consider the dynamical shear instability, the secular shear and the Solberg-Høiland instability as well as Eddington-Sweet circulation (e.g., Heger et al. 2000, Talon 2004). Furthermore, we consider the presence of a rotationally induced magnetic field.

A magnetic field is employed following the prescription of the ‘Taylor-Spruit dynamo’ presented by Spruit (2002). A small initial radial magnetic field B_r winds up due to the shear to create a much stronger toroidal field B_ϕ . The field growth is limited by magnetohydrodynamic (MHD) instabilities. In this process B_r is increased as well, such that once an equilibrium situation is reached, the initial field strength B_r is unimportant. Equilibrium is reached on much shorter timescales than the mixing processes induced by the magnetic field. Therefore, in our model we employ the equilibrium values for B_r and B_ϕ .

Both the magnetic and non-magnetic hydrodynamic instabilities cause turbulence which allows for chemical mixing and the transport of angular momentum. Furthermore, angular momentum is transported as well due to magnetic torques. We treat the chemical and angular

momentum mixing as diffusion processes. Transfer of angular momentum is governed by the one-dimensional diffusion equation

$$\frac{d\Omega}{dt} = \frac{1}{\rho r^4} \frac{d}{dr} \left(\rho r^4 \nu \frac{\partial \Omega}{\partial r} \right), \quad (5.2)$$

with ν the viscosity and ρ the density. Diffusion of the mass fraction Y of a given isotope, e.g. ${}^4\text{He}$, is calculated via

$$\frac{dY}{dt} = \frac{1}{\rho r^2} \frac{d}{dr} \left(\rho r^2 D \frac{\partial Y}{\partial r} \right), \quad (5.3)$$

where D is the diffusivity. D and ν are measures for the efficiency of the respective diffusion processes. D is generally smaller than ν , since it requires more work to exchange material than to exchange angular momentum. For the non-magnetic instabilities we use $\nu = 30D$ (Chaboyer & Zahn 1992). This is not the case for the D and ν that follow from the Tayler-Spruit mechanism, where angular momentum is transported due to magnetic torques, such that D and ν differ in their dependencies on q and Ω .

5.2.4 Initial model

We start with a grid of approximately 600 grid points that represent the outer layers of the neutron star from a column depth of $y \simeq 1 \text{ g cm}^2$ down to $y \simeq 10^{11} \text{ g cm}^2$, with a total mass of $\simeq 10^{24} \text{ g}$. As initial composition we take 50% ${}^{12}\text{C}$ and 50% ${}^{16}\text{O}$. This acts as a buffer which is inert with respect to the triple-alpha reactions of helium burning. On this grid matter is accreted with a composition of 99% ${}^4\text{He}$ and 1% other isotopes, based on the equilibrium mass fractions of the CNO cycle.

We use a core with a mass of $M = 1.44 M_{\odot}$ and a radius $R = 10 \text{ km}$ for a canonical neutron star. The angular velocity of the core, Ω , is expressed in units of the Keplerian angular velocity at the surface: $\Omega_K = 1.4 \cdot 10^4 \text{ radians s}^{-1}$. We create models with different values for Ω .

The heat flux from the neutron star crust is modeled by setting the luminosity at the inner boundary of our grid to a fixed value L_{crust} .

We disable the energy output of the ${}^{12}\text{C} + {}^{12}\text{C}$ and ${}^{12}\text{C} + {}^{16}\text{O}$ reactions to prevent the occurrence of unstable carbon burning. Any heating that stable carbon may have provided can be modeled as an extra contribution to L_{crust} .

5.2.5 Flux from the crust

As the ignition of the accreted helium depends strongly on the temperature and we do not consider heating by stable hydrogen burning, it is influenced by L_{crust} . The crust is a deeper layer of the neutron star starting at $y \simeq 10^{12} \text{ g cm}^{-2}$ and extending down to the core where densities exceed the nuclear density. When matter is accreted onto the neutron star, the crust is compressed. This gives rise to pycnonuclear burning and electron-capture reactions which heat both the neutron star core as well as the outer layers. Therefore, this heat flux is generally assumed to scale with the accretion rate and a fixed energy generated per accreted nucleon is applied. Previous studies often use 0.15 MeV/nucleon (Haensel & Zdunik 2003). Cumming et al. (2006) use values in the range of $0.1\text{--}0.3 \text{ MeV/nucleon}$ when studying the ignition conditions of long duration type I X-ray bursts. The analysis of the superburst from 4U 1608-52 (Keek et al. 2008) indicates that the temperature of the crust was likely much higher than predicted by current models. Recently Gupta et al. (2007) calculated the thermal structure of the crust, for the first time including electron captures into excited states, finding a heat flux from the crust up to ten times higher than obtained in previous studies. It is clear that the value of the heat flux from the crust is still not well understood. Therefore, we choose to vary it independently from the mass accretion rate.

5.3 RESULTS

5.3.1 Turbulent mixing

The accretion of angular momentum gives rise to shear, which causes turbulence and induces a magnetic field. These drive the transport of angular momentum and the mixing of the chemical composition. In turn, the chemical and angular velocity profiles influence the diffusivity and viscosity, until an equilibrium is reached. We present the properties of equilibrium models with different rotation rates of the core and different mass accretion rates. The heat flux from the crust is set to a value such that steady-state burning is achieved.

Fig. 5.1 shows the rotational velocity profile for several values of the mass accretion rate. The viscous processes transport angular momentum efficiently through the outer layers of the neutron star into the core, resulting in a small difference in Ω between the outer and inner part of our model of $\Delta\Omega/\Omega \sim 10^{-4}$. The largest change in Ω is at $y \simeq 10^8 \text{ g cm}^{-2}$. We will see that at this depth helium burning gen-

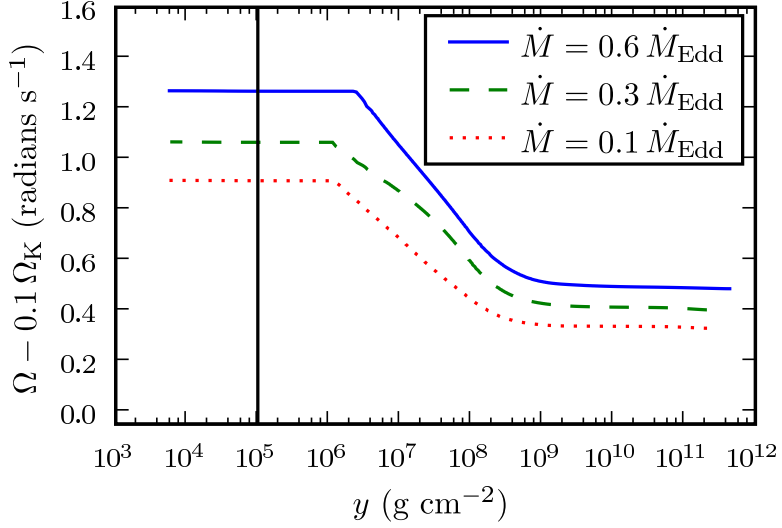


Figure 5.1: Rotational velocity Ω as a function of column depth y for three values of the mass accretion rate and an angular velocity of the core of $0.1 \Omega_K$. Accreted angular momentum is shared with the region to the left of the vertical line.

erates heat and changes the chemical composition. In the figure we indicate the region of the model where the accreted angular momentum is added as described in the previous section. Since the accreted angular momentum is quickly shared with this region, the angular momentum transport is not calculated in a physically correct way in that part of the model. Furthermore, at $y \lesssim 10^7 \text{ g cm}^{-2}$ lies the pseudo-Lagrangian region where the accreted matter is added. Therefore, we will limit most plots to show the Lagrangian part, $y \gtrsim 10^7 \text{ g cm}^{-2}$.

For higher accretion rates, angular momentum is added faster to the star, resulting in a higher shear (Figure 5.2 top), although the difference is less than an order of magnitude in the range of accretion rates we consider. Since the accreted material originally rotates with the Keplerian velocity, models with a more slowly rotating core experience an up to 10^3 times larger shear (Fig. 5.2 bottom). The shear profiles show two broad ‘bumps’: one in the region $10^7 \lesssim y \lesssim 10^9 \text{ g cm}^{-2}$ and another at $y \gtrsim 10^{10} \text{ g cm}^{-2}$. We will see below that due to nuclear burning and diffusion there is a gradient in the chemical composition in these regions. This gradient has a stabilizing effect which reduces the angular momentum transport, causing a somewhat larger shear.

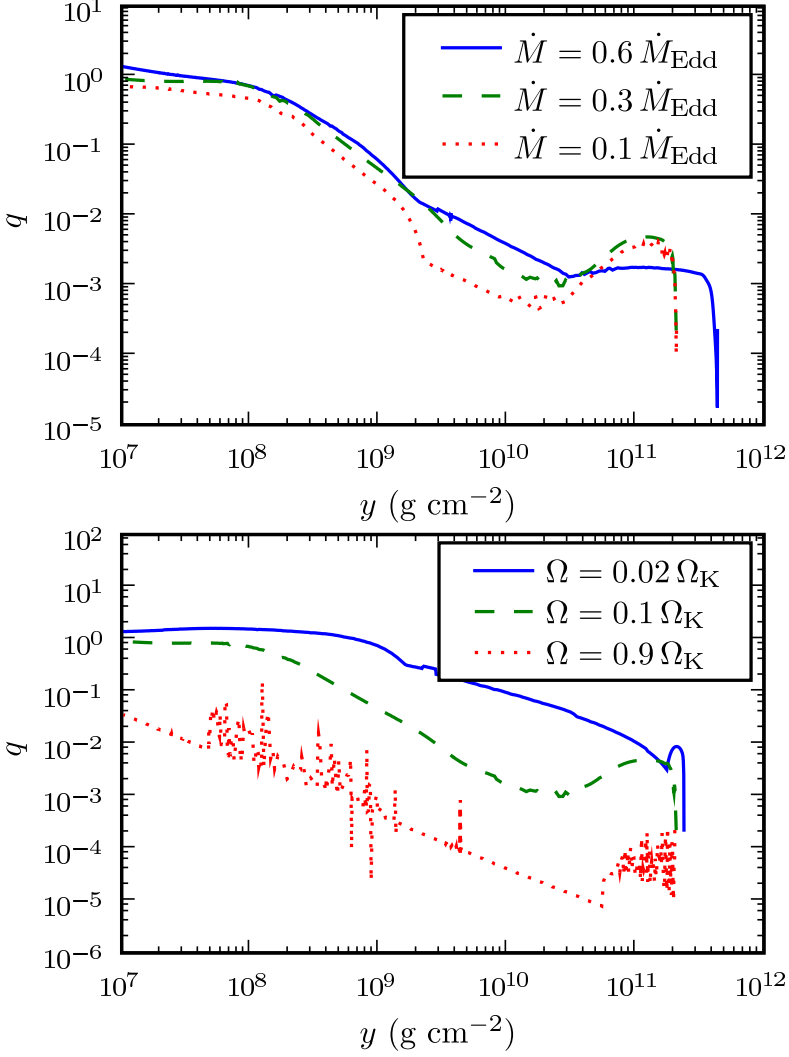


Figure 5.2: Comparison of shear q with column depth y . *Top*: models with different mass accretion rates and their rotation rate of the core fixed to $\Omega = 0.1 \Omega_K$. Note that the model with $\dot{M} = 0.6 \dot{M}_{\text{Edd}}$ accreted for a longer time and, therefore, reaches larger depths. *Bottom*: models with different rotation rates of the core and a fixed accretion rate of $\dot{M} = 0.3 \dot{M}_{\text{Edd}}$. The model with $\Omega = 0.9 \Omega_K$ suffers from numerical noise.

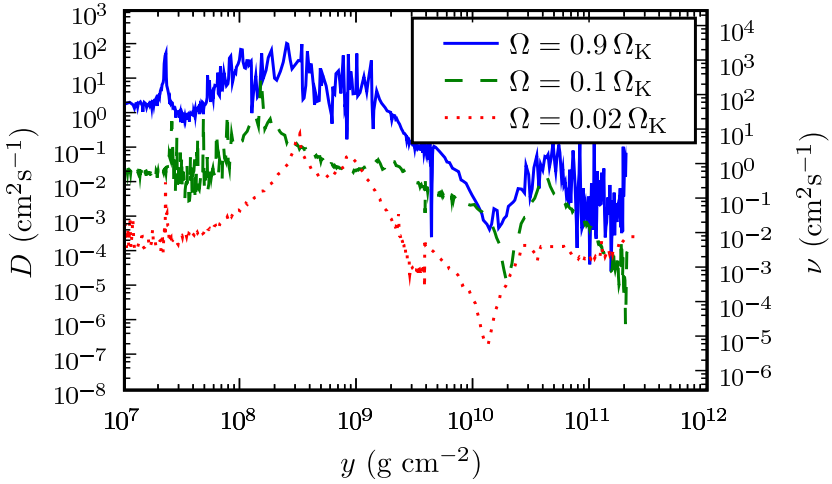


Figure 5.3: Non-magnetic diffusivity D and viscosity ν due to Eddington-Sweet circulation as a function of column depth y for different values of the angular velocity of the core Ω and an accretion rate of $\dot{M} = 0.3 \dot{M}_{\text{Edd}}$. Note that ν is larger than D by a fixed factor of 30. Especially the model with $\Omega = 0.9 \Omega_K$ suffers from numerical noise.

The presence of shear causes turbulence and induces a magnetic field, that drive diffusion and viscous processes. We obtain a magnetic field with a radial component $B_r \simeq 10^5$ G and a toroidal component $B_\phi \simeq 10^{10}$ G. We calculate D and ν both due to the hydrodynamic instabilities and due to the (generation of) the magnetic field (Fig. 5.3, 5.4 and 5.5). We find the latter to have the largest contribution to the diffusivity and viscosity. Of the non-magnetic instabilities, Eddington-Sweet circulation is the dominant process. At $y \simeq 10^8$ g cm $^{-2}$ D and ν due to this process peak, since at this depth the luminosity gradient is largest due to helium burning. Note that convective mixing plays no role in our models of steady state burning, because heat transport is radiative throughout our models, except at the onset of a flash, similar to what is found by Woosley et al. (2004).

We investigate how D and ν depend on the rotation rate Ω . The contribution from the non-magnetic instabilities increases with increasing Ω (Fig. 5.3). For the Eddington-Sweet circulation the diffusivity and viscosity are proportional to Ω^2 (Kippenhahn 1974; Heger et al. 2000). The diffusivity due to the magnetic field generation increases towards lower rotation rates as, approximately, $D \propto \Omega^{-3/4}$ (Fig. 5.4). The precise dependence is influenced by buoyancy effects from tempera-

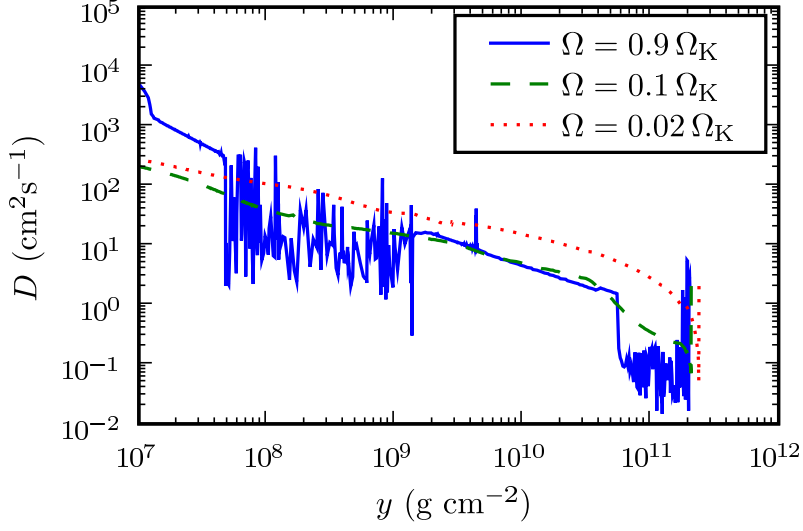


Figure 5.4: Magnetic diffusivity D as a function of column depth y for different values of the angular velocity of the core and an accretion rate of $\dot{M} = 0.3 \dot{M}_{\text{Edd}}$. A minimum in D is apparent at $\Omega \simeq 0.1 \Omega_K$. The model with $\Omega = 0.9 \Omega_K$ suffers from numerical noise.

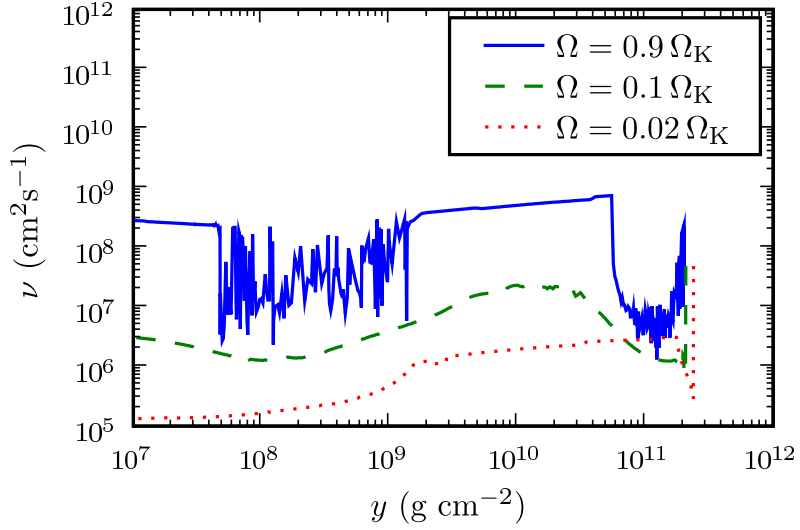


Figure 5.5: Magnetic viscosity ν as a function of column depth y for different values of the angular velocity of the core Ω . The model with $\Omega = 0.9 \Omega_K$ suffers from numerical noise.

ture and compositional gradients (Spruit 2002). The magnetic viscosity, which is induced by the magnetic torques instead of MHD instabilities, increases towards higher Ω , since it depends mostly on the rotation rate: $D \propto \Omega^{3/2}$ (Fig. 5.5). Interestingly, while the magnetic diffusivity dominates at most depths, for models with $\Omega \gtrsim 0.1 \Omega_K$ Eddington-Sweet circulation gives a contribution to the diffusivity which is equal or larger at the depth of $y \simeq 10^8 \text{ g cm}^{-2}$ where helium is burned.

During our calculations we assume angular momentum is accreted with an efficiency of 100%. Due to viscous processes in the disk, the actual efficiency may be lower. We investigate the dependency of the shear, diffusivity and viscosity on the accretion efficiency by comparing a model with 100% to a model with 0% efficiency. In the helium burning region, the difference is at most several tens of percents. For more realistic efficiencies the deviation from the 100% efficient model is likely even smaller. Therefore, we neglect this effect in our calculations.

The viscosity allows for the transport of angular momentum, leading in the envelope to the angular velocity profile we presented in Fig. 5.1. Similarly, diffusion mixes the chemical composition of our model. Without diffusion, the chemical profile consists on the outside of the star (Fig. 5.6 middle, left-hand side) of accreted helium which

burns at $y \simeq 10^8 \text{ g cm}^{-2}$, forming a layer of mostly carbon. On the inside (right-hand side) the composition is that of the initial model: 50% ^{12}C and 50% ^{16}O . When we include diffusion, ^4He is mixed down to higher column depths, while some ^{12}C is mixed all the way to the surface (Fig. 5.6 bottom). Due to the increased helium abundance at $y \gtrsim 10^8 \text{ g cm}^{-2}$, the energy generation rate is higher there compared to the models without diffusion (Fig. 5.6 top).

In the steady state helium is burned typically at the depth where the accretion timescale equals the burning timescale. In the case of diffusive mixing of the chemical composition, fuel can be transported to deeper layers than the accretion column. In this case, helium is burned down to the depth where the burning timescale equals the diffusion timescale. We determine as a function of column depth the burning and diffusion timescales t_{nuc} and t_{diff} for ^4He by calculating

$$t_{\text{nuc}}, t_{\text{diff}} = Y \left(\frac{\Delta Y}{\Delta t} \right)^{-1}, \quad (5.4)$$

with Y the ^4He mass fraction and ΔY the change in Y due to nuclear burning or diffusion during one time step Δt of our calculations (Fig. 5.7). In the inner part of the burning zone, where helium is mixed in, the diffusion and burning timescales differ by at most a few tens of percents, ensuring that steady-state burning can take place down to larger depths than without diffusion.

5.3.2 Effect of mixing on stability

The temperature in the burning shell has an important influence on the stability of the nuclear burning. Typically, burning is stable for higher temperatures of the neutron star envelope, which depends highly on the heat flux from the crust. We express this heat flux as a luminosity L_{crust} and investigate for which values burning is stable by starting at a high value of L_{crust} and subsequently lowering it at a rate which is slow with respect to the thermal timescale of the inner part of our model. For a certain value of L_{crust} nuclear burning no longer proceeds stably and a flash occurs. We refer to this as the critical luminosity L_{crit} . At that point we stop the calculation.

We perform this procedure for two models with $\Omega = 0.1 \Omega_K$ and $\dot{M} = 0.3 \dot{M}_{\text{Edd}}$. Both models take viscous processes into account, such that the angular velocity profiles are similar. However, we enable chemical diffusion only for one model, while the other is calculated without diffusion. For the model excluding chemical mixing, we start with stable burning (Fig. 5.8 top). Lowering L_{crust} ,

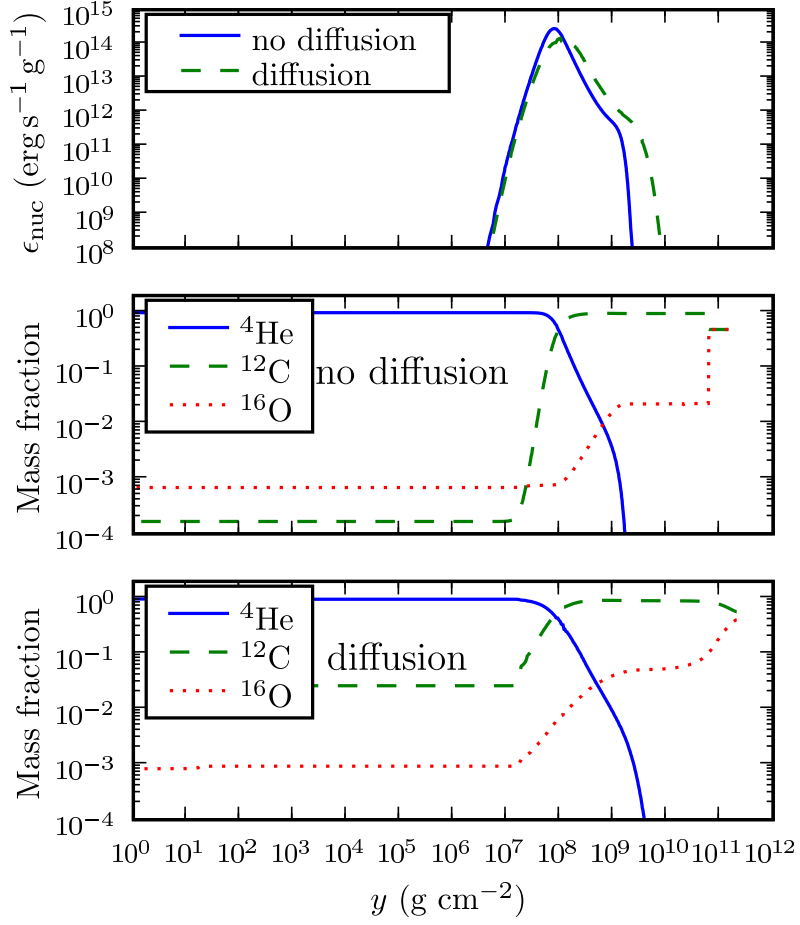


Figure 5.6: Nuclear energy generation rate ϵ_{nuc} and isotope mass fractions as a function of column depth y for two models with $\dot{M} = 0.3 \dot{M}_{\text{Edd}}$ and $\Omega = 0.1 \Omega_K$. One model is calculated including chemical diffusion, while the other is not.

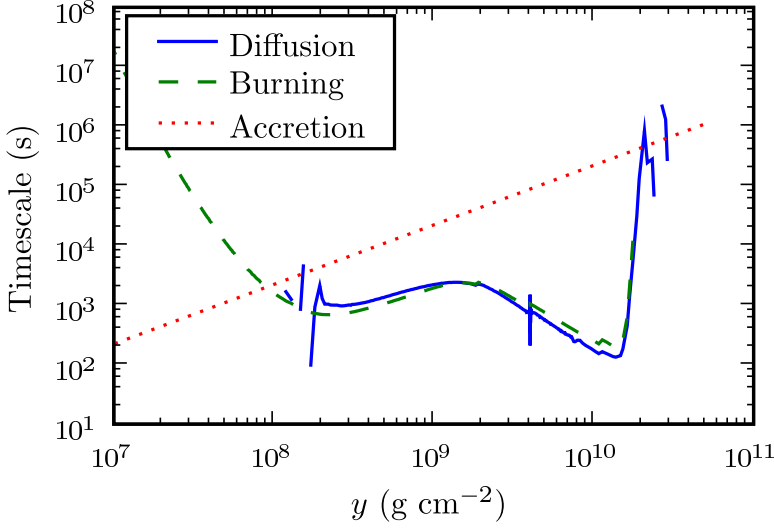


Figure 5.7: Timescales for helium burning, diffusion and accretion as a function of column depth y for $\Omega = 0.1 \Omega_K$ and $\dot{M} = 0.3 \dot{M}_{\text{Edd}}$.

helium shell burning exhibits oscillations with increasing amplitude. These oscillations are well resolved in time by our calculations. For $L_{\text{crust}} = 2.448 \cdot 10^{35} \text{ erg s}^{-1}$ the oscillation amplitude increases rapidly, until a flash occurs. We regard this as the onset of unstable burning. It is possible that what we regard as the onset of instability is actually just an oscillation with a large amplitude, which could be followed by a series of oscillations before the unstable situation is reached. Nevertheless, observing how fast the amplitude of the oscillations increases in a small interval of L_{crust} , we expect that our measure of L_{crit} is accurate within 0.2%. The period of the pulses increases, from approximately $6 \cdot 10^2 \text{ s}$ at $L_{\text{crust}} = 2.448 \cdot 10^{35} \text{ erg s}^{-1}$ to $9 \cdot 10^2 \text{ s}$ at $L_{\text{crust}} = 2.444 \cdot 10^{35} \text{ erg s}^{-1}$, just before the final two oscillations.

For the model including diffusion, the behavior is similar (Fig. 5.8 bottom). The amplitude of the oscillations, however, is large for a broader range of L_{crust} and the behavior is less regular. During intervals of $10^4 - 10^5 \text{ s}$ the amplitude slowly increases and subsequently decreases either slowly or fast. The cause of the irregularities is likely the increased complexity of our model when turbulent mixing is included, giving rise to more ‘noise’. Despite the irregular behavior, we can still discern a general trend towards oscillations with larger amplitudes while we lower L_{crust} . The period of the oscillations is $\sim 1.2 \cdot 10^3 \text{ s}$

and does not change significantly. The value of L_{crit} we obtain for this model is over a factor two smaller than for the model without diffusion: $L_{\text{crit}} = 1.180 \cdot 10^{35} \text{ erg s}^{-1}$. This shows the substantial stabilizing effect of turbulent mixing. The uncertainty in L_{crit} is likely larger than for the model without diffusion due to the increased noise. Note that for the chosen angular velocity of the core, $\Omega = 0.1 \Omega_K$, the diffusivity is at its minimum value. For another choice of Ω , the effect is likely to be even larger.

We investigate the dependence of L_{crit} on Ω by calculating two series of models, including and excluding diffusion. Due to the increased noise, the models which include diffusion are computationally more expensive. Therefore, we limit ourselves to two models with relatively low rotation rates, $\Omega = 0.05 \Omega_K$, $0.1 \Omega_K$, and two models with high rotation rates: $\Omega = 0.8 \Omega_K$, $0.9 \Omega_K$. We find that L_{crit} is lower by more than a factor of 2 for all values of Ω we consider (Fig. 5.9). Furthermore, even for the models without diffusion we see a decrease in L_{crit} of up to 12% when going to higher rotation rates. This stabilizing effect is due to the centrifugal force $F_{\text{cf}} \propto \Omega^2$, which lowers the effective gravity, increasing the efficiency of stabilizing effects. Note that due to the one-dimensional approximation we use, this is likely an underestimation (see Sect. 5.4.2).

We noted earlier that diffusivity due to Eddington-Sweet circulation can be comparable to or even exceed the diffusivity due to magnetic fields. To investigate the effect of non-magnetic instabilities alone, we created a model with $\Omega = 0.05 \Omega_K$ and $\dot{M} = 0.3 \dot{M}_{\text{Edd}}$ including only angular momentum transport and chemical diffusion due to non-magnetic instabilities. Angular momentum transport is much less efficient, leading to a large shear. The secular shear instability drives the diffusivity and viscosity. For this model we find $L_{\text{crit}} = 1.948 \cdot 10^{35} \text{ erg s}^{-1}$, which is 23% lower than what we find without diffusion (Fig. 5.9).

When we change L_{crust} it takes a thermal timescale for our model to adjust. Since we lower L_{crust} continuously, this introduces a systematic error in the value of L_{crit} we obtain, as the model is not fully adjusted to that value of L_{crust} when we stop the calculation. To estimate the systematical error we take one model and lower L_{crust} at different rates, all slow with respect to the thermal timescale of the model, and find that the difference in L_{crit} and, ergo, the systematic error is about 4%.

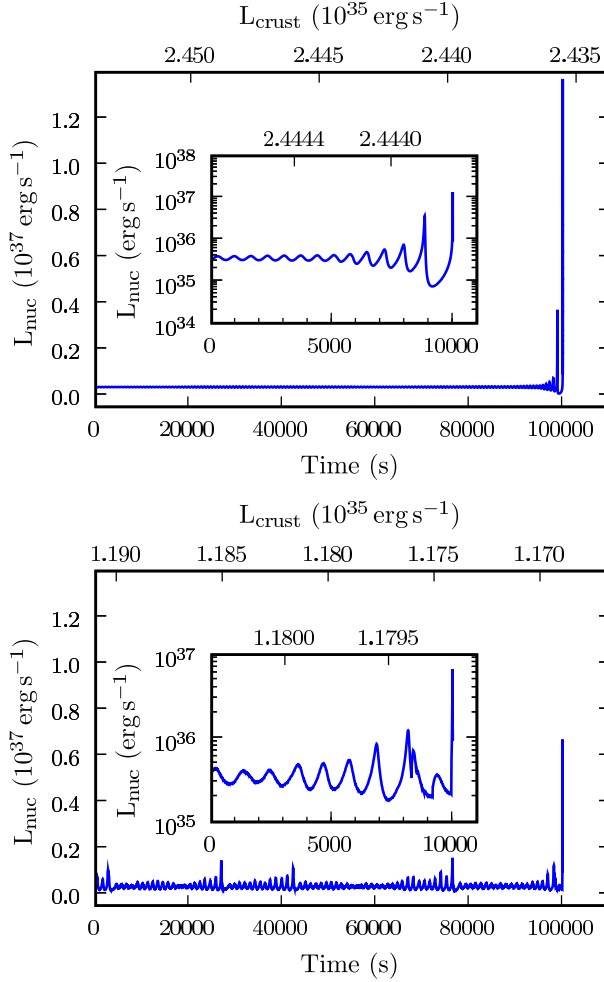


Figure 5.8: Nuclear luminosity L_{nuc} due to helium burning as a function of time, while lowering L_{crust} at a constant rate. Shown are the last 10^5 s before the onset of unstable burning. The insets zoom in on the last 10^4 s. *Top*: model without diffusion for $\Omega = 0.1 \Omega_K$ $\dot{M} = 0.3 \dot{M}_{\text{Edd}}$. While burning is initially stable, we see an increase in the amplitude of oscillations, until finally burning becomes unstable. *Bottom*: similar model including diffusion. Amplitude of oscillatory burning is much larger and less regular than for the model without diffusion.

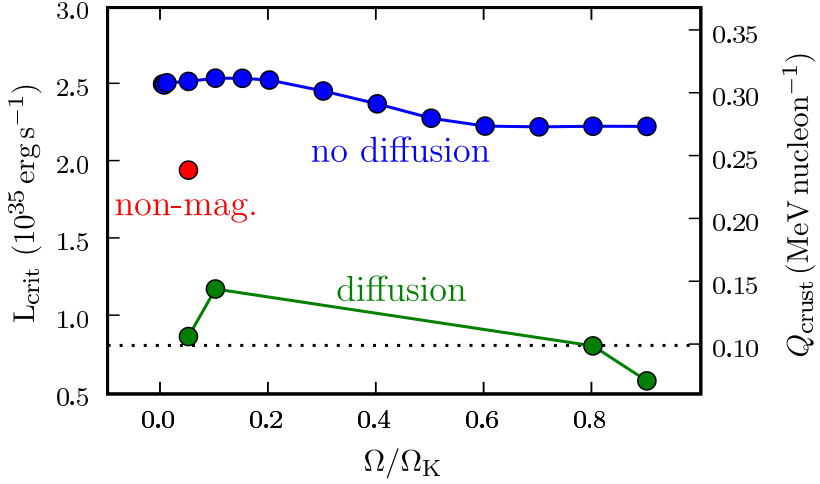


Figure 5.9: The heat flux from the crust at the transition of stable to unstable burning L_{crit} as a function of the angular velocity Ω of the core in units of the Keplerian velocity at the surface for models with $\dot{M} = 0.3\dot{M}_{\text{Edd}}$. Each dot represents one model. Two series of models are calculated: without (upper) and with diffusion (lower). One model is calculated without the effect of magnetic fields (middle). Here the secular shear instability drives the chemical mixing. On the right-hand vertical axis is indicated the heat generated in the crust per accreted nucleon, Q_{crust} , for the given accretion rate. The dotted line indicates $Q_{\text{crust}} = 0.1 \text{ MeV nucleon}^{-1}$, which is used in many studies.

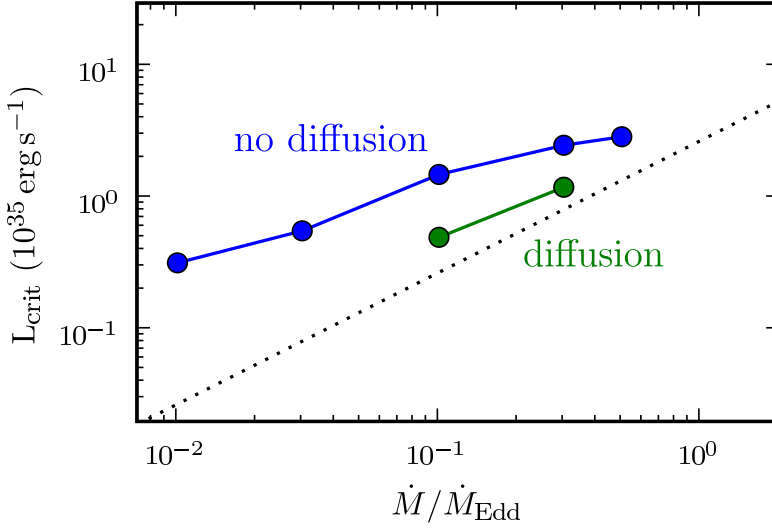


Figure 5.10: The heat flux from the crust at the transition of stable to unstable burning L_{crit} as a function of the accretion rate \dot{M} for models with $\Omega = 0.1 \Omega_K$. Each dot represents one model. Two series of models are calculated: without (upper) and with diffusion (lower). The dotted line indicates the luminosity from the crust as a function of \dot{M} for an energy release of $Q_{\text{crust}} = 0.1 \text{ MeV nucleon}^{-1}$, which is used in many studies.

5.3.3 Mass accretion rate dependence

The dependence of L_{crit} on the mass accretion rate is investigated by calculating two series of models with and without diffusion, in a similar way as we studied the dependence on Ω . The angular velocity of the core is set to $0.1 \Omega_K$. We find that L_{crit} increases towards higher mass accretion rates (Fig. 5.10) and is for all calculated models larger than the luminosity expected from a crustal energy release of $Q_{\text{crust}} = 0.1 \text{ MeV nucleon}^{-1}$, which is used in many studies (see Sect. 5.2.5). For the models without diffusion, the trend indicates that the accretion rate above which the luminosity of the crust exceeds L_{crit} lies roughly between one and ten times \dot{M}_{Edd} , which is in agreement with previous studies (Bildsten 1998).

To understand the behavior of increasing L_{crit} for larger values of \dot{M} , we follow the stability analysis of thermonuclear burning in a thin shell by Giannone & Weigert (1967) (see also Yoon et al. 2004b). These

authors derive an expression for the inverse of the growth time scale of temperature perturbations by considering both thermonuclear burning and radiative cooling (equation 16 in Giannone & Weigert 1967). In this expression the luminosity from below the thin shell is ignored. We can include L_{crust} by adding it to the luminosity of the shell, which results in an extra term in the numerator of the right-hand side of equation (16) in Giannone & Weigert (1967), proportional to $L_{\text{crust}}/\Delta M$. Here, ΔM is the mass of the shell, which for steady-state burning is proportional to the mass accretion rate. Increasing \dot{M} increases $-L_{\text{crust}}/\Delta M$, leading to a lower perturbation growth time scale. Therefore, to keep the same perturbation growth time scale, a larger value of L_{crust} is required at larger \dot{M} . This simple picture suggests that L_{crit} depends linearly on \dot{M} , while Fig. 5.10 suggests for the series of models without diffusion that the relation deviates from a linear dependence. In fact, for larger \dot{M} also the temperature and density in the shell are larger, which influences the perturbation growth time scale as well.

5.4 DISCUSSION

We performed detailed calculations of thin shell burning of accreted helium on a neutron star. Similar to what was found by Yoon et al. (2004a) for white dwarfs, also for neutron stars rotational mixing leads to more stable burning. As was demonstrated by Piro & Bildsten (2007), rotationally induced magnetic fields provide in most cases the dominant contribution to the diffusivity and viscosity. Yoon et al. (2004a) considered only non-magnetic hydrodynamic instabilities. In those models the transport of angular momentum is less efficient, resulting in a much larger shear. The secular shear instability is in that case the driver of turbulent mixing. We take magnetic fields into account through the Tayler-Spruit dynamo (Spruit 2002), which causes efficient angular momentum transport and turbulent mixing. Eddington-Sweet circulation also plays an important role, especially in the burning zone, at the peak of the energy generation rate, where there is a steep gradient in the luminosity.

In our models with diffusion the geometrical thickness of the burning shell is larger (Fig. 5.6). E.g., for a model with $\Omega = 0.1 \Omega_K$ and $\dot{M} = 0.3 \dot{M}_{\text{Edd}}$ the thickness of the burning shell is 6.7 m excluding and 8.7 m including diffusion, where we define the shell such that at the boundary the energy generation rate is 10^{-3} times the peak value. This results in an increased stability of thermonuclear burning.

Due to the increased stability, the critical value of the heat flux for the crust L_{crit} at the transition of (un)stable burning is lower for mod-

els that include diffusion. Even for the rotation rate which gives the minimum diffusivity, nuclear burning proceeds stably down to values for L_{crit} that are a factor two lower than for the non-diffusion case. In these calculations we vary the flux from the crust independently from the mass accretion rate. For several values of \dot{M} and Ω we determine L_{crit} . Observationally, this boundary is placed at $\dot{M} \simeq 0.1\dot{M}_{\text{Edd}}$. At this accretion rate, we find $L_{\text{crit}} = 0.508 \cdot 10^{35} \text{ erg s}^{-1}$ for a model with $\Omega = 0.1\Omega_K$. Assuming the heat flux from the crust is the main source of this luminosity, this corresponds to an energy deposition in the crust of $0.27 \text{ MeV nucleon}^{-1}$. This is approximately twice the value of $0.15 \text{ MeV nucleon}^{-1}$ used in many previous studies. Nevertheless, it is in agreement with the increased heat deposition in the crust from calculations by Gupta et al. (2007).

It is especially interesting to note that we obtain this result already at the value for Ω for which the diffusivity is minimal. Piro & Bildsten (2007) find this behavior only at low rotation rates: $\Omega \lesssim 0.1\Omega_K$. The Taylor-Spruit mechanism considers stabilizing effects due to temperature and compositional stratification. Piro & Bildsten (2007) simplify their models by taking into account only the former when determining the recurrence time of bursts and the condition for stable burning. This allows for a simple dependence of D on Ω of $D \propto \Omega^{-3/4}$. However, by including both stabilizing effects the dependence of D on Ω and q is more complex. In our calculations we find that the spread in the diffusivity in the considered range of rotation rates is at most one order of magnitude. Furthermore, we find that at high angular velocities Eddington-Sweet circulations drive mixing just as efficiently as the magnetic instabilities at low rotation rates. This means that for all rotation rates the stability of shell burning is increased by chemical mixing due to rotation and rotationally induced magnetic fields.

5.4.1 *Non-magnetic mixing*

In our models we find that the magnetic instabilities and torques provide the most efficient mixing of the chemical composition and angular momentum. The only exception is found at higher rotation rates, when the Eddington-Sweet circulation provides an important contribution to the diffusivity in the helium burning shell. Several studies need the Tayler-Spruit dynamo to reproduce observed quantities: Heger et al. (2005) model the pre-supernova evolution of massive stars and use the angular momentum transport due to rotationally induced magnetic fields to explain observed pulsar frequencies. Suijs et al. (2008) performed similar calculations for white dwarf progenitors and find

that angular momentum transport by magnetic torques is needed to explain the observed range of white dwarf rotation rates.

However, the mechanism of the Tayler-Spruit dynamo is uncertain. Zahn et al. (2007) performed calculations with three-dimensional models which do not reproduce the dynamo effect. Therefore, it is possible that this mechanism has a lower efficiency or is absent. In that case, non-magnetic instabilities drive chemical mixing and angular momentum transport. These are less efficient by many orders of magnitude. This leads to a large shear, causing the secular shear instability to provide the dominant contribution to D and ν , similarly to what Yoon et al. (2004a) found in white dwarf models which also did not include a rotationally induced magnetic field. For this model we find a value of L_{crit} that is 23% lower than for similar models that do not take diffusion into account (cf. Fig. 5.9). This model has a rotation rate of $0.05\Omega_K$. Models with a slower rotating core will have a higher shear, which may result in a lower value of L_{crit} . Therefore, even without magnetic fields, the effect of rotational mixing on the stability of helium shell burning is considerable.

5.4.2 *Centrifugal force*

Another stabilizing effect of rotation is provided by the centrifugal force. Yoon et al. (2004a) found that for shell burning in white dwarfs, the centrifugal force lowers the density and degeneracy in the shell, which leads to increased stability. We created a series of models without chemical mixing and found that for increasing Ω , L_{crit} is lower by up to 12%. However, this likely is an underestimation. Our implementation of the centrifugal force is a one-dimensional approximation. The centrifugal force depends on latitude, being largest at the equator and vanishing at the poles. Our calculations use a value which is averaged over latitude (e.g. Heger et al. 2000). In the case of rigidly rotating polytropes this approximation has been found accurate for rotation rates up to $0.6\Omega_K$ (Yoon et al. 2004a and references therein). Therefore, we limit the effect of the centrifugal force above 60% of the critical velocity. In actuality, the centrifugal force may reduce L_{crit} even further for fast spinning neutron stars.

5.4.3 *Marginally stable burning*

Revnivtsev et al. (2001) observe from the LMXBs 4U 1636–53, 4U 1608–52 and Aql X-1 millihertz quasi-periodic oscillations (mHz QPOs) and speculate that this phenomenon may be related to a special mode of

nuclear burning. This behavior is thought to occur at the boundary of stable and unstable burning, since it is observed in a narrow range of accretion rates, where at lower accretion rates type I X-ray bursts were observed while they were absent at higher accretion rates. The oscillatory burning mode at this boundary was expected from one-zone models by Paczynski (1983) as ‘marginally stable burning’. Heger et al. (2007) reproduce this behavior in multi-zone numerical models of the neutron star envelope, who derive the period of the oscillations P_{osc} to be the geometric mean of the accretion and thermal timescales: $P_{\text{osc}} = \sqrt{t_{\text{acc}} t_{\text{therm}}}$.

Altamirano et al. (2008) observe frequency drifts in mHz QPOs from 4U 1636–53. The mHz QPOs are observable for approximately 10^4 s. During this time the frequency drops by several tens of percents. At a certain point a type I X-ray burst is observed, after which no oscillations are detected for some time. The change in period is not found to be directly related to variations of the X-ray flux on short timescales. Therefore the frequency of the oscillations does not appear to be sensitive to variations in the accretion rate. Furthermore, Molkov et al. (2005) observed a long type I X-ray burst from SLX 1735–269 which exhibits ~ 10 mHz oscillations during the burst decay. Also in this case a drift to lower frequencies takes place during the part of the X-ray light curve where the black body temperature is observed to decrease.

Also in our models we observe oscillations close to the boundary of (un)stable burning. This is most pronounced in the models without diffusion. When we lower L_{crust} , effectively cooling our burning layer, the frequency of the oscillations decreases by several tens of percents until a flash occurs. The frequency drift takes place over a small range of L_{crust} , just before the onset of a flash. The amplitude of the oscillations is larger in this range, making the oscillations more easily detectable. This supports the suggestion by Altamirano et al. (2008) that the frequency drifts are due to cooling of deeper layers and could explain why it is not sensitive to short-term variations of the accretion rate. The cooling could, for instance, be caused by the slow release of energy from a deeper layer that was heated up during an X-ray burst.

Note that the models that include diffusion display oscillations as well, but the behavior is much more irregular, as the amplitude of the oscillations changes in a seemingly erratic way. This makes it difficult to draw conclusions from the oscillatory behavior. We suspect that numerical noise is the source of this behavior. A different implementation of the mixing processes in the model may be required to improve this.

5.4.4 *Further consequences of mixing*

Apart from the increased stability of helium burning, chemical mixing can give rise to other effects. Superbursts, which are energetic type I X-ray bursts that last up to a day, are thought to be the result of a carbon flash (Strohmayer & Brown 2002; Cumming & Bildsten 2001). Fifteen superbursts have been observed from ten sources, most of which have accretion rates $\dot{M} \gtrsim 0.1\dot{M}_{\text{Edd}}$ (Kuulkers 2004; in 't Zand et al. 2004a; Remillard et al. 2005; Kuulkers 2005). As noted by Piro & Bildsten (2007), turbulent mixing could allow for stable burning of helium at these accretion rates, building up a thick carbon layer. However, all superbursters exhibit normal type I bursts as well. In the presence of hydrogen, the rp-process creates heavy isotopes, while lowering the carbon abundance. It has proven difficult to explain how carbon can survive many normal bursts to fuel a superburst (e.g., Keek et al. 2008).

While helium is mixed down, we find that carbon is mixed up to smaller depths (Fig. 5.6). For our helium-accreting model this is of little consequence, but many neutron stars in LMXBs accrete hydrogen-rich material. Hydrogen burns via the hot-CNO cycle. The energy generation rate of this process depends on the mass fractions of the CNO seed nuclei, which are increased if carbon is mixed into the hydrogen/helium layer. This may lower the hydrogen mass fraction in the burning shell. If subsequently a hydrogen/helium flash occurs, there is less hydrogen present for the rp-process to destroy the carbon created by helium fusion. This could allow for the creation of a thick carbon layer to fuel a superburst.

Our models show that carbon is mixed all the way to the neutron star photosphere at $y = 1 \text{ g cm}^{-2}$. In case hydrogen-rich material is accreted, the ashes of hydrogen and helium burning can contain heavy isotopes, e.g. iron. If mixing increases the mass fractions of these isotopes near the surface, this would allow for the detection of absorption lines from the neutron star. Measuring the gravitational redshift of the absorption line provides constraints on the neutron star equation of state, such as has been shown with the tentative result of Cottam et al. (2002). This is similar to the result of Weinberg et al. (2006), who predict that convection during luminous X-ray bursts can mix heavy elements to the photosphere.

5.5 CONCLUSION

A long-standing problem in the theory of thermonuclear burning in the envelope of accreting neutron stars is the accretion rate at which

the burning becomes (un)stable. While observations point at $\dot{M} \simeq 0.1\dot{M}_{\text{Edd}}$, the models find $\dot{M} \simeq \dot{M}_{\text{Edd}}$ when hydrogen-rich material is accreted and $\dot{M} \simeq 10\dot{M}_{\text{Edd}}$ when it is hydrogen-deficient. Recent relatively simple analytical and numerical models (Piro & Bildsten 2007) suggest that turbulent mixing due to rotationally induced magnetic fields leads to increased stability of the thin shell burning on neutron stars, similar to the effect of mixing due to hydrodynamic instabilities in the white dwarf case (Yoon et al. 2004a).

For the first time we perform detailed calculations of nuclear burning of accreted helium in the neutron star envelope using an extensive numerical model including both magnetic and non-magnetic hydrodynamic instabilities. In most cases the magnetic instabilities and torques provide the largest contribution to the diffusivity and the viscosity, respectively, while Eddington-Sweet circulation becomes important at high rotation rates. We create models with an accretion rate of $\dot{M} = 0.3\dot{M}_{\text{Edd}}$ and different rotation rates of the core. We do not couple the heat flux from the crust to the mass accretion rate, but leave it as a free parameter, finding the threshold value between stable and unstable burning. This value is lower by at least a factor two for models including diffusion, in comparison with models without chemical mixing. If we ignore the rotationally induced magnetic fields, mixing due to the secular shear instability can lower the critical heat flux by several tens of percents. For larger rotation rates the centrifugal force allows for stable burning at crustal heat fluxes that are up to 12% smaller in our models. Note, however, that this is likely an underestimation, because of the employed approximation of the centrifugal force in our one-dimensional model.

These effects show that the stability of helium shell burning is increased due to rotation, such that stable burning can take place at sub-Eddington accretion rates. Magnetic field generation through the Tayler-Spruit dynamo yields the strongest effect. However, even without magnetic fields, hydrodynamic instabilities and the centrifugal force increase stability substantially. We calculate models including diffusion which accrete at 10% and 30% of the Eddington limited mass accretion rate and find that in both cases the critical heat flux from the crust lies above the value inferred from an energy release of $Q_{\text{crust}} = 0.1 \text{ MeV nucleon}^{-1}$, which is used in many previous studies. Therefore, an increased energy release is required, as found recently by Gupta et al. (2007). Combined with this larger energy release, rotational mixing and rotationally induced magnetic fields may explain the transition from unstable to stable burning at the observed accretion rate.

Our models exhibit oscillations close to the transition of stable to unstable burning, which have been related to the observed mHz QPOs (Heger et al. 2007). When we lower the heat flux from the crust at a constant rate, we find that the frequency of the oscillations is reduced by up to several tens of percents. This supports the suggestion by Altamirano et al. (2008) that the frequency drifts observed in mHz QPOs are due to cooling.

THERMONUCLEAIRE VERBRANDING OP ACCRETERENDE NEUTRONENSTERREN

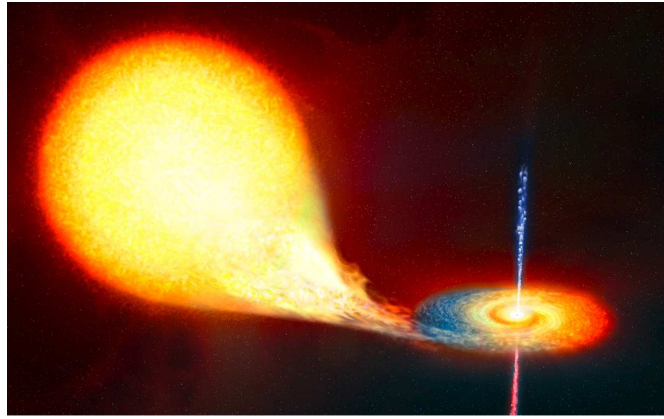
Nederlandse samenvatting

Neutronensterren zijn bijzondere, compacte sterren. Wat er precies in het binnenste van deze sterren gebeurt is tot op de dag van vandaag een mysterie. Heel af en toe worden op het oppervlak van neutronensterren enorme kernexplosies waargenomen. De studie van deze ontploffingen geeft aanwijzingen voor het oplossen van dit mysterie. Dit hoofdstuk geeft een korte introductie over neutronensterren en een samenvatting van het onderzoek dat in dit proefschrift gepresenteerd wordt.

6.1 VAN ZEER GROOT TOT UITERST KLEIN

Om te begrijpen hoe iets groots als een ster in elkaar steekt, moeten we vaak gebruik maken van onze kennis van de allerkleinste deeltjes, zoals de atomen. Zo was het lange tijd onbekend waar de Zon de energie vandaan haalt om zoveel licht uit te stralen. In laboratoria ontdekten men dat bij hoge temperatuur en dichtheid kleine atomen, zoals waterstof en helium, kunnen fuseren tot zwaardere atomen, zoals koolstof. Bij dit fusieproces komt veel energie vrij. Het was bekend dat de Zon veel waterstof bevat. Toen begreep men dat fusie van waterstof de energiebron van de Zon moet zijn. Zo hebben metingen in laboratoria veel inzicht verschaft over de omstandigheden en processen in het binnenste van sterren.

Er is echter een type ster waarvoor onze kennis op het gebied van de allerkleinste deeltjes niet toereikend is: de neutronenster. Dit is een zeer compacte ster. De massa van een neutronenster is niet bijzonder: ongeveer anderhalf keer die van de Zon. Echter, al die massa is samengeperst binnen een straal van slechts tien kilometer. Dit betekent dat de dichtheid binnen in de neutronenster zeer hoog is, hoger zelfs dan in de kern van een atoom. De omstandigheden in zo'n compacte ster zijn zo extreem, dat ze niet na te bootsen zijn in een laboratorium, zelfs niet in de deeltjesversnellers van het CERN. Er zijn wel theorieën over hoe een neutronenster van binnen is opgebouwd. Omdat de dichtheid in de neutronenster hoger is dan in een atoomkern, gaan deze theorieën ervan uit dat de kern van een neutronenster bestaat uit deeltjes



Figuur 6.1: Neutronenster in een dubbelster-systeem. Deze tekening geeft aan hoe een dergelijk systeem er waarschijnlijk uit ziet. Van de begeleider (links) wordt materie aangetrokken. Alvorens het materiaal op de neutronenster valt, komt het in een schijf (rechts) terecht. De neutronenster is op deze tekening een klein stipje middenin de schijf. *Bron: ESA.*

die nog kleiner dan atomen zijn. Volgens de oudste theorie worden de atomen bij deze grote dichtheden omgevormd tot neutronen. Door deze theorie heeft de ster de naam 'neutronenster' gekregen. Er zijn ook theorieën die voorspellen dat nog exotischere deeltjes ontstaan. Welke van deze theorieën correct is kan helaas niet in een laboratorium bevestigd worden. We kunnen het alleen testen door met telescopen neutronensterren te bestuderen.

6.2 NEUTRONENSTERREN

Neutronensterren zijn te zien in vele bijzondere gedaanten. Zo zien radiotelescopen deze sterren als 'pulsars', waarvan zeer regelmatig radiopulsen waargenomen worden. Ook de röntgentelescopen op satellieten boven de Aarde kunnen neutronensterren zien. Van ongeveer negentig van deze sterren worden met enige regelmaat speciale flitsen röntgenstraling waargenomen.

Al deze flitsen komen van neutronensterren die vlak bij een andere ster staan, en daarmee een zogenaamde dubbelster vormen (zie figuur 6.1). De begeleider is bijvoorbeeld een ster zoals onze Zon. De twee sterren zijn gevangen door elkaars zwaartekracht en draaien

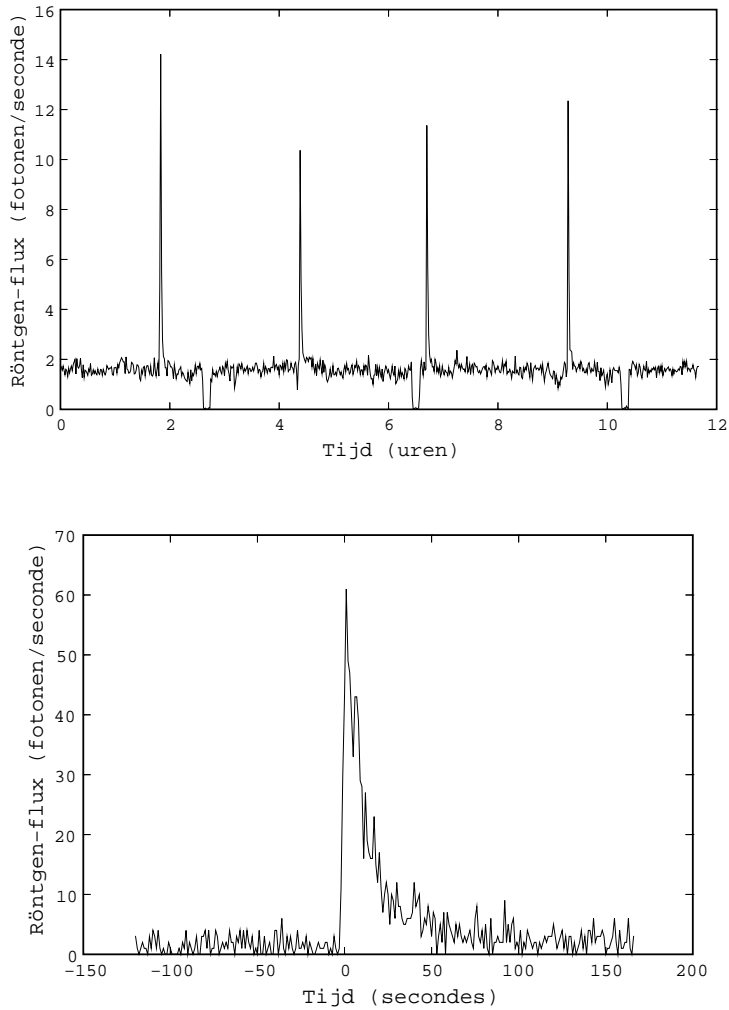
samen in een baan rondom hun gemeenschappelijk zwaartepunt. De neutronenster is zwaarder dan de andere ster en heeft een sterkere zwaartekracht. Hierdoor trekt hij materie aan vanaf het oppervlak van de begeleider. Deze materie valt van de ster naar de neutronenster toe en komt in een baan er omheen, waar het een platte schijf vormt. Van de binnenkant van de schijf valt uiteindelijk het materiaal op de neutronenster. In de schijf is veel wrijving waardoor de schijf gaat gloeien. Door de zeer hoge zwaartekracht die bij de ster heerst, komt van de gloeiende schijf vooral röntgenstraling af.

6.3 RÖNTGENFLITSEN

Wanneer we met een röntgentelescoop naar een dergelijk systeem kijken zien we een constante hoeveelheid straling van de gloeiende schijf (Figuur 6.2 boven). De neutronenster zelf zendt minder röntgenstraling uit, en is met een röntgentelescoop normaal gesproken niet zichtbaar. Af en toe is er echter een piek te zien: een flits röntgenstraling. Zoomen we in op de flits, dan zien we dat deze een speciale vorm heeft: de hoeveelheid straling stijgt eerst snel en neemt daarna langzaam af (Figuur 6.2 onder). Deze flits is afkomstig van het oppervlak van de neutronenster. Wanneer materiaal van de andere ster op de neutronenster valt, vormt het daar een laagje dat in de loop van de tijd dikker wordt. Dit materiaal is een mengsel van waterstof en helium. Als de laag slechts een paar meter dik is, is door de extreem hoge zwaartekracht de druk al zo groot dat spontaan kernfusie van waterstof en van helium begint. Onder bepaalde omstandigheden verloopt dit proces explosief: binnen enkele seconden ‘verbrandt’ het hele oppervlak, waarbij veel röntgenstraling vrijkomt. Waterstof en helium smelten samen tot zwaardere elementen zoals koolstof. Na de flits koelt de neutronenster langzaam af, gedurende tien tot honderd seconden. In de korte tijd van de flits kunnen we dus het oppervlak van de neutronenster zien. Dit soort flitsen wordt regelmatig waargenomen van ongeveer negentig neutronensterren met tussenpozen van uren tot dagen.

6.4 TE SNEL

Gedurende de tussenpozen wordt een nieuwe laag brandstof opgebouwd voor de volgende flits. Af en toe komt het voor dat een flits afgaat binnen een half uur na de vorige. Dit is veel te kort om een nieuwe laag brandstof op te bouwen. Wij hebben waarnemingen bestudeerd van de dubbelster EXO 0748-676 waarin met enige regelmaat



Figuur 6.2: Hoeveelheid röntgenstraling (flux) in de loop van de tijd uitgestraald door een neutronenster in een dubbelster. Deze waarneming is gedaan met de ESA satelliet XMM-Newton. *Boven*: gedurende vele uren zien we een constante flux van de gloeiende schijf, af en toe onderbroken door een flits. *Onder*: ingezoomd op één flits zien we de snelle stijging en de langzame afkoeling.

twee of soms zelfs drie flitsen elkaar opvolgen binnen tien tot twintig minuten. Uit onze analyse blijkt dat gemiddeld genomen tijdens een dubbele of drievoudige flits meer energie wordt uitgestraald dan wanneer slechts een enkele flits wordt gezien. Dit duidt erop dat na een enkele flits brandstof overblijft, die na ongeveer tien minuten alsnog ontbrandt in een nieuwe flits. Waarom niet alle brandstof tijdens de eerste explosie verbrandt en waarom de volgende flits altijd na tien minuten afgaat is nog onbekend.

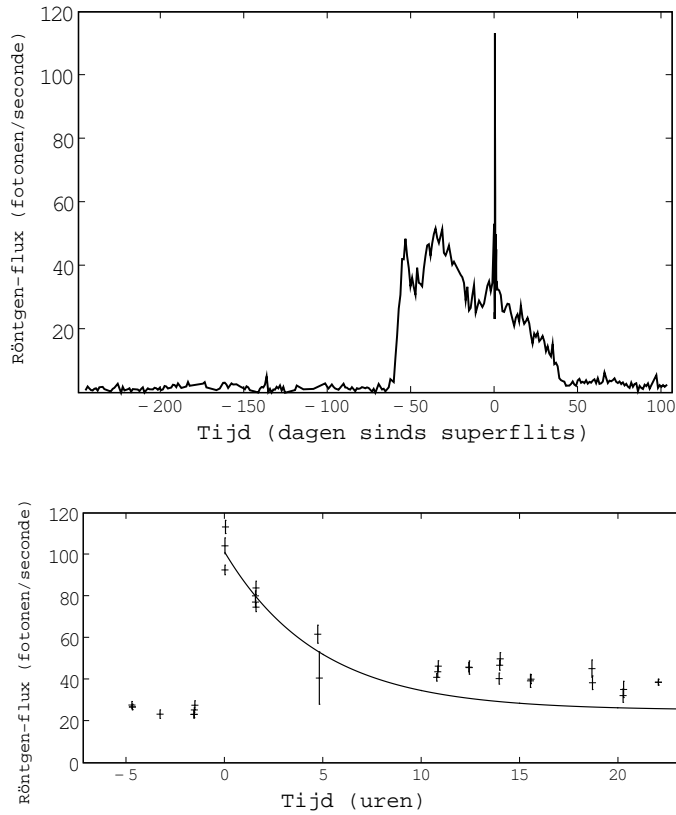
6.5 SUPERFLITSSEN

Sinds enkele jaren is een nieuw type röntgenflits bekend. Deze lijkt op het eerste gezicht op de gewone röntgenflitsen: binnen enkele seconden is de piek bereikt, waarna de neutronenster afkoelt (Figuur 6.3 onder). Echter, het afkoelen duurt niet honderd seconden, maar een hele dag. Gedurende deze tijd wordt duizend keer meer straling uitgezonden dan tijdens een gewone flits. Dit verschijnsel wordt dan ook een 'superflits' genoemd. Het proces achter de superflits is niet de fusie van een dunne laag waterstof of helium, maar van een honderd meter dikke laag met koolstof, die dieper onder het oppervlak van de neutronenster ligt. De koolstof ontstaat door de fusie van waterstof en helium, die van de andere ster is aangezogen. Het duurt ongeveer een jaar voor zo'n dikke laag koolstof is opgebouwd. Hierdoor zijn superflitsen veel zeldzamer dan de gewone röntgenflitsen: er zijn er tot nu toe maar vijftien gezien, afkomstig van tien neutronensterren.

In een poging om meer superflitsen te vinden, hebben we gezocht in een grote hoeveelheid waarnemingen met de Wide Field Camera's van de BeppoSAX-satelliet van dubbelsterren die lijken op degenen die superflitsen vertonen. Helaas werden geen nieuwe superflitsen gevonden, maar ook dit geeft ons belangrijke informatie. Dit betekent namelijk dat het opbouwen van de koolstof laag langer duurt dan de lengte van de waarnemingen (ongeveer 52 tot 76 dagen).

6.6 EEN GEWONE SUPERFLITS?

Om een superflits te krijgen zijn twee ingrediënten nodig. Ten eerste moet de laag met koolstof dik genoeg zijn, zodat de druk voldoende is voor ontbranding. Ten tweede moet de temperatuur binnen in de neutronenster hoog genoeg zijn. Het binnenste van de neutronenster wordt verwarmd als materie van de andere ster wordt aangezogen. Wanneer materiaal op het oppervlak valt, worden de diepere lagen samengeperst. Dit brengt processen op gang die het binnenste verhitten.



Figuur 6.3: Superflits waargenomen op 5 mei 2005 door de NASA satelliet RXTE. *Boven*: de hoge piek is de superflits. Licht van de gloeiende schijf is pas zichtbaar 55 dagen voor de superflits. *Onder*: de superflits ingezoomd. Ieder kruisje is een waarneming. De lijn geeft de afkoeling van de neutronenster aan naar het niveau voor de superflits. In werkelijkheid blijft de flux iets boven dit niveau.

De neutronensterren waarvan een superflits gezien is waren al meer dan tien jaar bezig met het aanzuigen van materie, zodat we er zeker van kunnen zijn dat de temperatuur binnenin de ster hoog genoeg was om de explosie te starten. Dit geldt voor alle neutronensterren met superflitsen, op één na.

Op 5 mei 2005 werd een superflits waargenomen door de NASA-satelliet RXTE (Figuur 6.3 onder). De eigenschappen van deze su-

perflits wijken niet af van die van superflitsen die van andere neutronensterren gezien zijn. Het is dus een normale superflits. Kijken we echter naar de hoeveelheid straling die over langere tijd van deze neutronenster gezien is, dan zien we niet een constante flux van straling van de schijf (Figuur 6.3 boven). Deze neutronenster begon pas 55 dagen voor de superflits met het aanzuigen van materie. Berekeningen die gebruik maken van de meest recente modellen van het binnenste van neutronensterren laten zien dat het na 55 dagen nog veel te koud is voor een superflits. Volgens onze kennis van het binnenste van neutronensterren had er geen superflits mogen plaatsvinden, terwijl er wel een is waargenomen. Deze tegenstrijdigheid laat zien dat er nog iets belangrijks ontbreekt in de theorieën over de binnenkant van neutronensterren. De superflits heeft hiervoor een belangrijke hint gegeven. De waarneming van de superflits laat zien dat de temperatuur hoger was dan wat de modellen voorspellen. Dit kan erop duiden dat een proces plaatsvindt dat de neutronenster extra verwarmt. Op dit moment wordt uitgezocht wat dit proces is.

6.7 EXPLOSIEF OF STABIEL?

Een röntgenflits is het resultaat van de explosieve verbranding (fusie) van waterstof en helium. De verbranding kan echter ook stabiel verlopen. Dit gebeurt wanneer de snelheid waarmee waterstof en helium worden aangevoerd op de neutronenster, de zogenaamde accretiesnelheid, hoog genoeg is om steeds evenveel brandstof aan te voeren als er verbrand wordt; ligt de accretiesnelheid onder dit niveau, dan vinden er röntgenflitsen plaats. Ligt de snelheid hierboven, dan zijn ze afwezig. Dit gedrag wordt bij sommige neutronensterren daadwerkelijk waargenomen, maar de accretiesnelheid die hierbij wordt waargenomen ligt minstens vier keer lager dan de theorie voorspelt. Er ontbreekt dus nog iets aan ons begrip van dit proces. Recente studies laten zien dat de rotatie van de ster een belangrijke rol speelt bij de stabiele verbranding. Wanneer de ster draait, treedt er turbulentie op die de verschillende lagen van de ster door elkaar mengt. Hierdoor kan waterstof en helium in een diepere laag terecht komen. Daar is de temperatuur hoger, waardoor de verbranding stabiel verloopt.

Wij hebben uitgebreide computermodellen gemaakt van de buitenste laag van een neutronenster. Voor het eerst simuleren we in een dergelijk model zowel de verbranding van helium als de vermenging ten gevolge van rotatie. Het model toont aan dat vermenging er inderdaad voor zorgt dat het verbrandingsproces stabiel verloopt.

6.8 CONCLUSIE

Sinds de ontdekking in de jaren zeventig zijn we veel te weten gekomen over röntgenflitsen en daardoor over neutronensterren. Er zijn echter nog steeds belangrijke aspecten die we niet goed begrijpen. Onze waarneming van twee of drie flitsen binnen twintig minuten is hier een voorbeeld van. Een probleem waarvoor we een mogelijke oplossing hebben gevonden is de waargenomen accretiesnelheid waarbij wel of niet flitsen optreden. Onze modellen tonen aan dat vermenging door de rotatie van de neutronenster zorgt voor een betere overeenstemming met de waarnemingen.

De zeldzame superflitsen, die sinds enkele jaren worden waargenomen, geven informatie over een diepere laag van de neutronenster. We hebben geen nieuwe superflitsen gevonden, maar wel informatie over de minimale dikte van de koolstof-rijke laag die verbrandt tijdens een superflits. Ook analyseerden wij een superflits van een neutronenster die slechts korte tijd materie ontving. Volgens de huidige modellen is dit te kort om de neutronenster voldoende te verhitten voor de ontbranding van koolstof.

Deze resultaten laten zien dat röntgenflitsen ons inderdaad veel informatie geven over het binnenste van neutronensterren: de waarneming van één zeldzame superflits geeft al belangrijke aanwijzingen over op welke punten de huidige modellen verbeterd moeten worden. Wanneer in de toekomst meer (super)flitsen worden waargenomen, dan geeft ons dat de mogelijkheid om onze kennis van deze bijzondere sterren verder te vergroten.

CURRICULUM VITAE

I was born on April 11 1980 in Winterswijk, The Netherlands. Starting in 1992, I attended the secondary school GSG Lingecollege in Tiel. On June 17 1998 I received my *gymnasium* diploma.

At Utrecht University I studied physics and astronomy. During the final year of my undergraduate studies, I worked on the master thesis project *Sterile Neutrinos as Dark Matter*, supervised by prof. dr. J. Smit at the Institute for Theoretical Physics in Utrecht. I received the degree *Master of Science in Physics and Astronomy* on June 28 2004.

In November 2004 I joined the High Energy Astrophysics division at SRON Netherlands Institute for Space Research and the Stellar Evolution and Hydrodynamics group at the Astronomical Institute of Utrecht University. Here I worked with prof. dr. Norbert Langer, dr. Jean in 't Zand and prof. dr. Mariano Méndez to study thermonuclear burning on accreting neutron stars. I analyzed X-ray observations of explosive burning (type I X-ray bursts) and I created sophisticated numerical models of steady-state burning. This work, which you can find in this thesis, resulted in several publications and was presented by me at international conferences and workshops. I will defend my PhD thesis on December 1 2008.

PUBLICATIONS

REFEREED

- ★ L. Keek, J.J.M. in 't Zand, A. Cumming 2006, *The superburst recurrence time in luminous persistent LMXBs*, A&A 455, 1031
- ★ L. Boirin, L. Keek, M. Méndez, A. Cumming, J.J.M. in 't Zand, J. Cottam, F. Paerels, W.H.G. Lewin 2007, *Discovery of X-ray burst triplets in EXO 0748-676*, A&A 465, 559
- ★ L. Keek, J.J.M. in 't Zand, E. Kuulkers, A. Cumming, E.F. Brown, M. Suzuki 2008, *First superburst from a classical low-mass X-ray binary transient*, A&A 479, 177
- ★ J.J.M. in 't Zand, C.G. Bassa, P.G. Jonker, L. Keek, F. Verbunt, M. Méndez, C.B. Markwardt 2008, *An X-ray and optical study of the ultracompact X-ray binary A 1246-58*, A&A 485, 183

OTHER

- ★ P.G. Jonker, L. Keek 2008, *AX J1754.2-2754: back in outburst*, The Astronomer's Telegram, 1643

OBSERVING PROPOSALS

Accepted proposals of which I am the Principle Investigator.

- ★ L. Keek, J.J.M. in 't Zand, P.G. Jonker and M. Méndez 2007, *Taking the temperature of the superburster 4U 1608-522 after an outburst*, XMM-Newton
- ★ L. Keek, P.G. Jonker 2008, *The cold neutron star in the long-duration transient AX J1754.2-2754*, Chandra
- ★ L. Keek, J.J.M. in 't Zand, P.G. Jonker and M. Méndez 2008, *Taking the temperature of the superburster 4U 1608-522 after an outburst*, Chandra

ACKNOWLEDGMENTS

After finishing a master thesis in theoretical physics I decided to do something more directly in touch with the real world. Studying far away stars seemed like an interesting possibility and meant that I could put to use everything I learned during the many astronomy courses I took as an undergraduate student. I consider it a luxury that I was provided with a choice of different research projects. One of these projects was a joint project between SRON and the SIU with both an observational and a theoretical part. Although I was more theoretically oriented, I found it to be a unique opportunity from which I could learn many things. Now, after four years, I can say that it has been a great learning experience indeed, both on a scientific and a personal level. Therefore, I would like to express my gratitude to the people and organizations who have made this possible.

First of all, I would like to thank my (co-)promotors Norbert Langer, Jean in 't Zand and Mariano Méndez for giving me the opportunity to work on a PhD in this fascinating field of research. You provided me with all the knowledge and tools I used in my research, from X-ray observations to stellar evolution models. Your insistence on thoroughness has contributed greatly to the quality of the work presented in this thesis. I am especially thankful for the day-to-day supervision by Jean.

Thank you Norbert for involving me in your work as editor for *Astronomy & Astrophysics*, which has given me an interesting insight into the important process of publishing scientific results.

I would like to thank the co-authors with whom I have collaborated, whose names you can find at the start of the respective chapters in this thesis. In particular I thank Andrew Cumming, who contributed to the discussion of three chapters and who kindly received me as a guest during the summer of 2006. On a similar note, I would like to thank Nobuyuki Kawai, Motoko Suzuki and Makoto Arimoto for my stay at the Tokyo Institute of Technology. Although the work we started is not part of this thesis, I look forward to completing it.

I thank all my HEA colleagues at SRON and SIU colleagues at Utrecht University for their help and interesting discussions as well as the pleasant atmosphere during many meetings, coffee-breaks and lunches. I would like to thank in particular all the people with whom I shared an office: Mariano, Nanda, Jean, Rob and Tayeb. Furthermore,

I thank the non-scientific staff at SRON and Utrecht University who have helped me during the passed few years.

It is a pleasure to thank the members of the thesis committee for carefully studying this thesis and for helpful comments: Alexander Heger, John Heise, Peter Jonker, Michiel van der Klis and Frank Verbunt.

Financial support is acknowledged from the Netherlands Organization for Scientific Research (NWO), the Netherlands Research School for Astronomy (NOVA) and the Leids Kerkhoven-Bosscha Fonds.

Finally, I thank my parents and my brother for their support. In the coming years we will be much farther apart than we have ever been, but I hope that modern technology will keep us close. I would also like to thank my 'Benchmark' friends. While our lives continue to diverge, we still keep many things in common. In particular, I thank Eelke Warrink for his comments on the Dutch summary (Chapter 6).

Laurens Keek
Utrecht, October 2 2008

BIBLIOGRAPHY

- Altamirano, D., van der Klis, M., Wijnands, R., & Cumming, A. 2008, *ApJ*, 673, L35
- Aoki, T., Dotani, T., Ebisawa, K., et al. 1992, *PASJ*, 44, 641
- Arnaud, K. A. 1996, in *ASP Conf. Ser. 101: Astronomical Data Analysis Software and Systems V*, ed. G. H. Jacoby & J. Barnes, 17
- Asai, K. & Dotani, T. 2006, *PASJ*, 58, 587
- Atteia, J.-L., Boer, M., Cotin, F., et al. 2003, in *American Institute of Physics Conference Series*, Vol. 662, *Gamma-Ray Burst and Afterglow Astronomy 2001: A Workshop Celebrating the First Year of the HETE Mission*, ed. G. R. Ricker & R. K. Vanderspek, 17–24
- Ayasli, S. & Joss, P. C. 1982, *ApJ*, 256, 637
- Baade, W. & Zwicky, F. 1934, *Proceedings of the National Academy of Science*, 20, 259
- Balucinska-Church, M. & McCammon, D. 1992, *ApJ*, 400, 699
- Belian, R. D., Conner, J. P., & Evans, W. D. 1976, *ApJ*, 206, L135
- Bell, S. J. & Hewish, A. 1967, *Nature*, 213, 1214
- Bildsten, L. 1995, *ApJ*, 438, 852
- Bildsten, L. 1998, in *NATO ASIC Proc. 515: The Many Faces of Neutron Stars.*, ed. R. Buccheri, J. van Paradijs, & A. Alpar, 419
- Bildsten, L. & Hall, D. M. 2001, *ApJ*, 549, L219
- Boella, G., Butler, R. C., Perola, G. C., et al. 1997a, *A&AS*, 122, 299
- Boella, G., Chiappetti, L., Conti, G., et al. 1997b, *A&AS*, 122, 327
- Bradshaw, C. F., Fomalont, E. B., & Geldzahler, B. J. 1999, *ApJ*, 512, L121
- Bradshaw, C. F., Geldzahler, B. J., & Fomalont, E. B. 2003, *ApJ*, 592, 486
- Braga, J., Rothschild, R., Heise, J., et al. 2004, *Advances in Space Research*, 34, 2657
- Brown, E. F. 2000, *ApJ*, 531, 988
- Brown, E. F. 2004, *ApJ*, 614, L57
- Brown, E. F., Bildsten, L., & Chang, P. 2002, *ApJ*, 574, 920
- Chaboyer, B. & Zahn, J.-P. 1992, *A&A*, 253, 173
- Chelovekov, I. V., Grebenev, S. A., & Sunyaev, R. A. 2007, *ArXiv e-prints*, 709
- Chou, Y. & Grindlay, J. E. 2001, *ApJ*, 563, 934
- Christian, D. J. & Swank, J. H. 1997, *ApJS*, 109, 177
- Cooper, R. L., Mukhopadhyay, B., Steeghs, D., & Narayan, R. 2006, *ApJ*, 642, 443
- Cooper, R. L. & Narayan, R. 2005, *ApJ*, 629, 422
- Cooper, R. L. & Narayan, R. 2007, *ApJ*, 657, L29

- Corbet, R. H. D. 2003, *ApJ*, 595, 1086
- Cornelisse, R., Heise, J., Kuulkers, E., Verbunt, F., & in 't Zand, J. J. M. 2000, *A&A*, 357, L21
- Cornelisse, R., in 't Zand, J. J. M., Verbunt, F., et al. 2003, *A&A*, 405, 1033
- Cottam, J., Paerels, F., & Méndez, M. 2002, *Nature*, 420, 51
- Cumming, A. 2003, *ApJ*, 595, 1077
- Cumming, A. 2004, *Nuclear Physics B Proceedings Supplements*, 132, 435
- Cumming, A. & Bildsten, L. 2000, *ApJ*, 544, 453
- Cumming, A. & Bildsten, L. 2001, *ApJ*, 559, L127
- Cumming, A. & Macbeth, J. 2004, *ApJ*, 603, L37
- Cumming, A., Macbeth, J., in 't Zand, J. J. M., & Page, D. 2006, *ApJ*, 646, 429
- Cumming, A., Zwebel, E., & Bildsten, L. 2001, *ApJ*, 557, 958
- den Hartog, P. R., in 't Zand, J. J. M., Kuulkers, E., et al. 2003, *A&A*, 400, 633
- den Herder, J. W., Brinkman, A. C., Kahn, S. M., et al. 2001, *A&A*, 365, L7
- Di Salvo, T., Farinelli, R., Burderi, L., et al. 2002, *A&A*, 386, 535
- Díaz Trigo, M., Parmar, A. N., Boirin, L., Méndez, M., & Kaastra, J. S. 2006, *A&A*, 445, 179
- Fabian, A. C., Rees, M. J., Stella, L., & White, N. E. 1989, *MNRAS*, 238, 729
- Faucher-Giguère, C.-A. & Kaspi, V. M. 2006, *ApJ*, 643, 332
- Fender, R. 2002, *LNP Vol. 589: Relativistic Flows in Astrophysics*, 589, 101
- Fender, R., Belloni, T., & Gallo, E. 2005, *Ap&SS*, 300, 1
- Fiore, F., Guainazzi, M., & Grandi, P. 1999, *Cookbook for BeppoSAX NFI Spectral Analysis, Version 1.2*.
- Frank, J., King, A. R., & Lasota, J.-P. 1987, *A&A*, 178, 137
- Fraser, G. W. 1989, *X-ray detectors in astronomy* (Cambridge and New York, Cambridge University Press, 1989, 312 p.)
- Frontera, F., Costa, E., dal Fiume, D., et al. 1997, *A&AS*, 122, 357
- Fujimoto, M. Y. 1988, *ApJ*, 324, 995
- Fujimoto, M. Y. 1993, *ApJ*, 419, 768
- Fujimoto, M. Y., Hanawa, T., & Miyaji, S. 1981, *ApJ*, 247, 267
- Fujimoto, M. Y., Sztajno, M., Lewin, W. H. G., & van Paradijs, J. 1987, *ApJ*, 319, 902
- Galloway, D. K., Cumming, A., Kuulkers, E., et al. 2004, *ApJ*, 601, 466
- Galloway, D. K., Munro, M. P., Hartman, J. M., et al. 2006, *ArXiv Astrophysics e-prints*
- Galloway, D. K., Psaltis, D., Chakrabarty, D., & Munro, M. P. 2003, *ApJ*, 590, 999
- Giannone, P. & Weigert, A. 1967, *Zeitschrift fur Astrophysik*, 67, 41
- Gierliński, M. & Done, C. 2002, *MNRAS*, 337, 1373
- Gold, T. 1968, *Nature*, 218, 731
- Gottwald, M., Haberl, F., Parmar, A. N., & White, N. E. 1986, *ApJ*, 308, 213

- Gottwald, M., Haberl, F., Parmar, A. N., & White, N. E. 1987, *ApJ*, 323, 575
- Grindlay, J., Gursky, H., Schnopper, H., et al. 1976, *ApJ*, 205, L127
- Grindlay, J. E. & Liller, W. 1978, *ApJ*, 220, L127
- Gupta, S., Brown, E. F., Schatz, H., Möller, P., & Kratz, K.-L. 2007, *ApJ*, 662, 1188
- Haensel, P. & Zdunik, J. L. 1990, *A&A*, 227, 431
- Haensel, P. & Zdunik, J. L. 2003, *A&A*, 404, L33
- Hansen, J.-P., McDonald, I. R., & Pollock, E. L. 1975, *Phys. Rev. A*, 11, 1025
- Hasinger, G. & van der Klis, M. 1989, *A&A*, 225, 79
- Heger, A., Cumming, A., & Woosley, S. E. 2007, *ApJ*, 665, 1311
- Heger, A., Fryer, C. L., Woosley, S. E., Langer, N., & Hartmann, D. H. 2003, *ApJ*, 591, 288
- Heger, A., Langer, N., & Woosley, S. E. 2000, *ApJ*, 528, 368
- Heger, A., Woosley, S. E., & Spruit, H. C. 2005, *ApJ*, 626, 350
- Hessels, J. W. T., Ransom, S. M., Stairs, I. H., et al. 2006, *Science*, 311, 1901
- Hewish, A., Bell, S. J., Pilkington, J. D., Scott, P. F., & Collins, R. A. 1968, *Nature*, 217, 709
- Hoyle, F. & Fowler, W. A. 1965, in *Quasi-Stellar Sources and Gravitational Collapse*, ed. I. Robinson, A. Schild, & E. L. Schucking, 17
- Hua, X.-M. & Titarchuk, L. 1995, *ApJ*, 449, 188
- Iaria, R., di Salvo, T., Robba, N. R., et al. 2004, *Nuclear Physics B Proceedings Supplements*, 132, 608
- Iaria, R., di Salvo, T., Robba, N. R., et al. 2005, *A&A*, 439, 575
- in 't Zand, J. J. M., Cornelisse, R., & Cumming, A. 2004a, *A&A*, 426, 257
- in 't Zand, J. J. M., Cumming, A., van der Sluys, M. V., Verbunt, F., & Pols, O. R. 2005, *A&A*, 441, 675
- in 't Zand, J. J. M., Jonker, P. G., & Markwardt, C. B. 2007, *A&A*, 465, 953
- in 't Zand, J. J. M., Kuulkers, E., Verbunt, F., Heise, J., & Cornelisse, R. 2003, *A&A*, 411, L487
- in 't Zand, J. J. M., Verbunt, F., Heise, J., et al. 2004b, *Nucl. Phys. Proc. Suppl.*, 132, 486
- Inoue, H., Koyama, K., Makino, F., et al. 1984, *PASJ*, 36, 855
- Jager, R., Mels, W. A., Brinkman, A. C., et al. 1997, *A&AS*, 125, 557
- Jahoda, K., Markwardt, C. B., Radeva, Y., et al. 2006, *ApJS*, 163, 401
- Jansen, F., Lumb, D., Altieri, B., et al. 2001, *A&A*, 365, L1
- Jonker, P. G. & Nelemans, G. 2004, *MNRAS*, 354, 355
- Kaaret, P., Prieskorn, Z., in 't Zand, J. J. M., et al. 2007, *ApJ*, 657, L97
- Keek, L., in 't Zand, J. J. M., & Cumming, A. 2006, *A&A*, 455, 1031
- Keek, L., in 't Zand, J. J. M., Kuulkers, E., et al. 2008, *A&A*, 479, 177
- Kippenhahn, R. 1974, in *IAU Symposium, Vol. 66, Late Stages of Stellar Evolution*, ed. R. J. Tayler & J. E. Hesser, 20
- Kirsch, M. G., Briel, U. G., Burrows, D., et al. 2005, in *UV, X-Ray, and Gamma-*

- Ray Space Instrumentation for Astronomy XIV. Edited by Siegmund, Oswald H. W. Proceedings of the SPIE, Volume 5898, pp. 22-33 (2005)., ed. O. H. W. Siegmund, 22-33
- Kouveliotou, C., Dieters, S., Strohmayer, T., et al. 1998, *Nature*, 393, 235
- Kuulkers, E. 2002, *A&A*, 383, L5
- Kuulkers, E. 2004, *Nucl. Phys. Proc. Suppl.*, 132, 466
- Kuulkers, E. 2005, *The Astronomer's Telegram*, 483, 1
- Kuulkers, E., den Hartog, P. R., in 't Zand, J. J. M., et al. 2003, *A&A*, 399, 663
- Kuulkers, E., Homan, J., van der Klis, M., Lewin, W. H. G., & Méndez, M. 2002a, *A&A*, 382, 947
- Kuulkers, E., in 't Zand, J., Homan, J., et al. 2004, in *AIP Conf. Proc.* 714: X-ray Timing 2003: Rossi and Beyond, 257-260
- Kuulkers, E., in 't Zand, J. J. M., van Kerkwijk, M. H., et al. 2002b, *A&A*, 382, 503
- Lamb, D. Q. & Lamb, F. K. 1978, *ApJ*, 220, 291
- Langmeier, A., Sztajno, M., Hasinger, G., Truemper, J., & Gottwald, M. 1987, *ApJ*, 323, 288
- Lapidus, I. I. & Sunyaev, R. A. 1985, *MNRAS*, 217, 291
- Lattimer, J. M. & Prakash, M. 2007, *Phys. Rep.*, 442, 109
- Lavagetto, G., Iaria, R., di Salvo, T., et al. 2004, *Nuclear Physics B Proceedings Supplements*, 132, 616
- Lebrun, F., Leray, J. P., Lavocat, P., et al. 2003, *A&A*, 411, L141
- Leinson, L. B. & Pérez, A. 2006, *Physics Letters B*, 638, 114
- Levine, A. M., Bradt, H., Cui, W., et al. 1996, *ApJ*, 469, L33+
- Lewin, W. H. G., Hoffman, J. A., Doty, J., et al. 1976, *MNRAS*, 177, 83P
- Lewin, W. H. G., van Paradijs, J., & Taam, R. E. 1993, *Space Science Reviews*, 62, 223
- Liu, Q. Z., van Paradijs, J., & van den Heuvel, E. P. J. 2007, *A&A*, 469, 807
- Lochner, J. C. & Roussel-Dupre, D. 1994, *ApJ*, 435, 840
- London, R. A., Howard, W. M., & Taam, R. E. 1984, *ApJ*, 287, L27
- Makishima, K., Maejima, Y., Mitsuda, K., et al. 1986, *ApJ*, 308, 635
- Maraschi, L. & Cavaliere, A. 1977, in *Highlights in Astronomy*, ed. E. A. Müller, Vol. 4 (Reidel, Dordrecht), 127
- Méndez, M. & Belloni, T. 2007, *MNRAS*, 381, 790
- Miller, J. M. 2007, *ARA&A*, 45, 441
- Mitsuda, K., Inoue, H., Koyama, K., et al. 1984, *PASJ*, 36, 741
- Molkov, S., Revnivtsev, M., Lutovinov, A., & Sunyaev, R. 2005, *A&A*, 434, 1069
- Morrison, R. & McCammon, D. 1983, *ApJ*, 270, 119
- Murakami, T., Inoue, H., Koyama, K., et al. 1980a, *PASJ*, 32, 543
- Murakami, T., Inoue, H., Koyama, K., et al. 1980b, *ApJ*, 240, L143
- Nelemans, G., Jonker, P. G., Marsh, T. R., & van der Klis, M. 2004, *MNRAS*, 348, L7

- Nomoto, K. & Kondo, Y. 1991, *ApJ*, 367, L19
- Ohashi, T., Inoue, H., Koyama, K., et al. 1982, *ApJ*, 258, 254
- Özel, F. 2006, *Nature*, 441, 1115
- Pacini, F. 1967, *Nature*, 216, 567
- Paczynski, B. 1983, *ApJ*, 264, 282
- Page, D. & Reddy, S. 2006, *Annual Review of Nuclear and Particle Science*, 56, 327
- Paizis, A., Beckmann, V., Courvoisier, T. J.-L., et al. 2003, *A&A*, 411, L363
- Parmar, A. N., Martin, D. D. E., Bavdaz, M., et al. 1997, *A&AS*, 122, 309
- Parmar, A. N., White, N. E., Giommi, P., & Gottwald, M. 1986, *ApJ*, 308, 199
- Pedersen, H., Motch, C., van Paradijs, J., et al. 1982, *ApJ*, 263, 340
- Peng, F., Brown, E. F., & Truran, J. W. 2007, *ApJ*, 654, 1022
- Piro, A. L. & Bildsten, L. 2007, *ApJ*, 663, 1252
- Remillard, R., Morgan, E., & The ASM Team at MIT, N. 2005, *The Astronomer's Telegram*, 482, 1
- Revnivtsev, M., Churazov, E., Gilfanov, M., & Sunyaev, R. 2001, *A&A*, 372, 138
- Revnivtsev, M. et al. 2004, *Astron. Lett.*, 30, 382
- Ricker, G. R., Atteia, J.-L., Crew, G. B., et al. 2003, in *American Institute of Physics Conference Series*, Vol. 662, *Gamma-Ray Burst and Afterglow Astronomy 2001: A Workshop Celebrating the First Year of the HETE Mission*, ed. G. R. Ricker & R. K. Vanderspek, 3–16
- Rosenfeld, L. 1974, in *Proc. 16 Solvay Conf. on Phys (Univ. de Bruxells)*, 174
- Rutledge, R. E., Bildsten, L., Brown, E. F., Pavlov, G. G., & Zavlin, V. E. 1999, *ApJ*, 514, 945
- Rutledge, R. E., Bildsten, L., Brown, E. F., Pavlov, G. G., & Zavlin, V. E. 2000, *ApJ*, 529, 985
- Sato, K. 1979, *Progress of Theoretical Physics*, 62, 957
- Schatz, H., Aprahamian, A., Barnard, V., et al. 2001, *Physical Review Letters*, 86, 3471
- Schatz, H., Bildsten, L., Cumming, A., & Ouellette, M. 2003, *Nuclear Physics A*, 718, 247
- Schatz, H., Bildsten, L., Cumming, A., & Wiescher, M. 1999, *ApJ*, 524, 1014
- Shirasaki, Y., Kawai, N., Yoshida, A., et al. 2003, *PASJ*, 55, 1033
- Sidoli, L., Parmar, A. N., & Oosterbroek, T. 2005, *A&A*, 429, 291
- Sidoli, L., Parmar, A. N., Oosterbroek, T., et al. 2001, *A&A*, 368, 451
- Spitkovsky, A., Levin, Y., & Ushomirsky, G. 2002, *ApJ*, 566, 1018
- Spruit, H. C. 2002, *A&A*, 381, 923
- Stella, L., Friedhorsky, W., & White, N. E. 1987, *ApJ*, 312, L17
- Strüder, L., Briel, U., Dennerl, K., et al. 2001, *A&A*, 365, L18
- Strohmayer, T. & Bildsten, L. 2006, *New views of thermonuclear bursts (Compact stellar X-ray sources)*, 113–156

- Strohmayer, T. E. & Brown, E. F. 2002, *ApJ*, 566, 1045
- Strohmayer, T. E. & Markwardt, C. B. 2002, *ApJ*, 577, 337
- Suijs, M. P. L., Langer, N., Poelarends, A.-J., et al. 2008, *A&A*, 481, L87
- Swank, J. H., Becker, R. H., Boldt, E. A., et al. 1977, *ApJ*, 212, L73
- Talon, S. 2004, in *IAU Symposium*, Vol. 215, *Stellar Rotation*, ed. A. Maeder & P. Eenens, 336
- Tananbaum, H., Chaisson, L. J., Forman, W., Jones, C., & Matilsky, T. A. 1976, *ApJ*, 209, L125
- Thompson, C. & Duncan, R. C. 1995, *MNRAS*, 275, 255
- Thompson, C. & Duncan, R. C. 1996, *ApJ*, 473, 322
- Titarchuk, L. 1994, *ApJ*, 434, 570
- Titarchuk, L. & Lyubarskij, Y. 1995, *ApJ*, 450, 876
- Treves, A., Turolla, R., Zane, S., & Colpi, M. 2000, *PASP*, 112, 297
- Turner, M. J. L., Abbey, A., Arnaud, M., et al. 2001, *A&A*, 365, L27
- Ubertini, P., Lebrun, F., Di Cocco, G., et al. 2003, *A&A*, 411, L131
- van der Klis, M. 2006, *Rapid X-ray Variability (Compact stellar X-ray sources)*, 39–112
- van Paradijs, J., Penninx, W., & Lewin, W. H. G. 1988, *MNRAS*, 233, 437
- van Straaten, S., van der Klis, M., & Méndez, M. 2003, *ApJ*, 596, 1155
- Verner, D. A., Ferland, G. J., Korista, K. T., & Yakovlev, D. G. 1996, *ApJ*, 465, 487
- Wachter, S., Hoard, D. W., Bailyn, C. D., Corbel, S., & Kaaret, P. 2002, *ApJ*, 568, 901
- Wallace, R. K. & Woosley, S. E. 1984, in *American Institute of Physics Conference Series*, Vol. 115, *American Institute of Physics Conference Series*, ed. S. E. Woosley, 319
- Weinberg, N. N., Bildsten, L., & Schatz, H. 2006, *ApJ*, 639, 1018
- Wijnands, R., Muno, M. P., Miller, J. M., et al. 2002, *ApJ*, 566, 1060
- Wijnands, R. & van der Klis, M. 1998, *Nature*, 394, 344
- Wilms, J., Allen, A., & McCray, R. 2000, *ApJ*, 542, 914
- Winkler, C., Courvoisier, T. J.-L., Di Cocco, G., et al. 2003, *A&A*, 411, L1
- Wolff, M. T., Becker, P. A., Ray, P. S., & Wood, K. S. 2005, *ArXiv Astrophysics e-prints*, accepted for publication in *APJ*, astro-ph/0506515
- Wolff, M. T., Hertz, P., Wood, K. S., Ray, P. S., & Bandyopadhyay, R. M. 2002, *ApJ*, 575, 384
- Woosley, S. E., Heger, A., Cumming, A., et al. 2004, *ApJS*, 151, 75
- Woosley, S. E. & Taam, R. E. 1976, *Nature*, 263, 101
- Yakovlev, D. G., Kaminker, A. D., & Levenfish, K. P. 1999, *A&A*, 343, 650
- Yoon, S.-C., Langer, N., & Scheithauer, S. 2004a, *A&A*, 425, 217
- Yoon, S.-C., Langer, N., & van der Sluys, M. 2004b, *A&A*, 425, 207
- Zahn, J.-P., Brun, A. S., & Mathis, S. 2007, *A&A*, 474, 145